

SIMULATION-BASED COMPARISON OF  
SOME GMTI TECHNIQUES

A THESIS SUBMITTED TO  
THE GRADUATE SCHOOL OF NATURAL AND APPLIED SCIENCES  
OF  
MIDDLE EAST TECHNICAL UNIVERSITY

BY

CAN BAKTIR

IN PARTIAL FULFILLMENT OF THE REQUIREMENTS  
FOR  
THE DEGREE OF MASTER OF SCIENCE  
IN  
ELECTRICAL & ELECTRONICS ENGINEERING

MARCH 2009

**Approval of the thesis:**

**SIMULATION-BASED COMPARISON OF CONVENTIONAL and DEVELOPING  
GMTI TECHNIQUES**

submitted by **CAN BAKTIR** in partial fulfillment of the requirements for the degree  
of **Master of Science in Electrical & Electronics Engineering Department,**  
**Middle East Technical University** by,

Prof. Dr. Canan Özgen  
Dean, Graduate School of **Natural and Applied  
Sciences**

\_\_\_\_\_

Prof. Dr. İsmet Erkmén  
Head of Department, **Electrical & Electronics  
Engineering**

\_\_\_\_\_

Assoc. Prof. Dr. Seyit Sencer Koç  
Supervisor, **Electrical & Electronics Engineering,**  
**METU**

\_\_\_\_\_

**Examining Committee Members**

Prof. Dr. Yalçın Tanık  
Electrical & Electronics Engineering, METU

\_\_\_\_\_

Assoc. Prof. Dr. Seyit Sencer Koç  
Electrical & Electronics Engineering, METU

\_\_\_\_\_

Prof. Dr. Mete Severcan  
Electrical & Electronics Engineering, METU

\_\_\_\_\_

Assist. Prof. Dr. Ali Özgür Yılmaz  
Electrical & Electronics Engineering, METU

\_\_\_\_\_

Dr. Ülkü Çilek Doyuran  
Design Leader, ASELSAN

\_\_\_\_\_

Date:

25 March 2009

**I hereby declare that all information in this document has been obtained and presented in accordance with academic rules and ethical conduct. I also declare that, as required by these rules and conduct, I have fully cited and referenced all material and results that are not original to this work.**

Name, Last Name : CAN BAKTIR

Signature :

## **ABSTRACT**

### SIMULATION-BASED COMPARISON OF SOME GMTI TECHNIQUES

Baktır, Can

M.S., Department of Electrical & Electronics Engineering

Supervisor : Assoc. Prof. Dr. Seyit Sencer Koç

March 2009, 105 pages

With the developing radar technology, radars have been started to be used in the airborne platforms due to the need of fast, accurate and reliable information about the enemies. The most important and tactically needed information is the movements in an observation area. The detection of a ground moving target buried in a dense clutter environment from a moving air platform is a very challenging problem even today. The geometry of the operation, the course of the flight and structure of the clutter are the most effective parameters of this problem.

There are some "*Ground Moving Target Indication*" (GMTI) techniques that have been studied for the last twenty years to overcome this problem. In this thesis, the simulation of some of these techniques in a realistic environment and the comparison of their performances are discussed.

In this work, a GMTI simulator is developed to generate the environment containing the clutter and the noise signals, to locate and simulate the targets in this environment and to apply the GMTI techniques on the raw data generated by the simulator. The generation of the clutter signals including the *internal clutter motion* (ICM) for different types of clutter distributions is one of the most important parts of this thesis.

The GMTI techniques being investigated throughout this thesis are "*Displaced Phase Center Antenna*" (DPCA), "*Along-Track Interferometry*" (ATI), "*Adaptive DPCA*", "*Pre-Doppler Sigma-Delta STAP*" and "*Post-Doppler Sigma-Delta STAP*" techniques. These techniques are compared according to their clutter suppression and target detection performances under different environmental conditions.

**Key Words:** GMTI, DPCA, Adaptive DPCA, ATI, Sigma-Delta STAP, Internal Clutter Motion (ICM)

# ÖZ

## BAZI GMTI TEKNİKLERİNİN SİMÜLASYON TABANLI KARŞILAŞTIRMASI

Baktır, Can

Y. Lisans, Elektrik & Elektronik Mühendisliği Bölümü

Tez Yöneticisi : Assoc. Prof. Dr. Seyit Sencer Koç

Mart 2009, 105 sayfa

Gelişen radar teknolojisi ile radarlar, düşman hakkında hızlı, doğru ve güvenilir bilgi edinme ihtiyacı nedeniyle hava platformlarında da kullanılmaya başlanmıştır. En önemli ve taktik açıdan en çok ihtiyaç duyulan bilgi gözlem alanı içerisindeki hareketlerin bilgisi olmuştur. Fakat yoğun kargaşa ortamına gömülü olan yeryüzünde hareket eden hedeflerin tespit edilmesi problemi bugün bile çok zor bir çalışmadır. Operasyonun geometrisi, uçuş seyri ve kargaşa yapısı bu problemin en etkili parametrelerini oluşturmaktadır.

Son yirmi yıl içerisinde üzerinde çalışılmakta olan bazı "Yeryüzünde Hareket Eden Hedeflerin Gösterimi" (GMTI) teknikleri bulunmaktadır. Bu tez kapsamında bu tekniklerden bazılarının gerçekçi bir ortam üzerinde gerçekleşmesi ve başarımlarının karşılaştırması yapılmaktadır.

Tez kapsamında, kargaşa ve gürültü sinyallerini içeren bir ortamın üretildiği, bu ortam üzerine hedefleri konumlandırarak benzetimlerinin yapıldığı ve GMTI tekniklerinin üretilen ham veri üzerine uygulandığı bir GMTI simülatörü geliştirilmiştir. Kargaşa içi hareketlerin de (ICM) olduğu kargaşa sinyallerinin farklı kargaşa dağılımları için üretilmesi tezin en önemli kısımlarından biridir.

Bu tez kapsamında incelenen GMTI teknikleri "*Displaced Phase Center Antenna*" (DPCA), "*Along-Track Interferometry*" (ATI), "*Adaptive DPCA*", "*Pre-Doppler Sigma-Delta STAP*" ve "*Post-Doppler Sigma-Delta STAP*" teknikleridir. Bu teknikler, çeşitli çevresel şartlardaki kargaşa bastırma ve hedef tespit etme performanslarına göre karşılaştırılmıştır.

**Anahtar Kelimeler:** GMTI, DPCA, Adaptive DPCA, ATI, Sigma-Delta STAP, ICM

Sevgili Ailem  
ve  
Yasemin'ime...

## **ACKNOWLEDGEMENTS**

This thesis was written with the help and assistance of various people and I would like to take this opportunity to acknowledge the tremendous help they have given me while I was completing my thesis.

Firstly, I would like to thank Assoc. Prof. Dr. Seyit Sencer Koç, for his counselling, technical help and guidance which help me stay always in the right direction.

I would like to thank my lovely parents for their help, support and trust they have given me along my life.

I would like to convey my great thanks to my love Yasemin because she has turned my life to a heaven for last one year.

I would address my finally thanks to ASELSAN A.Ş., who gave me the opportunity to apply my studies to the realistic works.

## TABLE OF CONTENTS

ABSTRACT .....	iv
ÖZ .....	vi
ACKNOWLEDGEMENTS .....	ix
TABLE OF CONTENTS .....	x
LIST OF FIGURES .....	xii
1. INTRODUCTION .....	1
1.1. Motivation.....	1
1.2. Thesis Objective .....	2
1.3. Thesis Organization .....	3
2. BACKGROUND .....	4
2.1. History.....	4
2.1.1. History of GMTI's Operational Usage.....	4
2.1.2. GMTI Literature .....	6
2.2. GMTI Geometry.....	8
2.3. GMTI Performance Factors .....	12
2.3.1. Minimum Detectable/Discernible Velocity (MDV) .....	12
2.3.2. Target Location Accuracy.....	13
2.3.3. Target Range Resolution.....	13
2.3.4. Clutter Attenuation.....	14
2.3.5. Improvement Factor.....	14
2.3.6. Detection Probability .....	15
2.3.7. Stand-off distance.....	15
2.4. Doppler In GMTI .....	15
2.5. Clutter Structure.....	23
3. GMTI TECHNIQUES.....	28
3.1. Displaced Phase Center Antenna (DPCA) .....	28
3.2. Adaptive DPCA .....	31
3.3. Along Track Interferometry (ATI).....	37
3.4. $\Sigma - \Delta$ STAP.....	40

3.5. Detection Algorithm .....	46
4. GMTI SIMULATOR .....	48
4.1. The Purpose of the Simulator .....	48
4.2. Basic Properties of the Simulator.....	48
4.3. Clutter Generation .....	52
4.4. Moving Target Generation .....	60
4.5. Applying GMTI Techniques .....	63
5. SIMULATION RESULTS.....	65
5.1. DPCA.....	65
5.2. Adaptive DPCA .....	78
5.3. ATI.....	83
5.4. $\Sigma - \Delta$ STAP.....	88
5.5. Comparison of GMTI Techniques.....	96
6. CONCLUSIONS .....	100
6.1. Thesis Summary.....	100
6.2. Future Work.....	102
REFERENCES.....	103

## LIST OF FIGURES

Figure - 2.1: GMTI Geometry .....	8
Figure - 2.2: Squint Angle.....	9
Figure - 2.3: Radar Look Angle and Ground Resolution .....	10
Figure - 2.4: Resolution Area .....	11
Figure - 2.5: Target Velocity Component According to the Radar .....	13
Figure - 2.6: Radar Illumination Area and Related Doppler Spreads.....	16
Figure - 2.7: Doppler Sprectrum for an Airborne Radar .....	17
Figure - 2.8: Doppler Spectrum of Exo-Clutter GMTI .....	18
Figure - 2.9: Doppler Spectrum of Endo-Clutter GMTI .....	19
Figure - 2.10: a) Different Positions of Radar in the Flight b) Related Doppler History .....	20
Figure - 2.11: Radar and Target Locations and Velocities .....	21
Figure - 2.12: Doppler History for a Target a) Approaching to the Radar Flight Direction b) Approaching from the Radar Flight Direction .....	22
Figure - 2.13: Doppler History for a Target a) Moving Same Direction with Radar b) Moving Opposite Direction with Radar .....	23
Figure - 2.14: Clutter Patch for a Side Looking Radar .....	24
Figure - 2.15: Point Scatterers in the Clutter Patches .....	25
Figure - 2.16: Complex Clutter Samples in the Range Bins Collecting in each Pulse	26
Figure - 2.17: Autocorrelation Function of a Noise-like Vector $x$ .....	27
Figure - 3.1: DPCA Antenna Alignment Geometry.....	28
Figure - 3.2: DPCA Processing Block Diagram.....	29
Figure - 3.3: DPCA Antenna Misalignment.....	31
Figure - 3.4: Adaptive DPCA Processing Block Diagram .....	33
Figure - 3.5: Power Spectral Density of Noise and Clutter.....	34
Figure - 3.6: Block Diagram of Clutter Covariance Matrix Estimation from Neighbor Range Bins.....	35
Figure - 3.7: ATI Processing Block Diagram.....	37

Figure - 3.8: Distribution of Clutter Samples in Complex Plane After Correlation ....	38
Figure - 3.9: Magnitude vs. Phase Distribution of Clutter at the ATI Processor Output .....	38
Figure - 3.10: Magnitude vs. Phase Distribution of Interference According to CNR.	39
Figure - 3.11: Angle and Doppler Domains of $\Sigma - \Delta$ STAP .....	40
Figure - 3.12: Sum and Different Beams used in $\Sigma - \Delta$ STAP .....	41
Figure - 3.13: Pre-Doppler $\Sigma - \Delta$ STAP Processing Block Diagram .....	43
Figure - 3.14: Post-Doppler $\Sigma - \Delta$ STAP Processing Block Diagram .....	45
Figure - 3.15: Detection Regions for ATI Processor Output.....	47
Figure - 4.1: GMTI Simulator Graphical User Interface.....	49
Figure - 4.2: Radar Parameters Selection Section .....	49
Figure - 4.3: Noise Addition Checkbox .....	50
Figure - 4.4: Antenna Parameters Selection Section .....	50
Figure - 4.5: Same Antenna Paramets Selection Checkbox .....	51
Figure - 4.6: Radar Parameters Loading Button .....	51
Figure - 4.7: Entering FM Bandwidth .....	51
Figure - 4.8: Clutter Generation Type Selection .....	52
Figure - 4.9: Clutter Parameters Selection Section .....	52
Figure - 4.10: Clutter Generation Geometry .....	53
Figure - 4.11: Ground RCS Values According to the Range .....	58
Figure - 4.12: Reflectivity Matrix .....	58
Figure - 4.13: Raw Clutter Data Generation Block Diagram.....	59
Figure - 4.14: Targets Located in Different Range Bins in a Pulse.....	59
Figure - 4.15: Moving Target Parameters Selection Section .....	61
Figure - 4.16: Moving Target Generation Geometry .....	62
Figure - 4.17: Raw GMTI Data Generation Block Diagram.....	64
Figure – 5.1: a) Range-Doppler Output of First Channel b) Range-Doppler DPCA Output for Perfectly Aligned Antenna Case.....	66
Figure – 5.2: a) Range-Doppler Output of First Channel b) Range-Doppler DPCA Output for Perfectly Aligned Antenna Case (target exists) .....	68
Figure – 5.3: Clutter Attenuation vs. Normalized Frequency for DPCA.....	69

Figure – 5.4: Range-Doppler DPCA Output for a) Perfectly Aligned Antenna Case b) Phase Center Misaligned Case (target exist).....	69
Figure – 5.5: Phase Shift in the Received Signal according to the Phase Center Misalignment for a Target Located at the Center of Radar Beam.....	70
Figure – 5.6: Phase Shift in the Received Signal according to the Phase Center Misalignment for a Target Located 1 Degree Squinted from the Center of Radar Beam.....	71
Figure – 5.7: Clutter Attenuation vs. Phase Center Misalignment.....	72
Figure – 5.8: a) Range-Doppler Output of First Channel b) Range-Doppler DPCA Output for Perfectly Aligned Antenna Case (ICM and target exist).....	74
Figure – 5.9: Average Correlation of Clutter Samples according to the Correlation Factor.....	75
Figure – 5.10: Clutter Attenuation vs. Clutter Correlation Factor.....	75
Figure – 5.11: a) Range-Doppler DPCA Output b) CFAR processor output (Rayleigh distribution) .....	77
Figure – 5.12: a) Range-Doppler DPCA Output b) CFAR processor output (K-distribution) .....	77
Figure – 5.13: a) Range-Doppler Output of First Channel b) Range-Doppler Adaptive DPCA Output for Perfectly Aligned Antenna Case (target exists) .....	78
Figure – 5.14: Clutter Attenuation vs. Normalized Frequency for Adaptive DPCA ...	79
Figure – 5.15: Range-Doppler Adaptive DPCA Output for a) Perfectly Aligned Antenna Case b) Phase Center Misaligned Case (target exist).....	79
Figure – 5.16: Clutter Attenuation vs. Phase Center Misalignment.....	80
Figure – 5.17: a) Range-Doppler Output of First Channel b) Range-Doppler Adaptive DPCA Output for Perfectly Aligned Antenna Case (ICM and target exist).....	80
Figure – 5.18: Clutter Attenuation vs. Clutter Correlation Factor.....	81
Figure – 5.19: a) Range-Doppler DPCA Output b) CFAR processor output (Rayleigh distribution) .....	82
Figure – 5.20: a) Range-Doppler DPCA Output b) CFAR processor output (K-distribution) .....	82
Figure – 5.21: a) ATI Output at Complex Plane b) ATI Output at Phase-Magnitude Plane (only highly correlated clutter) .....	84
Figure – 5.22: a) ATI Output at Complex Plane b) ATI Output at Phase-Magnitude Plane (only clutter, correlation factor = 0.9999) .....	84

Figure – 5.23: ATI Output at Phase-Magnitude Plane for Different Correlation Factors .....	85
Figure – 5.24: ATI Output at Phase-Magnitude Plane for Different Phase Center Misalignments .....	85
Figure – 5.25: ATI Output at Phase-Magnitude Plane a) with a Target having 3m/s velocity b) with a Target having 6m/s velocity (correlation factor = 0.9999) .....	86
Figure – 5.26: ATI Output at Phase-Magnitude Plane for the cases a) Noise exist b) No noise .....	87
Figure – 5.27: a) Range-Doppler Output of Sigma Channel, b) Range-Doppler Output of Delta Channel (no ICM) .....	89
Figure – 5.28: a) Taylor Pattern (SSL = -35 dB) b) Bayliss Pattern .....	89
Figure – 5.29: Output of Pre-Doppler $\Sigma - \Delta$ STAP .....	90
Figure – 5.30: a) Range-Doppler Output of Sigma Channel, b) Range-Doppler Output of Delta Channel (no ICM) .....	91
Figure – 5.31: Output of Post-Doppler $\Sigma - \Delta$ STAP .....	92
Figure – 5.32: Output of Post-Doppler $\Sigma - \Delta$ STAP (narrow beam antenna) .....	94
Figure – 5.33: Output of Post-Doppler $\Sigma - \Delta$ STAP (small RCS target) .....	94
Figure – 5.34: Range-Doppler Output of Post-Doppler $\Sigma - \Delta$ STAP a) Correlation Factor = 1, b) Correlation Factor = 0.6 .....	95

# CHAPTER 1

## INTRODUCTION

### 1.1. Motivation

The term RADAR stands for "*RADio Detection And Ranging*" and they are designed to detect, locate and track targets by using the echoes of them.

When radar was first developed in the World War II era, the system basically consisted of a ground-based antenna and was working by transmitting a pulse and listening to its echo. With the developing radar technology, it has been started to be used in many types of platforms. But each platform had its own problems that have to be overcome.

The most important effect to accelerate the development of the radar technology is the need of information of enemies beyond front lines. There was a rapid transition from the ground-to-air surveillance systems to the air-to-ground surveillance systems. Airborne radar concept has seemed to have great tactical advantages compared to the ground-based radar systems. The first air-based radar systems were SLAR (Side Looking Airborne Radar) systems, which give a map like information of the observation area. But, the more important and critical issue was the detection of moving objects located in the observation area.

The problem of detecting a moving target from an air platform is a very challenging subject even today. Determining the target signal buried in a

dense clutter environment is not easy as it is done in the ground-based radar systems. Suppressing the effects of the aircraft motion is the main work that has to be done in air-to-ground surveillance systems.

There are many works that has been done for the last twenty years, which can be classified into the subject of as Ground Moving Target Indication (GMTI). The techniques used to detect targets moving on the ground from an air platform are basically called as GMTI techniques.

The summary of the works that have been done is given in the "GMTI Literature" section (2.1.2) and a comparison of the basic GMTI techniques is discussed in this thesis.

## **1.2. Thesis Objective**

The primary objective of this thesis is to investigate the performances of the basic GMTI techniques under different environments. This goal can be accomplished by constructing a sample-based GMTI simulator that incorporates various system, environment and target parameters to the simulation to see and evaluate the performances of these GMTI techniques. It is imperative to develop a reliable system and environment model. This model must also support an expandable configuration to study different system designs.

In summary, the objectives of this thesis are:

- Define the geometry and the environment of the target detection problem for the ground-looking airborne radar systems
- Investigate the basic GMTI techniques, their advantages and disadvantages
- Construct a sample-based GMTI simulator that incorporates various system, environment and target parameters
- Run the techniques under different operational conditions and compare the results

### **1.3. Thesis Organization**

This chapter gives the motivation and objectives of this thesis. Chapter 2 details the background information needed to understand the air-to-ground surveillance concept. The operational and literature history, the geometry of the GMTI systems, the performance factors, the Doppler and the clutter structures are explained in this chapter. Chapter 3 covers the basic GMTI techniques that are going to be examined in this thesis. Chapter 4 presents the simulator developed through the scope of this thesis. The techniques used to have a realistic model in this simulator are explained in this chapter. Chapter 5 gives the results of the GMTI techniques explained in Chapter 3 and mentions the comparison of these techniques.

## **CHAPTER 2**

### **BACKGROUND**

#### **2.1. History**

##### **2.1.1. History of GMTI's Operational Usage**

The need to GMTI technology was firstly realized after Arab-Israeli War in 1973 due to the need of situation information of enemy beyond the front lines. With U.S. Army's Stand-Off Target Acquisition System (SOTAS) and U.S. Air Force/Defense Advanced Research Projects Agency (DARPA) Assault Breaker/Pave Mover programs, the research on GMTI technology was initiated. However, because of the fund limitations of separate programs, Army and Air Force leaders agreed to join the efforts in a single program, Joint STARS (Surveillance and Target Attack Radar System), that would provide battle management of strike aircraft for the Air Force and wide area surveillance for the Army [7].

The purpose of the system was to detect targets moving slowly on the land and targets moving with high speed towards the radar like guided weapons.

The Desert Storm operation in the Gulf War was the first operation in which two Joint STARS aircrafts were used. During the Battle of Al Khafji, Joint STARS' GMTI information made it possible to locate advancing Iraqi ground

forces that had attacked at night in an effort to avoid detection. The Coalition's Air Forces used GMTI cues to locate, target, and destroy these forces before the majority of them could close with Coalition land forces.

After the war, many U.S. military leaders recognized the importance of the contribution that GMTI and Joint STARS made. It is stated by the commanders that, "Joint STARS was the single most valuable intelligence and targeting system in Desert Storm."

With this accomplishment, GMTI technology was started to be used by the US Air Forces and US NAVY.

Joint STARS' GMTI system was secondly used in Kosovo. But this time, Kosovo's rugged terrain and foliage increased the amount of radar screening, making it more difficult for Joint STARS' GMTI surveillance to detect, locate, and track mobile forces. Moreover, the lack of friendly ground troops to threaten Serb units, even with a high sortie rate, the limited number of aircrafts, the distance they had to fly from their base to their orbit and Serb civilians as "human shields" decreased the performance of Joint STARS. The situation remained stuck because there wasn't any movement of Serb forces until the attack of Kosovo Liberation Army (KLA). When KLA began to attack, it was a dilemma for Serb forces because of Joint STARS' GMTI. If the Serbs had attempted to maneuver, the movement would have made their forces visible to GMTI and thus vulnerable to NATO air attack. If the Serbs had not moved, they would have lost their ability to achieve the force ratios and position needed to defeat the lighter KLA forces.

Joint STARS operations during Operation Enduring Freedom in Afghanistan have many similarities with previous conflicts. As in Kuwait and Kosovo, Joint STARS was not deployed in sufficient number of aircrafts for persistent coverage. Like Kosovo, the presence of civilians required positive target identification by an unmanned aerial vehicle (UAV) or manned aircraft. However, Joint STARS enhanced other surveillance assets by cueing UAVs

with high resolution but restricted field-of-view sensors. Northern Alliance units supported by U.S. Special Operations Forces (SOF) threatened Taliban and al Qaeda forces sufficiently to cause them to move in vehicles, allowing GMTI to detect, locate, and track them.

U.S. and British forces in Operation Iraqi Freedom benefited from the Joint STARS lessons learned from previous conflicts. For the first time, sufficient number of aircrafts were deployed to meet the GMTI requirement for a major portion of the operational area. Because GMTI was capable of detecting vehicular movement, Iraqi commanders and their forces faced the same operational and tactical dilemma the Serbs faced in Kosovo. If they moved, they were seen by GMTI and attacked by air or artillery. If they dispersed and remained camouflaged and dug in, they were either bypassed or defeated in detail by ground forces.

### **2.1.2. GMTI Literature**

GMTI is a concept used in airborne radars and it is under development even today. There are some techniques evaluated and having known performance limitations. But there are also some new techniques which are being investigated and developed.

Basically, GMTI techniques diverge into a few main branches. Some techniques use the advantage of the Doppler domain analysis. These techniques rely on the fact that the echo of a moving target will have a Doppler shift while the echo of unwanted clutter will only contain a small Doppler spread around the radar frequency. Hence a frequency analysis may provide information about the presence of a moving target.

The oldest, simplest and mostly used GMTI technique using the advantage of Doppler domain analysis is the Displaced Phase Center Antenna (DPCA) technique. This technique uses the advantage of the temporal measurement diversity from the same location with two antennas. Its performance limitations are known quite well, because it is the most frequently used

technique in real operations. It is known that the DPCA has some performance limitations in spite of its hardware simplicity. Adaptive DPCA is a technique similar to the DPCA, which uses the advantage of sub-Doppler band clutter cancellation weights optimization. This is a more complex technique as compared to the DPCA, but it has the advantage of adaptive signal processing for canceling the clutter.

The cancellation weight optimizations can be improved to the temporal and spatial domains simultaneously. Space-Time Adaptive Processing (STAP) can be seen as the optimum solution used in multi-channel systems for clutter cancellation. It has some different approaches for the processing. Mostly used ones are the pre-Doppler (sub-CPI), post-Doppler (long-CPI) and Knowledge-Aided STAP [9], [10]. In these techniques, the advantage of having multi-channels is used. But there is another version optimized for two antennas having different antenna beams.  $\Sigma - \Delta$  STAP uses the advantage of the antennas having same phase centers but different beam shapes [14].

STAP algorithms are under development and recently they have been implemented in operational systems.

Along-Track Interferometry (ATI) is not a clutter cancellation technique. It uses the advantage of the temporal measurement diversity from the same location with two antennas and the clutter correlation [8]. There are some theoretical and experimental research being done for this.

Other techniques use the image formation algorithms and SAR data to detect the moving targets. They mainly use one or more SAR images to obtain moving targets. Focusing [5] is a technique that uses the changes in the sharpness of the image to detect moving targets. Actually, focusing techniques are not used directly for the moving target detection. They are complementary to Doppler-sensing moving target indicators, which can sense only the radial velocity of rapidly moving targets. There are some other techniques using a model-based approach and one SAR image to detect the moving target. Their purpose is to match the target buried into

the complex SAR image with a target model after a number of matching iterations [16].

Some other techniques use more than one SAR images taken from the same location in different time instants. They try to detect moving targets from the changes between SAR images [4].

The SAR image based GMTI techniques are encountered in literature but no information of their operational usage could be found.

## 2.2. GMTI Geometry

GMTI is a key technology used for the surveillance and reconnaissance of land based moving targets from an air platform. In the air-to-land surveillance, geometry is basically defined with the flight and radar parameters. These parameters are used to clarify the locations of the radar and the observation area.

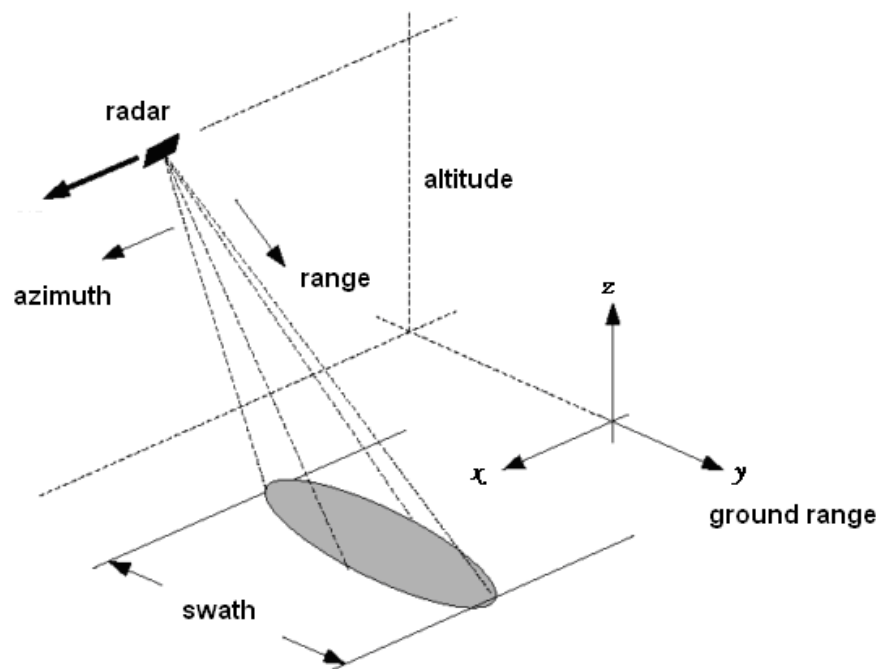


**Figure - 2.1:** GMTI Geometry

Flight parameters define two basic properties of the geometry which are the altitude of the flight and the velocity of the aircraft. The actual properties of the geometry are determined by the radar parameters.

The ground range is the distance between the projection of the radar platform on the ground and the target location and hence does not take altitude into account (Figure - 2.1). The real distance between them is called as the slant range. In airborne radars, the range term is commonly used to mean the slant range.

GMTI Radars usually operate in side-looking configuration. This means that the observation area is usually located at one side of the flight direction and the radar range direction is perpendicular to it. In some cases, range direction may not be perpendicular to the flight direction. The angle between the normal axis of the flight and the range direction is called the squint angle (Figure - 2.2).

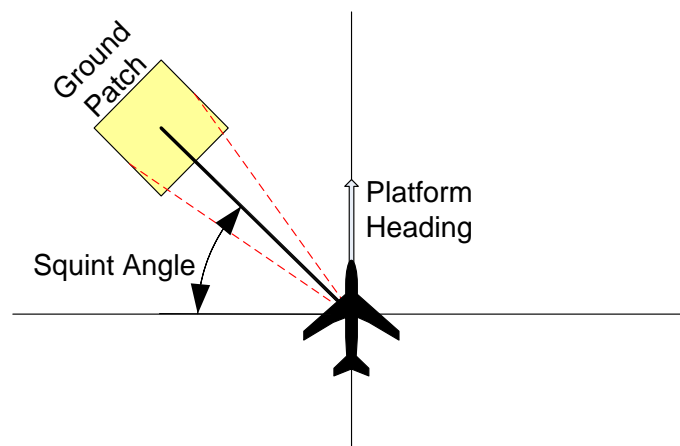


**Figure - 2.2:** Squint Angle

Another important parameter is the look angle ( $\varphi$ ). It is defined as the angle between ground normal axis and the radar beam incidence angle (Figure - 2.3). For a low altitude, far looking radar, look angle will be close to 90 degrees.

In airborne radars, the slant range resolution ( $\Delta R_{slant}$ ) and the ground range resolution ( $\Delta R_{ground}$ ) are different. The slant range resolution is defined as the range resolution on the slant-range direction and is given by

$$\Delta R_{slant} = \frac{c\tau}{2} \quad (2.1)$$

where  $\tau$  is the pulse width of the radar.

The ground range resolution is the projection of the slant range resolution on the ground. The formula

$$\Delta R_{ground} = \Delta R_{slant} / \sin(\varphi) \quad (2.2)$$

shows the relationship between them.

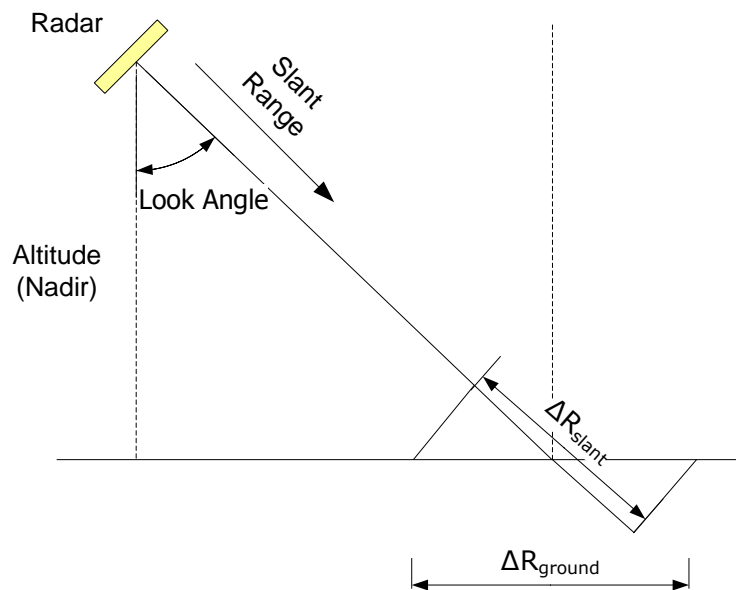


**Figure - 2.3:** Radar Look Angle and Ground Resolution

The look angle, the azimuth beamwidth ( $\theta_{az}$ ) and the ground range resolution of the radar defines the resolution cell ( $\Delta A_c$ ) on the ground (Figure - 2.4).

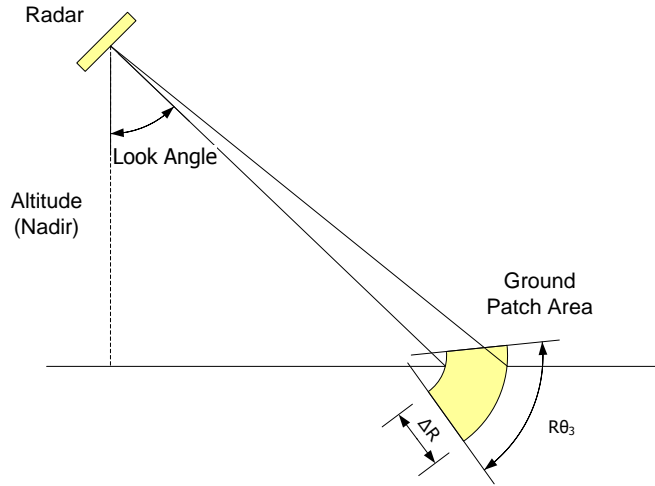


**Figure - 2.4:** Resolution Area

The distance between two points at a range  $R$  for an azimuth beamwidth  $\phi_{az}$  is called as the cross-range resolution.

$$\Delta R_{cross} = R\phi_{az} \quad \text{where } \phi_{az} \text{ is in radians} \quad (2.3)$$

So, the resolution cell area can be found with the equation given below:

$$\Delta A_c = \Delta R_{slant} R\phi_{az} / \cos(\varphi) \quad (2.4)$$

$$\Delta A_c = \frac{c\tau R\phi_{az}}{2\cos(\varphi)} \quad (2.5)$$

The purpose of the GMTI techniques is to detect the targets moving in a dense clutter area. The bigger is the clutter area; the bigger is the reflected clutter power to the radar. So, the main purpose of GMTI radars is to minimize the resolution cell area and maximize the Signal-to-Clutter Ratio (SCR) to be able to detect the targets.

There is one more parameter of the radar to be set for the air-to-ground surveillance radars which is the Pulse Repetition Frequency (PRF) of the radar. If the radar operates in unambiguous mode, that is there is no ambiguity in range or Doppler, PRF must be selected according to the maximum unambiguous range whose relationship with PRF is given below:

$$R_{unam} = \frac{cPRI}{2} = \frac{c}{2PRF} \quad (2.6)$$

$$PRF = \frac{c}{2R_{unam}} \quad (2.7)$$

PRF and the velocity of the flight determine the distance between the two consecutive pulses in the flight direction.

$$\Delta R_{pulses} = \frac{V_{flight}}{PRF} \quad (2.8)$$

This distance determines the correlation of the clutter between two consecutive pulses. In section 2.5, this is going to be explained in detail.

### **2.3. GMTI Performance Factors**

The following factors determine the performance levels of GMTI radar systems.

#### **2.3.1. Minimum Detectable/Discernible Velocity (MDV)**

Since the clutter spreads in frequency spectrum due to the Doppler shift of the clutter samples at the edges of the azimuth beamwidth and the internal clutter motion, the Doppler shifts of the targets might fall inside the clutter Doppler spread. Due to the usage of the filtering techniques to eliminate the stationary clutter, there is a limit to the minimum target Doppler frequency which can be detected without being eliminated by that filter. This minimum Doppler frequency is called the Minimum Detectable/Discernible Velocity (MDV).

A GMTI radar must distinguish a moving target from ground clutter by using the target's Doppler signature to detect the radial component of the target's velocity vector by measuring the component of the target's movement directly along the radar-target line (Figure - 2.5).

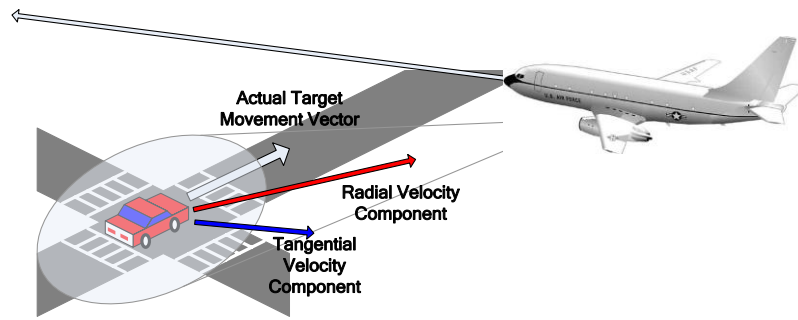


**Figure - 2.5:** Target Velocity Component According to the Radar

A radar is desired to detect targets that are moving almost tangentially to the radar (i.e., perpendicular to the radar-target line.) As the radial component of a target's velocity approaches zero, the Doppler shift of the target will fall into the clutter Doppler spread.

### 2.3.2. Target Location Accuracy

Location accuracy is a function of platform self-location performance, radar-pointing accuracy, azimuth resolution, and range resolution. A long antenna or very short wave length can provide fine azimuth resolution. Short antennas tend to have a larger azimuth error, an error that increases with range to the target because signal-to-noise ratio varies inversely with range. Location accuracy is vital for tracking performance because it prevents track corruption when there are multiple targets and makes it possible to determine which road the vehicle is on if it is moving in an area with many roads.

### 2.3.3. Target Range Resolution

The target range resolution determines whether two or more targets moving in close proximity will be detected as individual targets. Additionally, the higher the range resolution; the lower the reflected clutter power. So, for the

radars with high range resolution, the signal-to-clutter (SCR) ratio will be high enough to provide high detection probability.

For a high resolution radar, it is possible to recognize the type of the target and classify it. This is important in the operational usage.

#### 2.3.4. Clutter Attenuation

The ability of a radar to suppress undesired clutter is commonly measured by the improvement factor. To define the improvement factor, firstly, the clutter attenuation has to be defined. The clutter attenuation is simply the ratio of the clutter power at the input of the MTI filter to the clutter power at the output and is given by

$$CA = \frac{\sigma_{ci}^2}{\sigma_{co}^2} = \frac{\int_{-PRF/2}^{PRF/2} S_c(F) dF}{\int_{-PRF/2}^{PRF/2} S_c(F) |H(F)|^2 dF} \quad (2.9)$$

where  $\sigma_{ci}^2$  and  $\sigma_{co}^2$  are the clutter power at the input and output, respectively.

$S_c(F)$  denotes the sampled clutter power spectrum expressed in terms of analog frequencies, and  $H(F)$  denotes the discrete-time MTI filter frequency response.

The clutter attenuation depends on the phase difference between two consecutive pulses caused by several reasons. One of the reasons is the movement of the radar platform. Because of this motion, two consecutive pulses will be transmitted and received at slightly different positions causing a phase difference between them. If the radar uses two receive antennas, the measurement errors will also contribute to the phase difference.

#### 2.3.5. Improvement Factor

While an MTI filter reduces the clutter power, it may also reduce the power of the target signal according to the filter characteristics. The improvement factor  $I$  is defined formally as the signal-to-clutter ratio at the filter input,

averaged over all target radial velocities of interest. Considering for the moment only a specific target Doppler shift, the improvement factor can be written in the form

$$I = \frac{(S/C)_{out}}{(S/C)_{in}} = \left(\frac{S_{out}}{S_{in}}\right) \left(\frac{C_{in}}{C_{out}}\right) = G \cdot CA \quad (2.10)$$

where G is the signal gain.

### **2.3.6. Detection Probability**

The detection probability ( $P_D$ ) of a target depends on the target range, the radar range resolution, the permissible false alarm probability, the size of the antenna and the amount of power it radiates. For a constant false alarm probability, the detection probability depends on the signal-to-noise-and-clutter (SCNR) ratio. A large antenna radiating at high power provides the highest SCNR and so the best performance.

For GMTI Radars,  $P_D$  must be high enough for reliable target detection. While providing a low false alarm rate, the detection probability of a target might be the most critical property because of the probable fatal results of missing a target.

### **2.3.7. Stand-off distance**

Stand-off distance is the distance separating a radar system from the area it is covering. This distance will affect the signal-to-noise ratio (SNR) and the probability of detection. Operationally, detecting target movements far away from the observation area is a critical issue.

## **2.4. Doppler In GMTI**

In terms of the clutter characteristics, the Doppler properties are very similar between SAR (Synthetic Aperture Radar) and GMTI systems. For a moving radar, the platform motion can substantially spread the ground clutter

spectrum. We know that the Doppler shift for a radar moving at velocity  $v$  with its boresight squinted  $\varphi$  radians off the velocity vector is

$$F_D = \frac{2v}{\lambda} \cos \varphi \text{ Hz} \quad (2.11)$$

Let's say that the most squinted point of the clutter in 3 dB beamwidth of the radar antenna is P1 and the least squinted point of the clutter in 3 dB beamwidth of the radar antenna is P2 (Figure - 2.6).

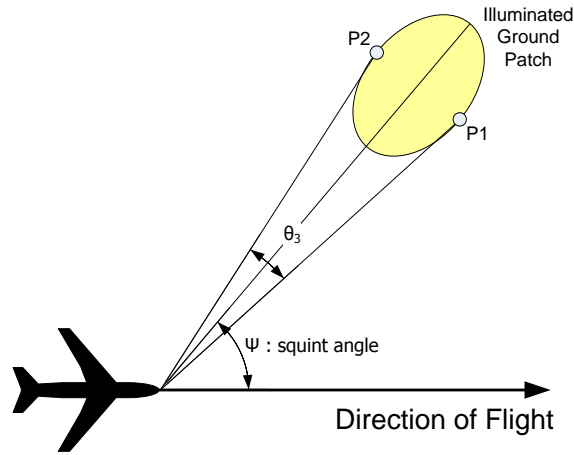


**Figure - 2.6:** Radar Illumination Area and Related Doppler Spreads

The Doppler shift of the point P1 can be written in the form

$$f_{D_{max}} = \frac{2v}{\lambda} \cos (\varphi + \theta_3/2) \text{ Hz} \quad (2.12)$$

where  $\theta_3$  is the 3 dB beamwidth of the radar antenna. Similarly, the Doppler shift of the point P2 can be written in the form

$$f_{D_{min}} = \frac{2v}{\lambda} \cos (\varphi - \theta_3/2) \text{ Hz} \quad (2.13)$$

The difference in the Doppler shift of the echoes ( $\beta_D$ ) from point P1 and P2 is then

$$\beta_D = \frac{2v}{\lambda} [\cos(\varphi - \theta_3/2) - \cos(\varphi + \theta_3/2)] \quad (2.14)$$

$$= \frac{4v}{\lambda} \sin \frac{\theta_3}{2} \sin \varphi$$

For radar antennas which have beamwidth typically less than 5 degrees, the small angle approximation to  $\sin(\theta_3/2)$  can be applied and the expression can be recast in a simpler form:

$$\beta_D \approx \frac{2v \theta_3}{\lambda} \sin \varphi \text{ Hz} \quad (2.15)$$

The center of the clutter spectrum is given by

$$\beta_c = \frac{2v}{\lambda} \cos \varphi \text{ Hz} \quad (2.16)$$

These values are shown in Figure - 2.7. In this figure, the Doppler spectrum for airborne radar is given. There is a strong signal return from the altitude direction of the aircraft, which has a Doppler spread around the zero Doppler axes. The main beam clutter may have a Doppler shift because of the squint angle and a Doppler spread because of the width of the azimuth beamwidth of the radar antenna. The nadir clutter appearing around the zero Doppler frequency is caused by the altitude line returns of the aircraft.

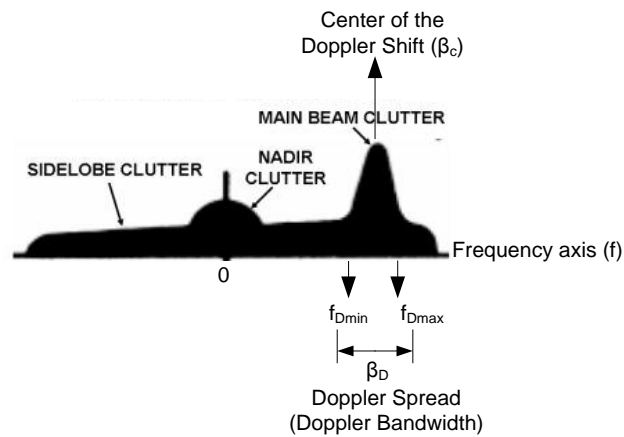


**Figure - 2.7:** Doppler Spectrum for an Airborne Radar []

The purpose of the GMTI radars is to detect the targets moving on the ground in spite of this ground clutter spectrum. There are two modes of GMTI radars according to the target Doppler spectrum.

For the fast moving targets, the Doppler shift of the target can stand outside the Doppler spread of the clutter (Figure – 2.8). The techniques used to detect these targets are called as “Exo-clutter GMTI” techniques. The ordinary MTI techniques can overcome this detection problem.

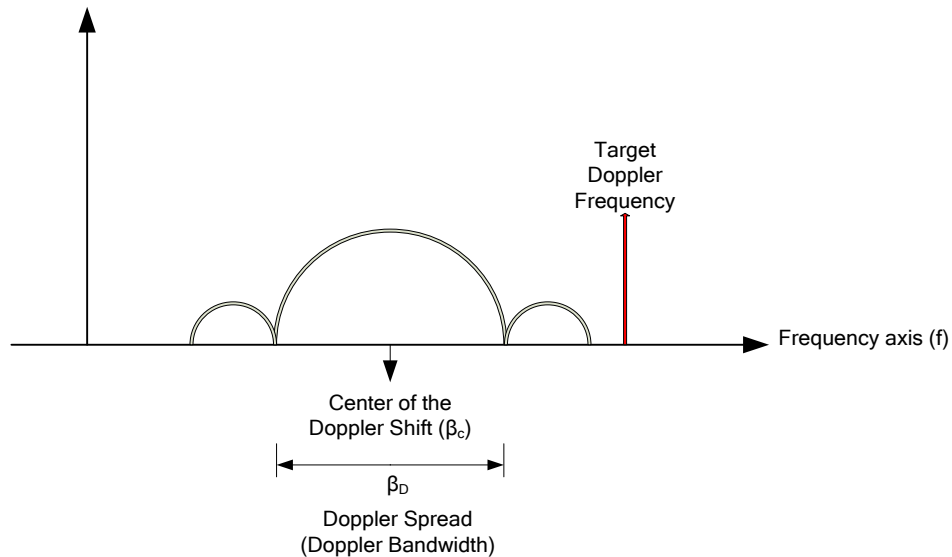


**Figure – 2.8:** Doppler Spectrum for Exo-Clutter GMTI

But for the slow moving targets, the problem is more complicated. The Doppler shift of these types of targets can fall inside the clutter Doppler spread (Figure – 2.9). The techniques used to detect these targets are called as “Endo-clutter GMTI” techniques. The ordinary MTI techniques are not suitable for this problem. The techniques that can be used to overcome this difficulty will be analyzed in this thesis.

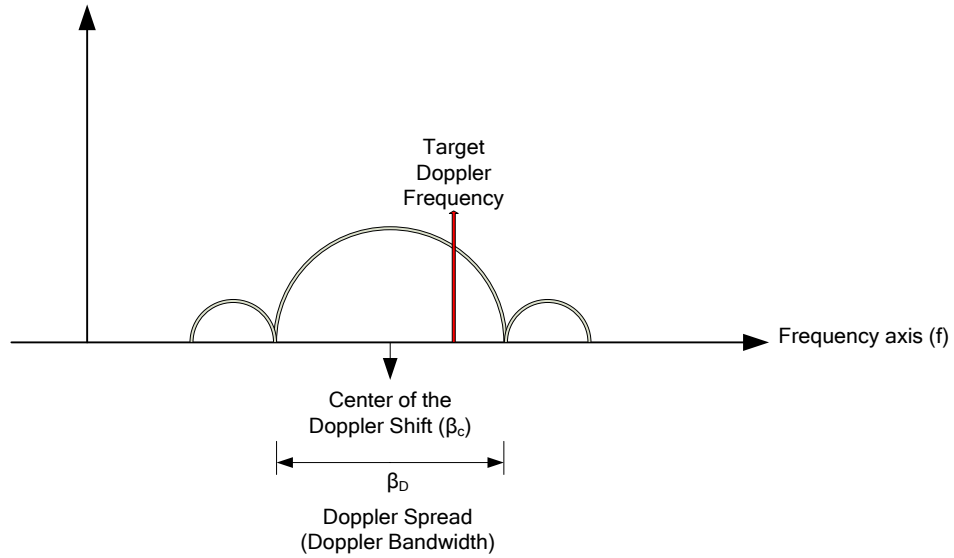


**Figure – 2.9:** Doppler Spectrum for Endo-Clutter GMTI

A stationary target has a Doppler history according to moving radar. The range of the target will change with the movement of the radar platform. The change in range will cause a change in phase of the target’s echo signal. The time derivative of this phase will give the Doppler frequency change of the target, which can be shown as given below:

$$F_D(t) = -\frac{2v^2}{R_o \lambda_t} t \quad (2.17)$$

Thus, the Doppler shift of the received signal varies linearly due to the changing radar-target geometry.

Figure – 2.10 – b shows the Doppler history of a stationary target according to the radar on an aircraft flying as shown in Figure – 2.10 – a.

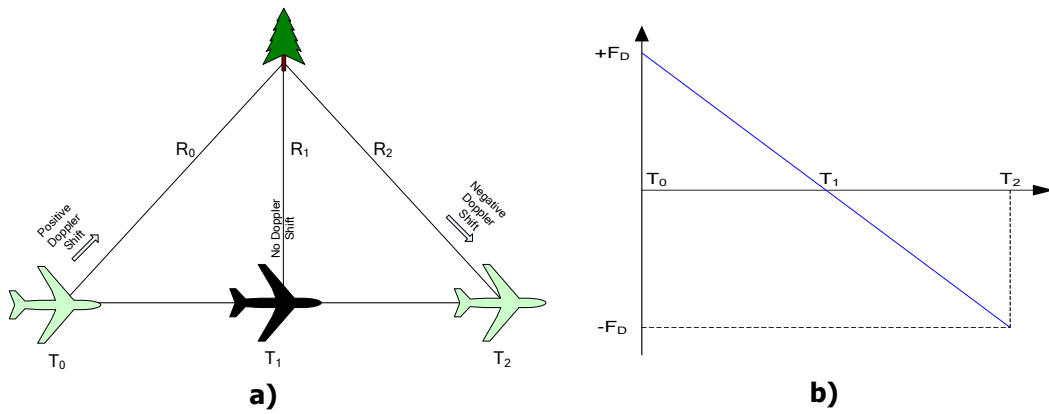


**Figure – 2.10:** a) Different Positions of Radar in the Flight b) Related Doppler History

In Figure – 2.10 – b, the Doppler shift of the received signal reflecting from the stationary target is shown.

The calculation of the Doppler frequency change for a target moving with constant velocity is given below.

The Doppler history changes according to the motion of the target. If there is a target at P having velocity components  $V_x$  and  $V_y$  in x and y direction and a radar having a velocity component  $V_{Rx}$  in x direction (Figure – 2.11), the instantaneous coordinates of the target and the radar can be written as:

$$P_{radar} = (V_{Rx} t, 0, r_0 \sin \delta) = (X_r, Y_r, Z_r) \quad (2.18)$$

$$P_{target} = (r_0 \cos \delta \cos \theta + V_x t, r_0 \cos \delta \sin \theta + V_y t, 0) = (X_t, Y_t, Z_t) \quad (2.19)$$

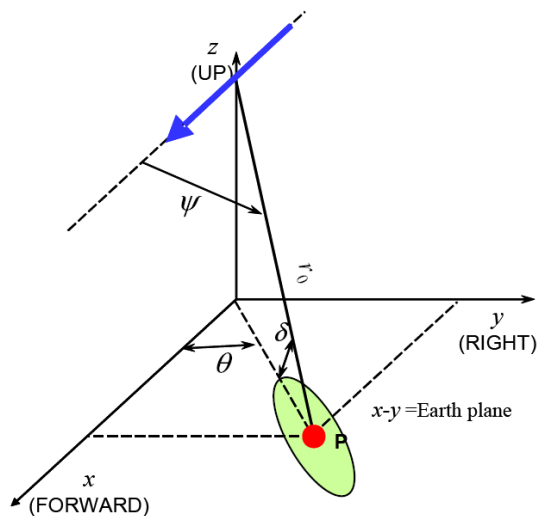


**Figure – 2.11:** Radar and Target Locations and Velocities

The range between these two targets can be written in Euclidean form taking the time into account.

$$\begin{aligned}
 r(t) &= \sqrt{(V_{Rx}t - r_0 \cos\delta \cos\theta - V_x t)^2 + (r_0 \cos\delta \sin\theta + V_y t)^2 + (r_0 \sin\delta)^2} & (2.20) \\
 &= \sqrt{t^2((V_{Rx} + V_x)^2 + V_y^2) + t(2r_0 \cos\delta(V_y \sin\theta - (V_{Rx} + V_x)\cos\theta)) + r_0^2} \\
 &= r_0 \sqrt{\left(1 + \frac{2t \cos\delta}{r_0}(V_y \sin\theta - (V_{Rx} - V_x)\cos\theta) + \frac{t^2((V_{Rx} - V_x)^2 + V_y^2)}{r_0^2}\right)}
 \end{aligned}$$

If we apply the series expansion of the square root as

$$\sqrt{1-x} = 1 - \frac{1}{2}x - \frac{1}{8}x^2 + \dots \quad (2.21)$$

we can approximate  $r(t)$  as:

$$\begin{aligned}
 r(t) &= r_0 \left\{ 1 + \frac{t \cos\delta}{r_0}(V_y \sin\theta - (V_{Rx} - V_x)\cos\theta) \right. & (2.22) \\
 &\quad \left. + \frac{t^2 \cos^2\delta}{2r_0^2}(V_y \sin\theta - (V_{Rx} - V_x)\cos\theta)^2 \right\}
 \end{aligned}$$

We can write the phase as a function of time in the form given below:

$$\begin{aligned}
 \Phi(t) &= -\frac{4\pi}{\lambda}r(t) & (2.23) \\
 &= -\frac{4\pi r_0}{\lambda} \left\{ 1 + \frac{t \cos\delta}{r_0}(V_y \sin\theta - (V_{Rx} - V_x)\cos\theta) \right. \\
 &\quad \left. + \frac{t^2 \cos^2\delta}{2r_0^2}(V_y \sin\theta - (V_{Rx} - V_x)\cos\theta)^2 \right\}
 \end{aligned}$$

The derivative of the phase gives the frequency change as a function of time.

$$F_D(t) = \frac{1}{2\pi} \frac{d\Phi(t)}{dt} \quad (2.24)$$

$$\approx -\frac{4\pi r_0}{\lambda} \left\{ \frac{\cos\delta}{r_0} (V_y \sin\theta - (V_{Rx} + V_x) \cos\theta) + \frac{t \cos^2\delta}{r_0^2} (V_y \sin\theta - (V_{Rx} + V_x) \cos\theta)^2 \right\}$$

For a stationary target, the velocity components of the target should be taken as zero. For a target having a velocity component only in the direction perpendicular to the flight axis and approaching to the radar, there will be a positive Doppler offset in the Doppler frequency history (Figure – 2.12 – a). If the target moves away from the radar in the same direction, the Doppler offset will be negative (Figure – 2.12 – b).

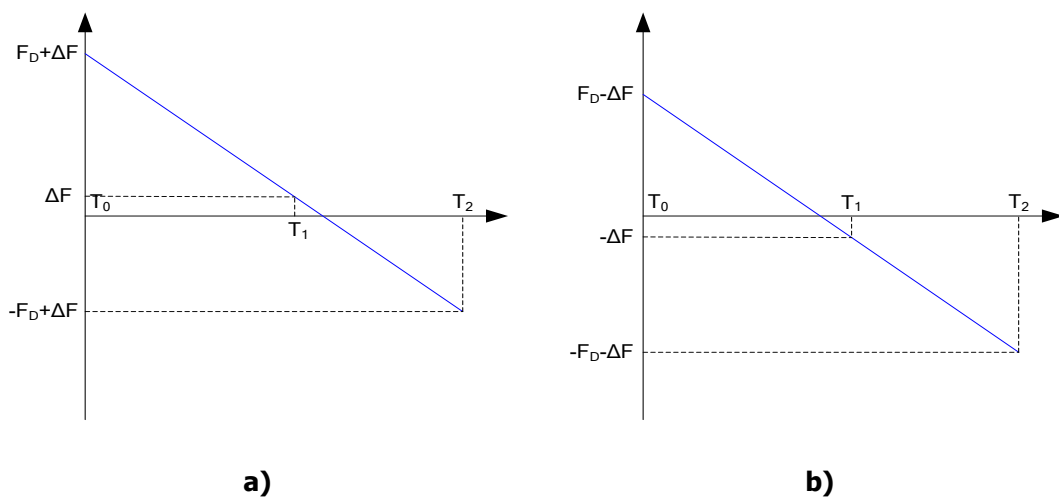


**Figure – 2.12:** Doppler History for a Target a) Approaching to the Radar Flight Direction b) Withdrawing from the Radar Flight Direction

For a target having a velocity component only in the opposite direction of the flight, the minimum and the maximum values of the Doppler shifts at times  $T_0$  and  $T_2$  will increase (Figure – 2.13 – a). If the target moves in the same direction with the aircraft, the minimum and the maximum values of the Doppler shifts at times  $T_0$  and  $T_2$  will decrease (Figure – 2.13 – b).

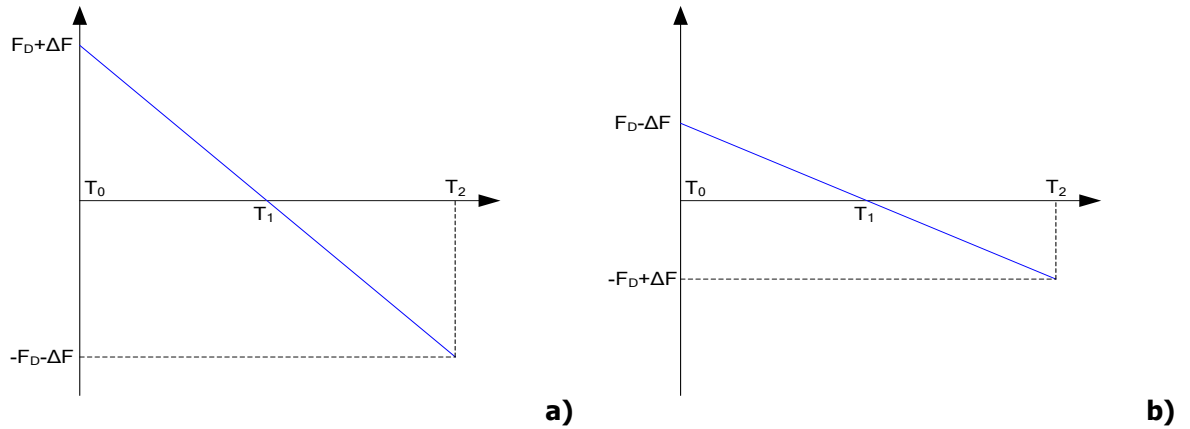


**Figure – 2.13:** Doppler History for a Target a) Moving Same Direction with Radar b) Moving Opposite Direction with Radar

In GMTI Radars, the general purpose is to detect the radial velocity of targets. For the far looking, narrow beam GMTI radars, target movements in the flight direction cause very low Doppler shifts. These Doppler shifts are negligible. The main Doppler shift is caused by the movements of the target in the direction perpendicular to the flight axis.

## 2.5. Clutter Structure

There are two important features of the clutter structure for airborne radars. These are the distribution and the correlation of the clutter samples.

The clutter distribution depends on the observation area. For the land, sea and weather clutters, the distributions are different. Before discussing the clutter structure of GMTI systems, the point scatterer structure of a single clutter patch must be studied.

The size of the ground patches of the radar beam can be calculated by the formula given in Section 2.3. For each range bin, the size of the ground patch will be different (Figure – 2.14).

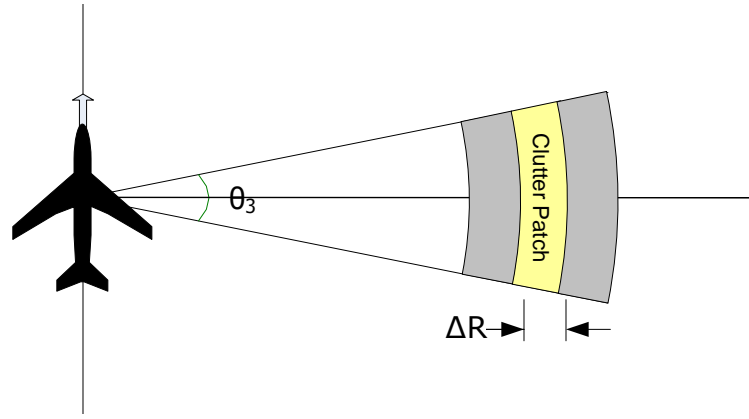


**Figure – 2.14:** Clutter Patch for a Side Looking Radar

Using the complex envelope notation, the clutter component of each sample of the received signal can be represented as

$$a = \alpha + j\beta \quad (2.25)$$

where  $\alpha$  and  $\beta$  denote the in-phase and quadrature components, respectively. It will be assumed that  $\alpha$  and  $\beta$  are independent identically distributed (i.i.d.) random variables. The probability density function of I and Q components is called the “marginal pdf” and will be denoted as

$$f_m(\alpha) = f_m(\beta). \quad (2.26)$$

The probability density function of the magnitude of the clutter is called the “envelope pdf” and is denoted as

$$f_s(|a|). \quad (2.27)$$

The probability density function of the magnitude square of the clutter is called the “power pdf” and is denoted as

$$f_p(aa^*) = f_p(|a|^2). \quad (2.28)$$

For land clutter, Weibull envelope pdf is a commonly used distribution in the literature, [26]. But providing the correlation between samples received from the same range bins is rather difficult for Weibull distribution. Another model

proposed in the literature for land clutter uses K-distributed envelope pdf, [26]. In fact, both Weibull and K-distributions can be made to have quite similar characteristics by appropriate choice of their shape parameter. The generation of correlated K-distributed complex clutter samples is explained in Section 4.3.

The correlation of the clutter samples between pulses depends on the operation type of the radar. There are two basic parameters affecting the clutter correlation. These are the antenna motion and the internal clutter motion (ICM). For air surveillance radars, the clutter correlation mainly depends on the antenna rotation rate, but for side-looking airborne radars, it depends on the flight velocity.

While the aircraft moves along the flight direction, radar will send pulses perpendicular to it. In each pulse, the area that radar looks at will be slightly different from the previous area (Figure – 2.15).

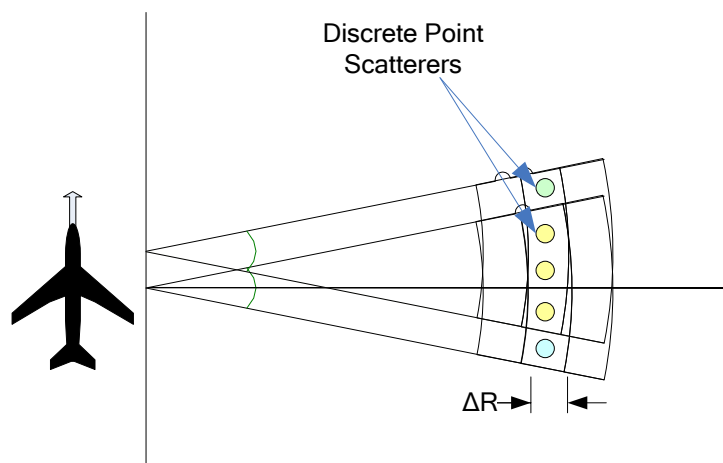


**Figure – 2.15:** Point Scatterers in the Clutter Patches

Each clutter patch can be thought of as a sum of point scatterers whose total radar cross section can be calculated according to the range resolution, the azimuth beamwidth, the radar look angle and the squint angle.

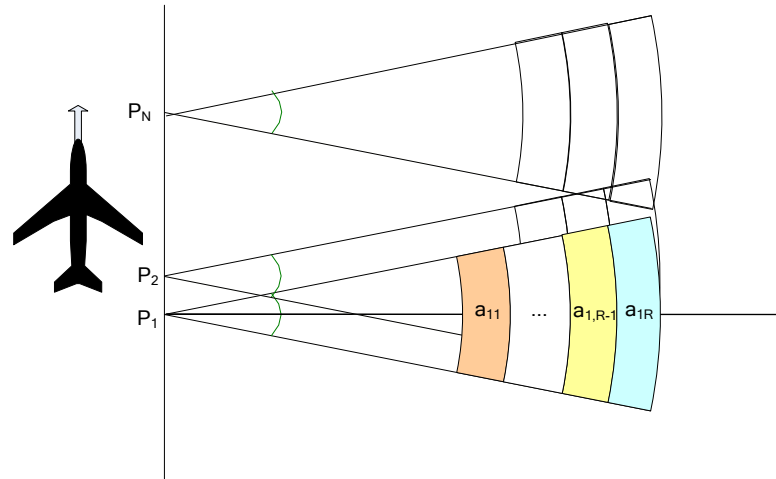


**Figure – 2.16:** Complex Clutter Samples in the Range Bins Collecting in each Pulse

At each location of the platform where the radar transmits the pulses, the clutter patch seen by the radar is slightly different from the clutter patch seen by the radar in the previous pulse. This small change causes a decorrelation in the clutter samples even if the clutter is completely stationary.

Another factor affecting the clutter correlation is the internal clutter motion. The reflection of each point scatterer in the observation area seen by the radar changes slightly during the flight because of the small motions of each scatterer. Trees' swinging through the wind is an example of this small motion.

Autocorrelation is useful for finding repeating patterns in a signal, such as determining the presence of a periodic signal which is buried under noise, or identifying the fundamental frequency of a signal which doesn't actually contain that frequency component, but implies it with many harmonic frequencies. If we say that  $\mathcal{R}(x)$  is the autocorrelation function (ACF) of the vector  $x$ ,  $\mathcal{R}(x)$  has an impulsive characteristic for a noise like vector  $x$  whose repeating pattern is only itself.

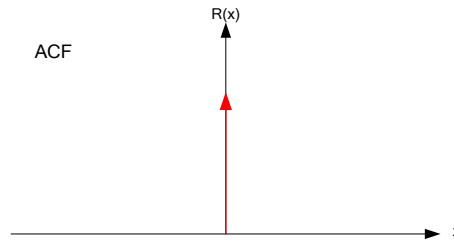


**Figure – 2.17:** Autocorrelation Function of a Noise-like Vector  $x$

For a vector  $x$  having a periodicity or continuity, the autocorrelation function doesn't have an impulsive characteristic.

Let's define  $x$  as the complex reflection coefficients of a point scatterer during the flight at the locations where the radar transmits the pulses.

$$x = [a_1 \ a_2 \ \dots \ a_3] \quad (2.29)$$

If the reflection of the point scatterer doesn't change during the flight as explained in previous paragraphs, i.e. the internal clutter motion is low, the autocorrelation of  $x$  will have a flat characteristic. But if the reflection of the point scatterer changes during the flight due to the wind or any similar effect, i.e. the internal clutter motion is high, the autocorrelation of  $x$  will have an impulsive characteristic.

For side-looking radars, the internal clutter motion is a dominant effect in the clutter correlation. In Section 4.3, the ICM generation and its parameters are explained in detail.

In this thesis, the computer generation of clutter samples having a covariance matrix is discussed in Chapter 4 and the effects of different clutter covariance matrix structures are analyzed.

## CHAPTER 3

### GMTI TECHNIQUES

#### 3.1. Displaced Phase Center Antenna (DPCA)

*Displaced Phase Center Antenna (DPCA)* Processing is a technique used to eliminate the clutter effects from the radar input signal by taking into account the platform motion and the radar parameters, [1, 17]. It is based on the side looking antenna arrangement with two or more phase centers (Figure – 3.1). The aircraft motion can then be compensated by choosing the pulse repetition frequency (PRF) so that the second phase centre occurs at the position of the first phase centre after an integer multiple of pulse repetition intervals (PRI).

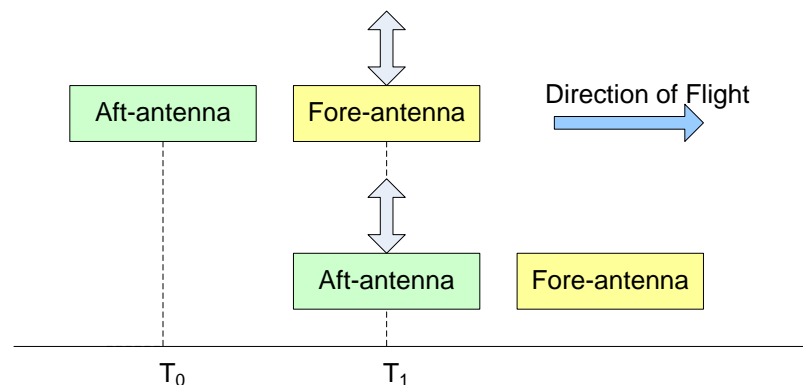


**Figure – 3.1:** DPCA Antenna Alignment Geometry

The aim of holding the phase centers at the same point is to make the antenna appear stationary even though the platform is moving forward.

DPCA processing tries to perform an effective MTI cancellation by combining the pulses measured at the same phase center by aft and fore antennas. The time between  $T_0$  and  $T_1$  is called as “slip time” ( $T_s$ ). To achieve a successful cancellation, there must be an integer number ( $M_s$ ) of pulses between  $T_0$  and  $T_1$  (Figure – 3.2).

$$M_s = \frac{T_s}{PRI} : Integer \quad (3.1)$$

$M_s$  is called as the “time slip pulses”.

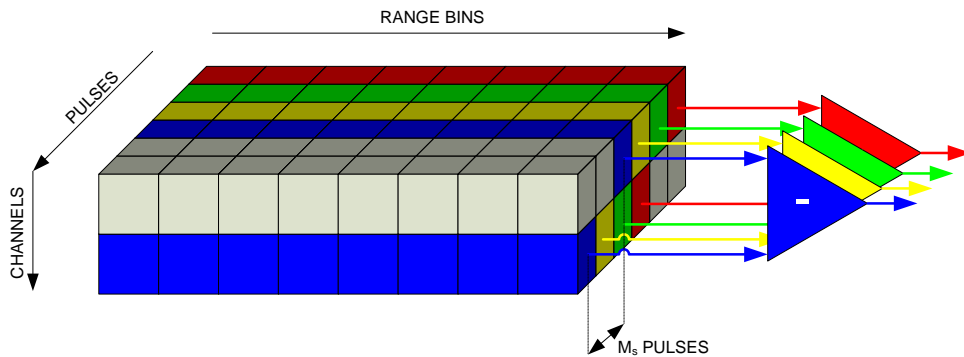


**Figure – 3.2:** DPCA Processing Block Diagram

Let  $y[l, m]$  represent the measurements taken from fore and aft antennas.

$$y[l, m] = \begin{bmatrix} y_f[l, m] \\ y_a[l, m + M_s] \end{bmatrix} \quad (3.2)$$

The process shown in Figure – 3.2 can be expressed with the formula given below:

$$\begin{aligned} z[l, m] &= y'[l, m] \begin{bmatrix} 1 \\ -1 \end{bmatrix} \\ &= [y_f[l, m] \quad y_a[l, m + M_s]] \begin{bmatrix} 1 \\ -1 \end{bmatrix} \\ &= y_f[l, m] - y_a[l, m + M_s] \end{aligned} \quad (3.3)$$

where  $z[l, m]$  is the output of DPCA processor.

There are some important parameters affecting the DPCA performance. First of all, DPCA performance depends on the phase matching between fore and aft antenna channels. Any phase mismatch may cause performance degradation in MTI cancellation. Besides, any phase center alignment mismatch causes the same effect with the phase mismatch in the antenna channels.

Another important issue is the clutter decorrelation. The larger the distance between fore and aft antennas, the larger the slip time. This means that the correlation of clutter samples received by the two antennas will decrease as the slip time increases, causing incomplete clutter cancellation.

DPCA performance depends on SNR. The correlation between measurements taken by the fore and aft antennas decreases with the increasing amount of noise. Some possible noise sources affecting the DPCA performance are:

- Additive White Gaussian Noise (AWGN)
- Phase errors caused by the timing jitter of oscillators in transmitter and receiver
- Multiplicative phase noises caused by positioning errors of the radar system

Because of these noise sources, the stationary ground clutter cannot be eliminated completely.

If there were only a single point scatterer exactly at the center of the main beam of the fore antenna, the phase error would be very small, since the Doppler shift of such a target would be zero.

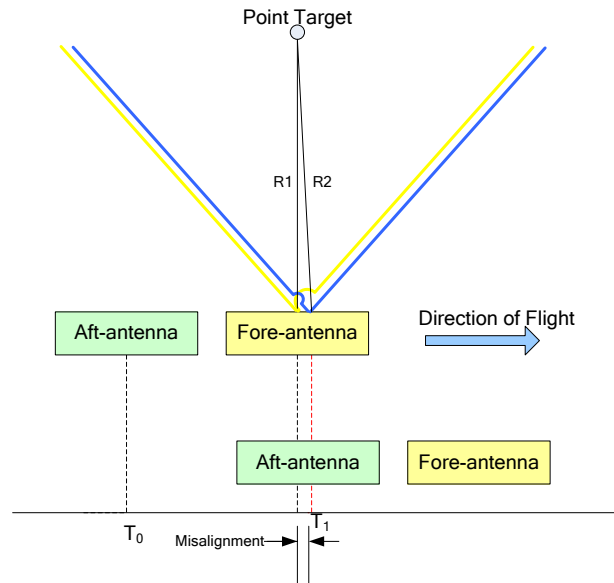


**Figure – 3.3:** DPCA Antenna Misalignment

But this is never the case in practice. Some reflection will return to the radar from very wide angles covered by the antenna pattern. If the boresights of the fore and aft antennas are misaligned, the phase error will increase due to accumulation of the phase differences of individual scatterers within the azimuth beamwidth (Figure – 3.3). This accumulative phase error will increase with increasing azimuth beamwidth.

DPCA processing is a simple but yet quite effective GMTI technique and is being used even in current GMTI systems like E-8 Joint STARS. But because of the weaknesses mentioned above, other adaptive techniques are being studied.

### 3.2. Adaptive DPCA

Even if the time alignment in PRF setting according to the flight velocity is perfect in a DPCA application, there may still be some phase center alignment mismatches. This is because the phase centers of antennas are not exactly known, and may change with frequency. A fraction of a wavelength error in the exact location of antenna phase center will degrade

the performance of DPCA technique. For X-band radars, this means that location errors of a few millimeters are not tolerable.

This suggests the use of adaptive DPCA techniques in which the phase center locations are inherently generated from the received data, [1, 21]. For the best performance of DPCA processing in clutter cancellation, there must not be any phase center misalignments.

The number of time slip pulses must be an integer for DPCA processing to achieve perfectly matched phase centers between fore and aft antennas. But, in the case of non-integer time slip pulses, the phase centers will not be at the same position and there will be degradation in the clutter cancellation. To overcome this problem, adaptive DPCA presents a subband-based solution. The technique is used as dividing each received signal channel into Doppler subbands using DFT and performing the cancellation independently in each subband. This subband-based solution allows us to optimize the cancellation weights independently for each sub-Doppler band.

The vector approach will be used to develop the adaptive filtering. The coarse-aligned two-channel signal vector is defined as

$$\mathbf{y}[l, m] = \begin{bmatrix} \mathbf{y}_f[l, m] \\ \mathbf{y}_a[l, m + M_s] \end{bmatrix} \quad (3.4)$$

where  $\mathbf{y}_f[l, m]$  is the fore channel and  $\mathbf{y}_a[l, m]$  is the aft channel received vectors. Here, the index  $l$  represents the range bins and the index  $m$  represents the slow time pulses.

The maximum length of  $m$  depends on the coherent processing interval (CPI). The maximum number of pulses that can be collected in CPI is denoted by  $M$ . This means that we can process  $M$  pulses for Fourier transformation without losing the coherency.

To pass to the Doppler domain for each channel, a K point discrete Fourier transform is taken in each range bin of each channel. The number K is commonly chosen as a power of 2 to facilitate a radix-2 FFT algorithm. The Doppler domain vectors are shown as:

$$\mathbf{Y}[l, k] = \begin{bmatrix} \mathbf{Y}_f[l, k] \\ e^{-j2\pi M_s k/K} \mathbf{Y}_a[l, k] \end{bmatrix} \quad (3.5)$$

A phase correction is done here to compensate for the phase difference between fore and aft antennas. The linear phase term used for the correction includes the misalignment corrections also (Figure – 3.4).

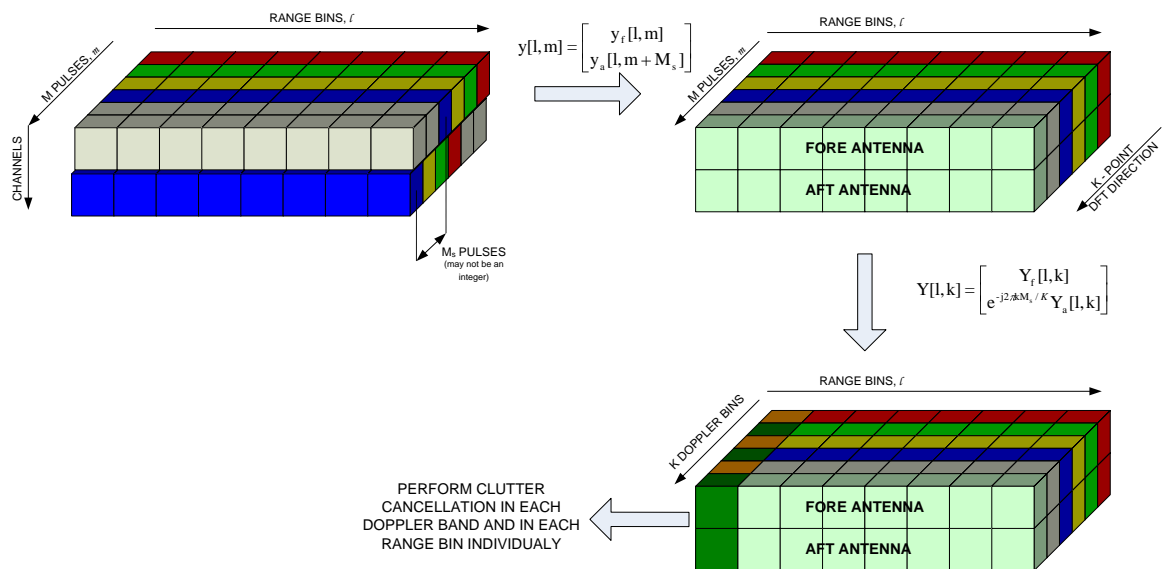


**Figure – 3.4:** Adaptive DPCA Processing Block Diagram

For a side looking antenna, the clutter spreads around DC due to the platform motion and the antenna azimuth beamwidth. This means that the clutter is not white in Doppler domain and its magnitude changes in each subdoppler band. But the noise is white and uncorrelated between channels. The signals at each subband consist of clutter, noise and if present target components (Figure – 3.5).

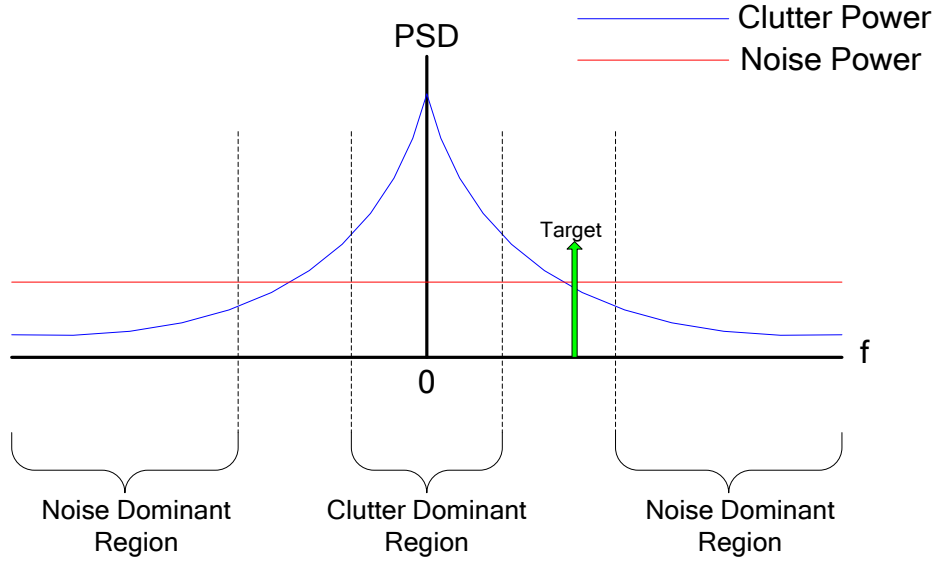


**Figure – 3.5:** Power Spectral Density of Noise and Clutter

For the interference elimination to maximize the SINR (signal to clutter plus noise ratio), a model of covariance matrix ( $\mathbf{S}_I$ ) is needed. Normally,  $\mathbf{S}_I$  has to be found individually in each range bin. But it also has to be found for each subband having different characteristics.

So,  $\mathbf{S}_I$  will take the form given below:

$$\mathbf{S}_I[l, k] = \begin{bmatrix} \sigma_c^2[l, k] + \sigma_n^2 & \rho[l, k]\sigma_c^2[l, k] \\ \rho^*[l, k]\sigma_c^2[l, k] & \beta[l, k](\sigma_c^2[l, k] + \sigma_n^2) \end{bmatrix} \quad (3.6)$$

where  $\rho$  is the clutter correlation coefficient and  $\beta$  is the phase and amplitude mismatch coefficient between fore and aft antenna channels.

For the radar systems having small swath widths, the clutter power variation will not be high. Noise power is already independent from the range and Doppler and its power is same for all regions. So, it can be assumed that the covariance matrix is the same for all range bins and varies only with Doppler. Then,  $\mathbf{S}_I$  can be written as:

$$\mathbf{S}_I[k] = \begin{bmatrix} \sigma_c^2[k] + \sigma_n^2 & \rho[k]\sigma_c^2[k] \\ \rho^*[k]\sigma_c^2[k] & \beta[k](\sigma_c^2[k] + \sigma_n^2) \end{bmatrix} \quad (3.7)$$

The exact clutter and noise statistics are not known a priori. Although it cannot be known exactly as an a priori data, it can be estimated from the neighboring range bins.  $\hat{S}_I$  can be computed as the sample average over several range bins (Figure – 3.6).

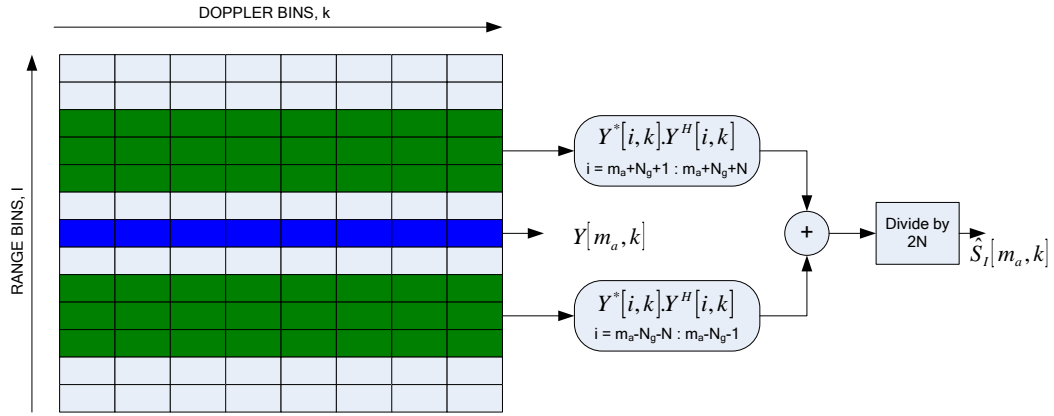


**Figure – 3.6:** Block Diagram of Clutter Covariance Matrix Estimation from Neighbor Range Bins

If a target is present in the test range bin, some guard range bins has to be used to decrease the effect of the present target while estimating the covariance matrix. The formula given below can be used for covariance matrix estimation:

$$\hat{S}_I[l, k] = \frac{1}{2N} \sum_{\substack{a=-N-N_g \\ -N_g < a < N_g \text{ is not included}}}^{N+N_g} Y[a, k] \cdot Y^H[a, k] \quad (3.8)$$

This formula shows that covariance matrix must be calculated for all range bins individually. But, in adaptive DPCA processing, covariance matrix is also calculated for each Doppler bin.

In adaptive DPCA, the adaptive weights are determined from the neighboring range bins with some guard cells. But this process is based on the assumption of a homogeneous clutter environment. For inhomogeneous clutter environments, clutter correlation between neighbor range bins will be low. In this case, the number of neighbor range bins used to estimate the

clutter covariance matrix must be decreased. In highly inhomogeneous clutter environments, this number becomes very small and other techniques are required to estimate the clutter covariance matrix.

After calculating the estimate of the clutter covariance matrix, optimum filter weights can be found by the formula [1]

$$\mathbf{h}_{opt}[l, k] = \mathbf{S}_l^{-1}[l, k] \mathbf{t}[l, k]^* \quad (3.9)$$

where  $\mathbf{t}^*$  is the column vector representing the desired target signal to which the filter is matched and the asterisk denotes the complex conjugate [1]. The Doppler domain target vector can be written in the form given below:

$$\mathbf{t}[l, k] = MA_t \delta[l - l_t] \delta[k - k_t] [\gamma_f \ e^{-j2\pi M_s k/K} \gamma_a] \quad (3.10)$$

where  $A_t$  denotes the complex amplitude coefficient of the target signal and  $\delta$  is the impulse representation of the range and velocity information of the target and

$$\gamma_f = \exp \left[ j \frac{2\pi}{\lambda_k} (2R + \theta_f) \right], \quad (3.11)$$

$$\gamma_a = \exp \left[ j \frac{2\pi}{\lambda_k} (2R + \theta_a + \Delta\phi) \right]. \quad (3.12)$$

The term  $(4\pi/\lambda_k)R$  appearing in each channel is due to the two-way distance to the target, assumed to be at range  $R$ . The terms  $\theta_f$  and  $\theta_a$  represent the receiver phase shifts, which are different for each channel in general.  $\Delta\phi$  is the phase shift caused by the distance between fore and aft antenna channels and can be calculated as:

$$\Delta\phi = \frac{2\pi}{\lambda} d \cdot \sin(\theta_{3dB-az}/2) \quad (3.13)$$

Here,  $d$  is the distance between fore and aft antennas and  $\theta_{3dB-az}$  is the 3 dB azimuth beamwidth of the antennas.

The output vector  $z$  will be:

$$\mathbf{z} = \mathbf{h}'_{opt} \mathbf{y} = \mathbf{t}^H (\mathbf{S}_I^{-1})^* \mathbf{y} \quad (3.14)$$

$\mathbf{y}$  denotes the coarse-aligned two-channel signal vector  $\mathbf{Y}[l, k]$ . This formula has to be written in Doppler domain, because the filtering is done in each Doppler subband.

$$\mathbf{z}[l, k] = \mathbf{t}^H[l, k] (\mathbf{S}_I^{-1}[k])^* \mathbf{Y}[l, k] \quad (3.15)$$

### 3.3. Along Track Interferometry (ATI)

The Along-Track Interferometry (ATI) processing is a technique similar to DPCA processing but the main difference is taking correlation between measurements of fore and aft antennas instead of taking the difference of them, [7, 11] (Figure – 3.7).

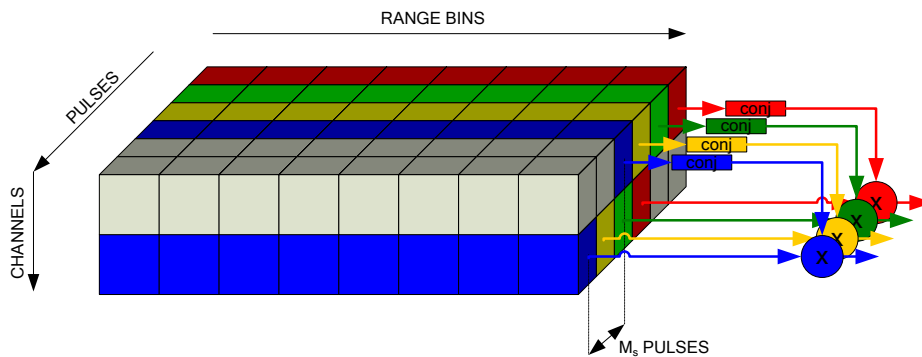


**Figure – 3.7:** ATI Processing Block Diagram

This technique is not a clutter suppression process. It uses the linear phase change of the target to distinguish it from the clutter and noise.

When viewed in the complex plane as a two dimensional distribution (imaginary part vs. real part), the complex signal output results in a fin-like histogram. The stationary scatterers are represented by their phase-noise distribution about the positive, real axis. Moving targets appear at nonzero

angles (measured from the positive real axis) that are proportional to the radial velocity of the targets (Figure – 3.8).

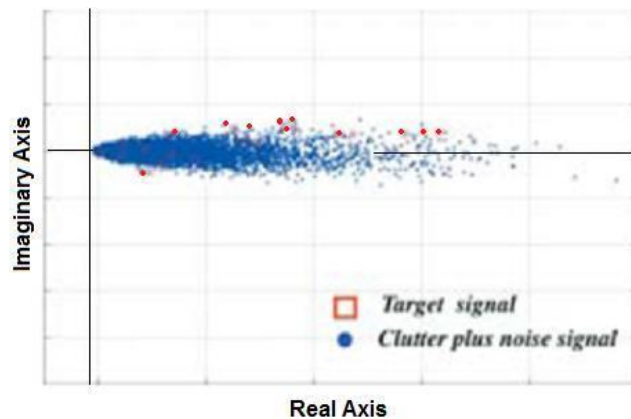


**Figure – 3.8:** Distribution of Clutter Samples in Complex Plane After Correlation

When viewed in the complex plane as a two-dimensional (2D) magnitude (radius) and phase (angle) distribution, the complex signal output of the ATI processor results in a bell-shaped distribution as seen in Figure- 3.9.

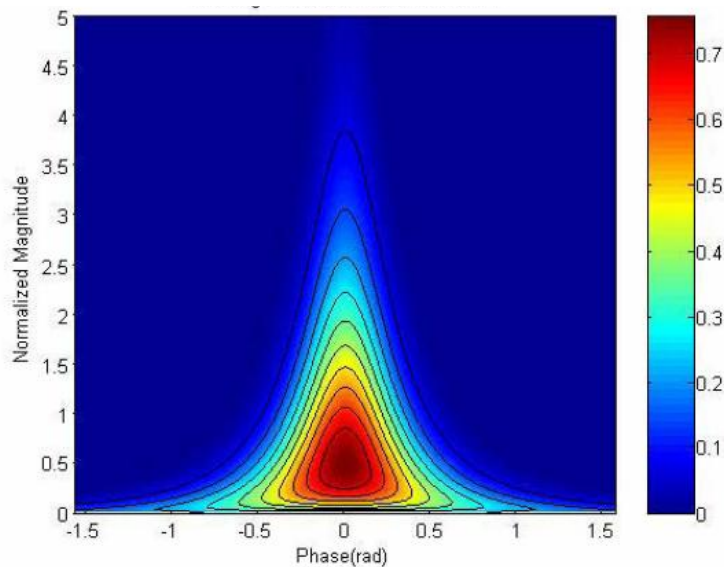


**Figure – 3.9:** Magnitude vs. Phase Distribution of Clutter at the ATI Processor Output

Signal-to-interference plus noise ratio (SINR) doesn't change the phase angle of the moving target. It only changes the amplitude of the complex sample. The shape of the interference signal representing the clutter and noise changes according to the CNR (Clutter-to-Noise Ratio). For low CNR values;

i.e. if the noise is more dominant than the clutter, the interference signal spreads over the phase axis. This is because the correlation output of noise signal might have a phase angle between  $-\pi$  to  $\pi$  (Figure – 3.10). For high CNR values; i.e. if the clutter is more dominant than the noise, the interference signal peaks at the zero phase angle point. The reason of this is that the correlation values are high for stationary clutter samples. In the case of high internal clutter motion (ICM) situation, the interference signal also spreads onto the phase axis even for the high CNR state [23].

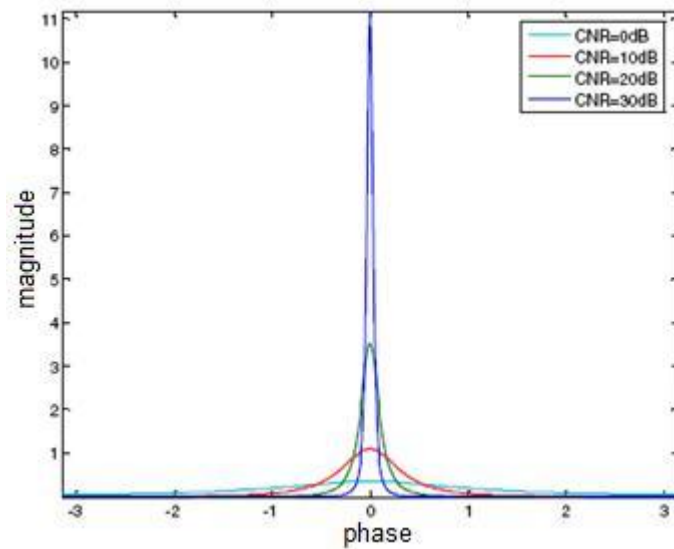


**Figure – 3.10:** Magnitude vs. Phase Distribution of Interference According to CNR

Let  $y_f[l, m]$  represent the measurements taken from fore antenna and  $y_a[l, m + M_s]$  represent the measurements taken from aft antenna. The process shown in Figure – 3.7 can express with the formula given below:

$$z[l, m] = y_f^*[l, m].y_a[l, m + M_s] \quad (3. 16)$$

where  $z[l, m]$  is the output of ATI processor.

In ATI processing, observation time is very important. For long observation time, target phase angle can change rapidly and cannot be distinguished from the noise and clutter samples. For the short observation times, complex

correlation output samples of a target distributed on the complex plane are more consistent and they have the same phase angle showing the ratio between real and imaginary components. But for very short observation times, energy would be a problem.

### 3.4. $\Sigma - \Delta$ STAP

Airborne surveillance radar systems operate in a dense interference environment. The interference is a sum of clutter, other moving objects, possible electronic counter measures (ECM) and noise. The ability to detect weak ground targets requires the suppression of interference in real time. Space-Time Adaptive Processing (STAP) techniques promise to be the best means to suppress such interference [13, 20, 22, 24].

The goal of adaptive processing is to weight the received space-time data vectors to maximize the output signal-to-interference plus noise ratio (SINR). Traditionally, the weights are determined based on an estimated covariance matrix of the interference. The weights maximize the gain in the look direction (Figure – 3.11).

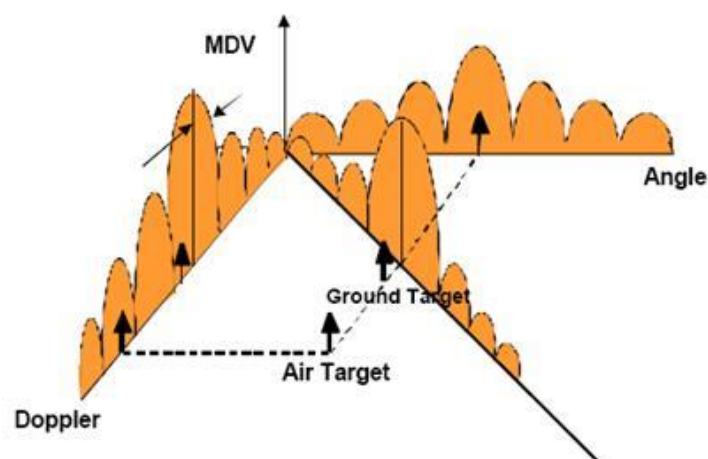


**Figure – 3.11:** Angle and Doppler Domains of STAP

For an airborne radar, the clutter in a given range cell has a structure determined by the motion of the aircraft platform and the azimuth beamwidth of the antenna. The larger is the aircraft velocity; the larger is the clutter spread in the Doppler spectrum. A slow moving ground target at the center of the main beam is closely spaced to mainlobe clutter in the Doppler domain. But a fast moving ground target at the center of the main beam is widely spaced from the mainlobe clutter. The aim of STAP processing is to put nulls in spatial and temporal dimensions.

DPCA and adaptive DPCA are the sub branches of the general STAP processing. For DPCA processing, any phase center misalignment in temporal domain cause a shift for null spacing in spatial domain. The phase center misalignments are corrected in some degree in the adaptive DPCA processing. But both of them are very dependent on the phase center alignments of the fore and aft antennas.

In  $\Sigma - \Delta$  (Sigma-Delta) STAP, measurements are taken from two antennas through two different channels. One of the channels is the sum channel and the other channel is the difference channel (Figure – 3.12).

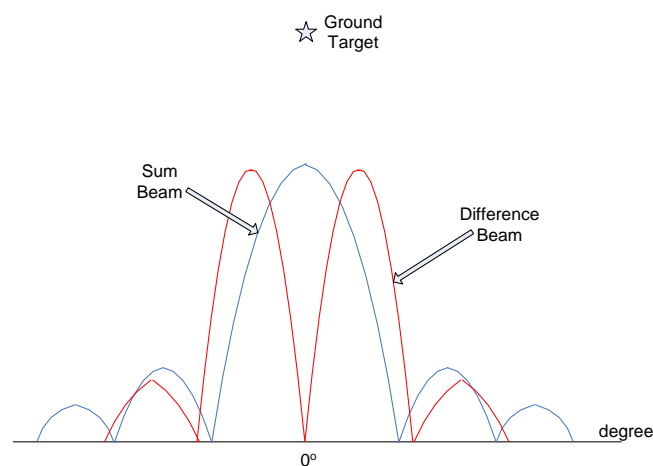


**Figure – 3.12:** Sum and Different Beams used in  $\Sigma - \Delta$  STAP

A moving target in the boresight direction will have an effect on the signal at the sum channel and no effect on the signal at the difference channel.

The sum and difference channels can be represented simply in a convenient form given below:

$$\mathbf{x} = \begin{bmatrix} x_{\Sigma} \\ x_{\Delta} \end{bmatrix} \quad (3.17)$$

Here,  $x_{\Sigma}$  is the data vector measured and sampled from the sum channel and  $x_{\Delta}$  is the data vector measured and sampled from the difference channel.

Two methods to eliminate the unwanted clutter and to detect moving targets are given below.

First method is the Pre-Doppler  $\Sigma - \Delta$  STAP [14]. In this method, adaptive cancellation weights are calculated before Doppler processing.

To calculate the adaptive filter weights, the covariance matrix has to be estimated. The correlation matrix can be written as:

$$\mathbf{R} = \begin{bmatrix} R_{\Sigma\Sigma} & R_{\Sigma\Delta} \\ R_{\Delta\Sigma} & R_{\Delta\Delta} \end{bmatrix} \quad (3.18)$$

The covariance matrix can be estimated with the formula given below:

$$\hat{\mathbf{R}}[l, m] = \frac{1}{2N} \sum_{\substack{a=-N-N_g \\ -Ng < a < Ng \text{ is not included}}}^{N+N_g} \mathbf{x}[a, m] \cdot \mathbf{x}^H[a, m] \quad (3.19)$$

Just like in adaptive DPCA, estimation is obtained from the nearby range cells with an amount of guard cells.

After calculating the estimate of interference covariance matrix, optimum filter weights can be found with the formula given below:

$$\tilde{\mathbf{h}} = \hat{\mathbf{R}}^{-1} \mathbf{t}^* \quad (3.20)$$

where  $\mathbf{t}$  is the target expected signal vector given by

$$\mathbf{t} = [s_1(0) \quad s_1(1) \quad \dots \quad s_1(N-1)] \quad (3.21)$$

The output vector  $\mathbf{z}$  will be:

$$\mathbf{z} = \mathbf{h}'_{opt} \mathbf{x} = \mathbf{t}^H (\tilde{\mathbf{R}}^{-1})^* \mathbf{x} \quad (3.22)$$

The whole process is shown in Figure – 3.13.

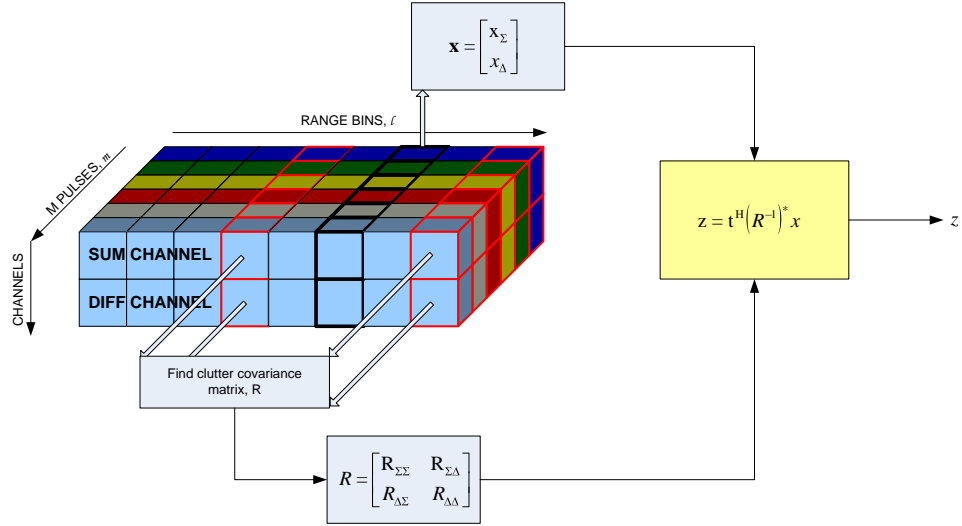


**Figure – 3.13:** Pre-Doppler  $\Sigma - \Delta$  STAP Processing Block Diagram

Second method is the Post-Doppler  $\Sigma - \Delta$  STAP [24]. In this method, adaptive cancellation weights are calculated for each Doppler bin individually after the Doppler processing.

Let us say that  $\mathbf{x}$  is the observation matrix

$$\mathbf{x} = \begin{bmatrix} \mathbf{x}_\Sigma \\ \mathbf{x}_\Delta \end{bmatrix} \quad (3.23)$$

where  $\mathbf{x}_\Sigma$  is the data vector measured and sampled from the sum channel and  $\mathbf{x}_\Delta$  is the data vector measured and sampled from the difference channel.  $H_1$  shows the case where target exists and  $H_2$  shows the case that there isn't any target signal.

$$H_1 : \mathbf{x} = \mathbf{c} + \mathbf{n} + \mathbf{b}s \quad (3.24)$$

$$H_2 : \mathbf{x} = \mathbf{c} + \mathbf{n}$$

The clutter covariance matrix can be estimated by using 3.18 and 3.19.  $\mathbf{D}$  matrix is used for the Fourier transformation and it is defined as

$$\mathbf{D} = \begin{bmatrix} \mathbf{F} & 0 & \dots & 0 \\ 0 & \dots & 0 & \mathbf{F} \end{bmatrix} \quad (3.25)$$

where

$$\mathbf{F} = [1 \quad e^{j\omega} \quad e^{j2\omega} \quad \dots \quad e^{j\omega(N-1)}]. \quad (3.26)$$

$\omega$  is the related Doppler velocity in radians used for the Fourier transformation.

After the clutter covariance matrix estimation, adaptive cancellation weights can be calculated by the formula given below:

$$\mathbf{w} = \gamma(\mathbf{D}\mathbf{R}\mathbf{D}')^{-1}\mathbf{D}\mathbf{b} \quad (3.27)$$

In this formula,  $\mathbf{b}$  represents the expected target signal in sum and delta channels and can be shown as given below:

$$\mathbf{b} = [s_1(0) \quad s_1(1) \quad \dots \quad s_1(N-1) \quad s_2(0) \quad s_2(1) \quad \dots \quad s_2(N-1)] \quad (3.28)$$

Here,  $s_i(n)$  can be defined as

$$s_i(n) = G_t G_r \exp(-j\omega n), \quad n = 1, 2, \dots \quad (3.29)$$

Where  $G_t$  is the transmit antenna pattern,  $G_r$  is the receive antenna pattern and  $\exp(-j\omega n)$  is the phase shift due to the round-trip delay time. This weight calculation has to be done for each Doppler bin. The adaptive cancellation weights can be represented simply in a convenient form given below:

$$\mathbf{w} = \begin{bmatrix} w_1 \\ w_2 \end{bmatrix} \quad (3.30)$$

The output vector  $z$  will be

$$z = wDx \quad (3.31)$$

The  $Dx$  process shown in (3.31) is used to find the Doppler bins of the sigma and delta channels.

The whole process is shown in Figure – 3.14.

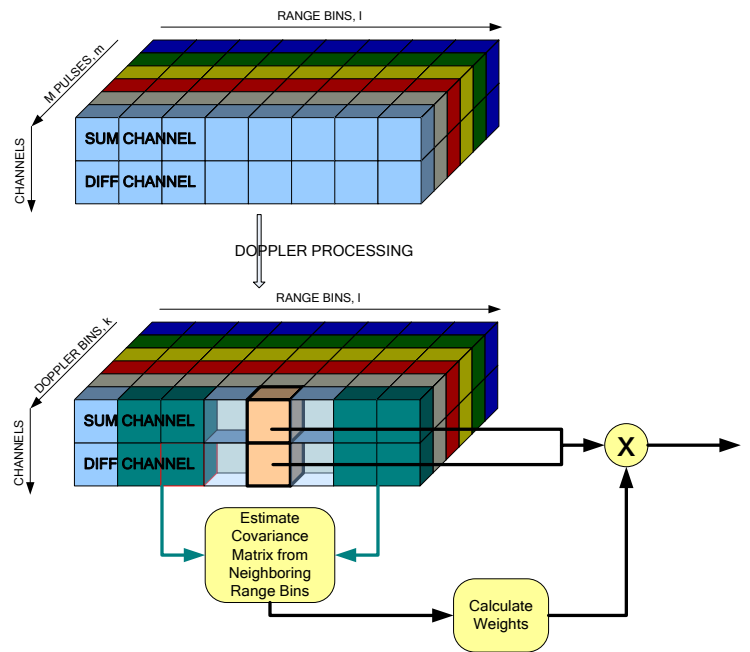


**Figure – 3.14:** Post-Doppler  $\Sigma - \Delta$  STAP Processing Block Diagram

Where the Pre-Doppler and Post-Doppler cases are compared, it is expected that they have the same performance results. The only difference between these methods is the estimation of the adaptive weights before or after the Fourier transformation.

Post-Doppler is a more privatized method. It estimates the cancellation weights after  $DRD'$  transformation. This transformation reduces the size of the clutter covariance matrix to a 2-by-2 matrix and the matrix inversion becomes easier. Because of this, Post-Doppler method has less processing load compared with Pre-Doppler method.

### 3.5. Detection Algorithm

DPCA, Adaptive DPCA, Pre-Doppler  $\Sigma - \Delta$  STAP and Post-Doppler  $\Sigma - \Delta$  STAP techniques are used to eliminate the unwanted clutter and maximize the SNR. After applying these techniques to the data observed during the operation, a range-Doppler matrix can be found. Some of these techniques (Adaptive DPCA and Post-Doppler  $\Sigma - \Delta$  ) already give a range-Doppler output and the others (DPCA and Pre-Doppler  $\Sigma - \Delta$  STAP) needs a Fourier transformation to be performed over all range bins to find the range-Doppler matrix.

After finding the range-Doppler matrices, conventional CFAR techniques can be applied to the data to find the moving targets.

A conventional detection rule cannot be applied to the ATI processor output, because ATI is not a clutter suppression technique. It uses the linear phase change of the target to distinguish it from the clutter and noise. As shown in Figure – 3.9, ATI processor output spreads over a magnitude vs. phase plane and the highly correlated signals like clutter centre at the zero phase angle point. The purpose here is to find the targets having a phase change greater than the maximum clutter phase angle.

There are some CFAR methods suggested to improve the detection performance in ATI [25]. The phase-magnitude plane of the ATI processor output is divided into three regions in these methods like clutter dominant region (Region I), noise dominant region (Region III) and the region where target detection can be performed (Region II) as shown in Figure – 3.15.

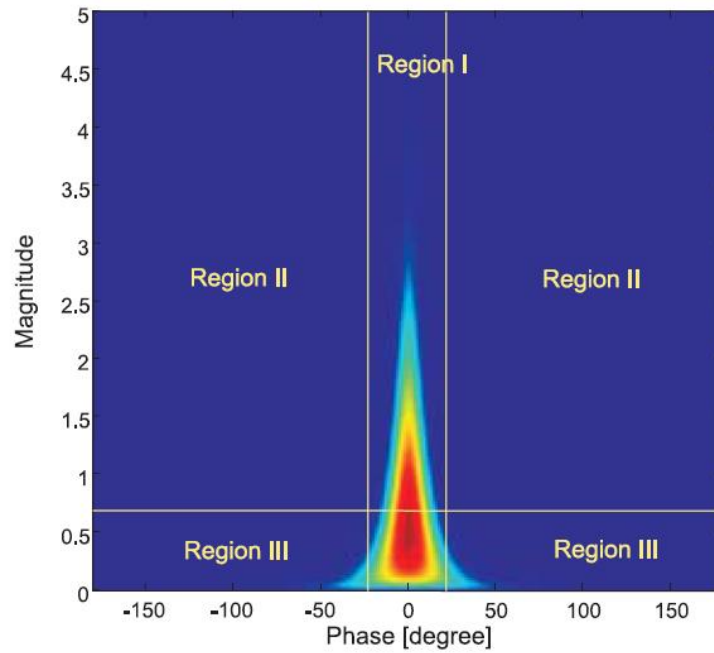


**Figure – 3.15:** Detection Regions for ATI Processor Output

In the simulator developed within the context of this thesis, a conventional Cell-Averaging CFAR detector is used for the techniques except ATI. A basic CFAR detector operating in range-phase plane is used in the simulator for ATI.

## **CHAPTER 4**

### **GMTI SIMULATOR**

#### **4.1. The Purpose of the Simulator**

The main purpose of the GMTI simulator is to compare the abilities of the basic GMTI techniques explained in Chapter 3 under controlled radar parameters and in different environments.

The radar and antenna parameters can be set and different clutter characteristics can be chosen in the simulation environment from the user interface of the simulator. The number of targets and its properties is also selectable from the interface.

In this Chapter, the operation principles of the simulator are explained and in Chapter 5, the comparison of the GMTI techniques explained in Chapter 3 is investigated.

#### **4.2. Basic Properties of the Simulator**

On the simulator interface, there are three main sections where radar, moving target and clutter parameters can be selected (Figure – 4.1).

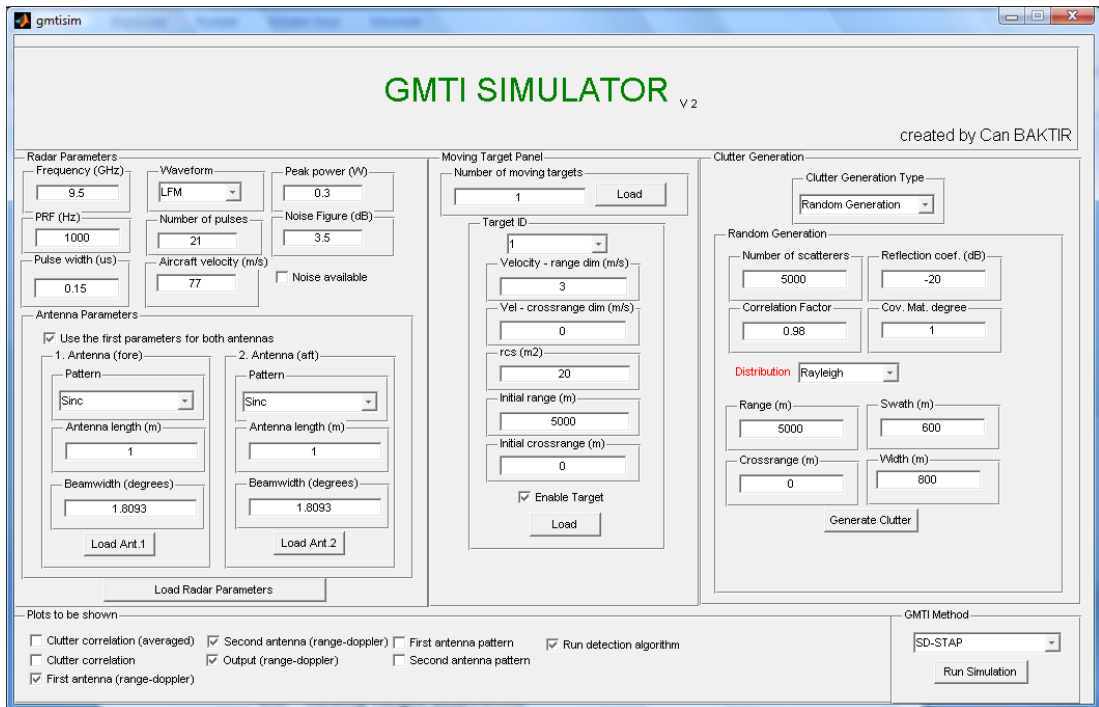


**Figure – 4.1:** GMTI Simulator Graphical User Interface

Basic radar parameters can be set from the “Radar Parameters” section (Figure – 4.2). In this simulator, the algorithms work for one pulse burst. A burst contains a sequence of identical pulses the number of which is determined by the “Number of Pulses” edit box. The operating frequency, PRF, the pulse length, the output power and the noise figure of the radar can be set from this section.

For the radar waveform, there are three available waveform alternatives which are LFM (Linear Frequency Modulation), Barker-13 and a long code developed for the simulation. The number of waveform alternatives can be increased according to the need by embedding the waveform into the simulator.

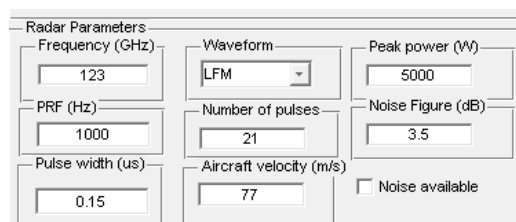


**Figure – 4.2:** Radar Parameters Selection Section

Another important property of the simulator is the ability of adding noise according to the radar parameters to the raw data while generating it. When the “Noise available” tab is selected, an additive white Gaussian noise (AWGN) is added to each pulse according to the radar parameters (Figure – 4.3).



**Figure – 4.3:** Noise Addition Checkbox

The part under the radar parameters selection section is the “Antenna Parameters” section (Figure – 4.4). The basic antenna parameters can be set in this part. According to the antenna pattern and the length of the antenna, gain is calculated automatically. These selections are available only for the azimuth pattern. The elevation pattern is a sinc pattern and it has a constant 20 degrees beamwidth. This value can be changed inside the code.

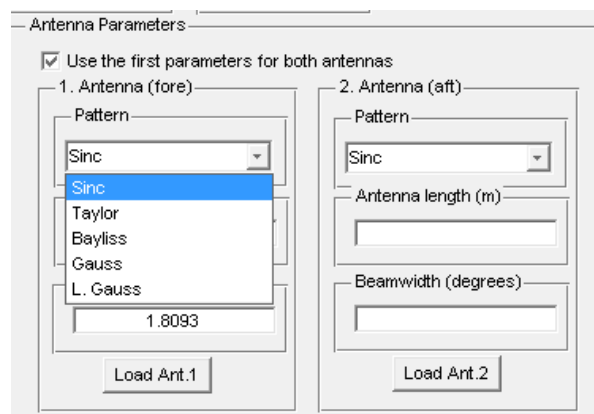


**Figure – 4.4:** Antenna Parameters Selection Section

The antenna patterns can be selected differently for the first (fore) antenna and the second (aft) antenna. The selection of the distance between the antennas is done according to the number of PRI’s (time slip pulses) from a pop-up menu when the simulation starts (Figure – 4.5).

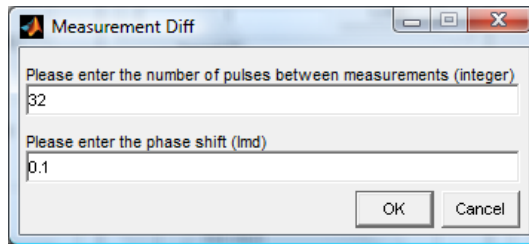


**Figure – 4.5:** Measurement Errors Pop-up Menu

If the tab shown in Figure – 4.6 is selected, all first antenna parameters are also valid for the second antenna whatever the selections in the second antenna tab are.



**Figure – 4.6:** Same Antenna Params Selection Checkbox

After the selections of radar parameters are finalized, these parameters can be entered to the simulation with button shown in Figure 4.7. Like the other parameter selection sections, radar parameters selection section is also independent from the other sections. Radar parameters can be changed from this section without making any change in the target or clutter parameters. This is good to see the effects of each part individually in the simulation.

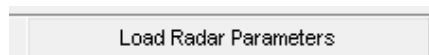


**Figure – 4.7:** Radar Parameters Loading Button

When "Load Radar Parameters" button is entered, some pop-up menus may appear according to the selections. If the LFM waveform is selected, the sweep bandwidth is asked (Figure – 4.8).



**Figure – 4.8:** Entering FM Bandwidth

If the Taylor pattern is selected from the antenna pattern section, the sidelobe level is asked. If different antenna parameters selection is made, the sidelobe level is asked for both antennas.

### 4.3. Clutter Generation

In the clutter generation part of the simulator, there are three clutter generation options that can be selected. These options are "Random Generation", "Importing from Image" and "Single Point Entry" (Figure – 4.9). The mostly used option is random clutter generation, because, in this option, the clutter parameters required for the GMTI techniques comparison can be entered.

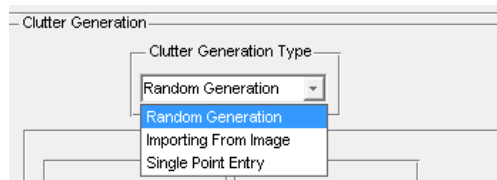


**Figure – 4.9:** Clutter Generation Type Selection

After the selection of random clutter generation from the simulator, the menu shown in Figure – 4.10 will come to the screen. In this section of the thesis, the random clutter generation method is explained.

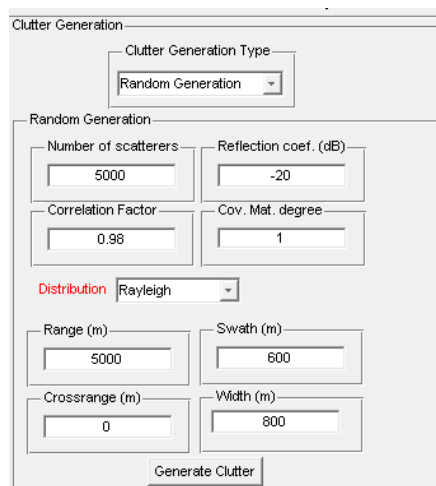


**Figure – 4.10:** Clutter Parameters Selection Section

As explained in Chapter 1, each clutter patch can be thought as a sum of point scatterers whose total radar cross section (RCS) can be calculated according to the range resolution, the azimuth beamwidth, the radar look angle, the squint angle and the reflectivity of the ground.

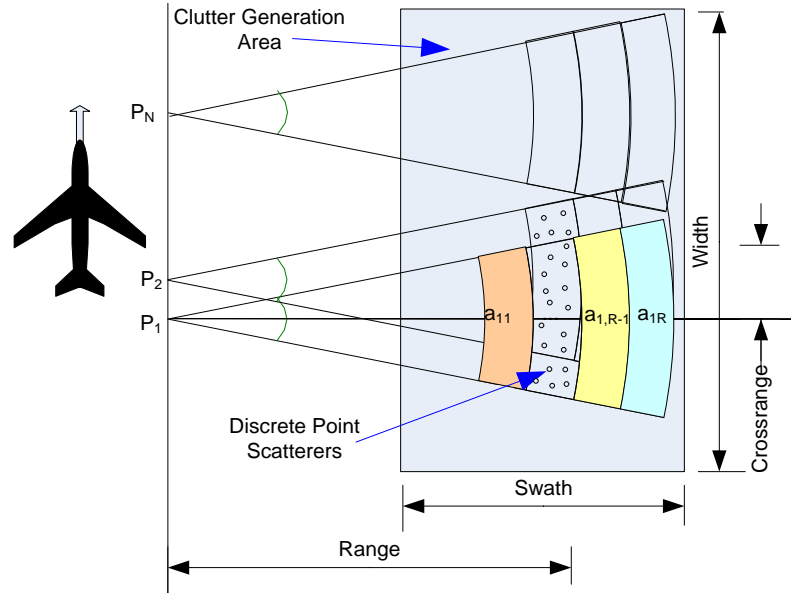


**Figure – 4.11:** Clutter Generation Geometry

The total number of the point scatterers can be selected from the clutter generation section of the simulator (Figure – 4.11). As the number of point scatterers entered from the clutter generation section, point scatterers are generated by the simulator. For each point scatterer, an X-Y coordinate is assigned according to the swath width, range and crossrange parameters of the clutter generation area.

$$\mathbf{x} = [x_1 \ x_2 \ x_3 \ \dots \ x_N], \quad Range - \frac{Swath}{2} < x_k < Range + \frac{Swath}{2} \quad (4.1)$$

$$\mathbf{y} = [y_1 \ y_2 \ y_3 \ \dots \ y_N], \quad (4.2)$$

$$Crossrange - \frac{Width}{2} < y_k < Crossrange + \frac{Width}{2}$$

where N is the number of point scatterers. The X-Y coordinates are uniformly distributed in the clutter generation area instead of generating them along

lines representing the range cells and the number of them are tried to be hold as many as possible to provide random phases to them.

In the simulation, all scatterers are thought as independent of each other and generated as complex samples.

$$a_{pq} = \alpha + j\beta \quad (4.3)$$

where  $\alpha$  and  $\beta$  are generated from a Gaussian distribution. Here,  $p$  represents the pulse number and  $q$  represents the scatterer number. Each pulse vector has all the complex scatterer coefficients.

$$P_p = [a_{p1} \quad a_{p2} \quad \dots \quad a_{pN}] \quad (4.4)$$

So the pulse-scatterer matrix becomes:

$$S = \begin{bmatrix} P_1 \\ P_2 \\ \vdots \\ P_{N_p} \end{bmatrix} = \begin{bmatrix} a_{11} & a_{12} & \dots & a_{1N} \\ a_{21} & a_{22} & \dots & a_{2N} \\ & & \vdots & \\ a_{N_p 1} & a_{N_p 2} & \dots & a_{N_p N} \end{bmatrix} \quad (4.5)$$

where  $N$  is the number of point scatterers and  $N_p$  is the number of pulses in a burst.

Firstly, all complex samples are generated independently in the "S" matrix.

The distribution of samples is described according to their envelope pdf's (probability density function). If a Rayleigh envelope pdf is wanted, marginal pdf's for  $\alpha$  and  $\beta$  has to be chosen from the Gaussian distribution.

As described in [2], if a random vector is SIRV (Spherically Invariant Random Vector), then there exists a nonnegative random variable  $Z$  such that the pdf of the random vector contained on  $Z$  is a multivariate Gaussian pdf.

$$Y = SZ \quad (4.6)$$

For the product given above,  $\mathbf{Y}$  denotes the SIRV,  $\mathbf{S}$  is a Gaussian random vector with zero mean and covariance matrix  $\mathbf{M}$  and  $Z$  is nonnegative random variable with pdf  $f_z(z)$ .

If K-distribution is wanted for the envelope pdf, the method given above is applied. A vector  $Z = [z_1 \ z_2 \ \dots \ z_N]$  has to be generated from the Gamma distribution and all  $P_p = [a_{p1} \ a_{p2} \ \dots \ a_{pN}]$  vectors are multiplied with this  $Z$  vector.

$$\mathbf{Y} = \begin{bmatrix} P_1 \\ P_2 \\ \vdots \\ P_{N_p} \end{bmatrix} \cdot \begin{bmatrix} Z \\ Z \\ \vdots \\ Z \end{bmatrix} = \begin{bmatrix} a_{11} & a_{12} & \dots & a_{1N} \\ a_{21} & a_{22} & \dots & a_{2N} \\ \vdots & \vdots & \ddots & \vdots \\ a_{N_p 1} & a_{N_p 2} & \dots & a_{N_p N} \end{bmatrix} \cdot \begin{bmatrix} z_1 & z_2 & \dots & z_N \\ z_1 & z_2 & \dots & z_N \\ \vdots & \vdots & \ddots & \vdots \\ z_1 & z_2 & \dots & z_N \end{bmatrix} \quad (4.7)$$

$$\mathbf{Y} = \begin{bmatrix} z_1 a_{11} & z_2 a_{12} & \dots & z_N a_{1N} \\ z_1 a_{21} & z_2 a_{22} & \dots & z_N a_{2N} \\ \vdots & \vdots & \ddots & \vdots \\ z_1 a_{N_p 1} & z_2 a_{N_p 2} & \dots & z_N a_{N_p N} \end{bmatrix} \quad (4.8)$$

So, the samples at each pulse will have K-distributed envelope pdf.

But, the samples in same range bin at each pulse are different and randomly distributed. This means that there is no correlation between values of a scatterer at each pulse.

If  $\mathbf{Y}$  is a SIRV with characteristic pdf  $f_y(y)$ , then

$$\mathbf{X} = \mathbf{A}\mathbf{Y} + \mathbf{b} \quad (4.9)$$

is also a SIRV with the same characteristic pdf. It is assumed that  $\mathbf{A}\mathbf{A}^H = \Sigma$  and  $\mathbf{b}$  is a known vector having same dimension as  $\mathbf{Y}$ .

The theorem [2] provides a powerful technique for simulating SIRVs. A white SIRV is defined as one that has a diagonal covariance matrix. In other words, the components of SIRV are uncorrelated but not necessarily independent.

We can start with a zero-mean white SIRV  $\mathbf{Y}$  having identity covariance matrix and perform the linear transformation given above to obtain a SIRV  $\mathbf{X}$  having a non-zero mean and desired covariance matrix  $\Sigma$ . The matrix  $\mathbf{A}$  and vector  $\mathbf{b}$  are given by

$$\mathbf{A} = \mathbf{E}\mathbf{D}^{1/2} \quad (4.10)$$

$$\mathbf{b} = \mu_x \quad (4.11)$$

where  $\mathbf{E}$  is the matrix of normalized eigenvectors of the desired covariance matrix  $\Sigma$ ,  $\mathbf{D}$  is the diagonal matrix of eigenvalues of  $\Sigma$  and  $\mu_x$  is the desired mean vector.

The desired mean is generally zero. But to find  $\mathbf{E}$  and  $\mathbf{D}$ , a desired covariance matrix has to be generated initially.

In exactly side looking radars, the correlation mainly depends on the internal clutter motion. Because, the reflectivity change due to the platform motion is very low. As described above, each clutter patch can be thought of as a sum of point scatterers and there is a very small change between the patches seen by pulses at the same range bin due to the platform motion.

So, the clutter covariance matrix can be generated according to a given correlation factor and its degree.

$$\Sigma = \begin{bmatrix} 1 & \rho^{N_p} & \rho^{2N_p} & \dots & \rho^{(N-1)N_p} \\ \rho^{N_p} & 1 & \rho^{N_p} & \dots & \rho^{(N-2)N_p} \\ \rho^{2N_p} & \rho^{N_p} & 1 & \dots & \dots \\ \vdots & \vdots & \vdots & \ddots & \vdots \\ \vdots & \vdots & \vdots & \vdots & \vdots \\ \rho^{(N-1)N_p} & \rho^{(N-2)N_p} & \rho^{(N-3)N_p} & \dots & 1 \end{bmatrix} \quad (4.12)$$

where  $\rho$  is the correlation coefficient and  $N_p$  is the degree of the clutter covariance matrix.

After generating this matrix,  $\mathbf{E}$  and  $\mathbf{D}$  can be calculated and  $\mathbf{A}$  can be generated. By using  $\mathbf{X} = \mathbf{A}\mathbf{Y} + \mathbf{b}$ , the sample matrix having desired covariance matrix and characteristic pdf is generated.

Each row of  $\mathbf{X}$  shows the values of the point scatterers at each pulse.

$$\mathbf{X} = \begin{bmatrix} x_{11} & x_{12} & \dots & x_{1N} \\ x_{21} & x_{22} & \dots & x_{2N} \\ \vdots & \vdots & \ddots & \vdots \\ x_{N_p 1} & x_{N_p 2} & \dots & x_{N_p N} \end{bmatrix} \quad (4.13)$$

If correlation coefficient  $\rho$  is 1 (or very close to 1), all samples at each column of  $\mathbf{X}$  is same.

$$x_{1k} = x_{2k} = \dots = x_{N_p k} \quad (4.14)$$

This means that there is no internal clutter motion and a scatterer has the same complex value at each pulse.

The reflectivity of the ground is added to the simulation after the generation of pulse-scatterer matrix. Each pulse vector is zero-mean in the pulse-scatterer matrix. According to the reflection coefficient and the resolution cell area at each range bin, a reflectivity matrix is generated (Figure – 4.12). This reflectivity matrix shows the resolution cell area of each range bin and can be calculated by using the equation 2.5.

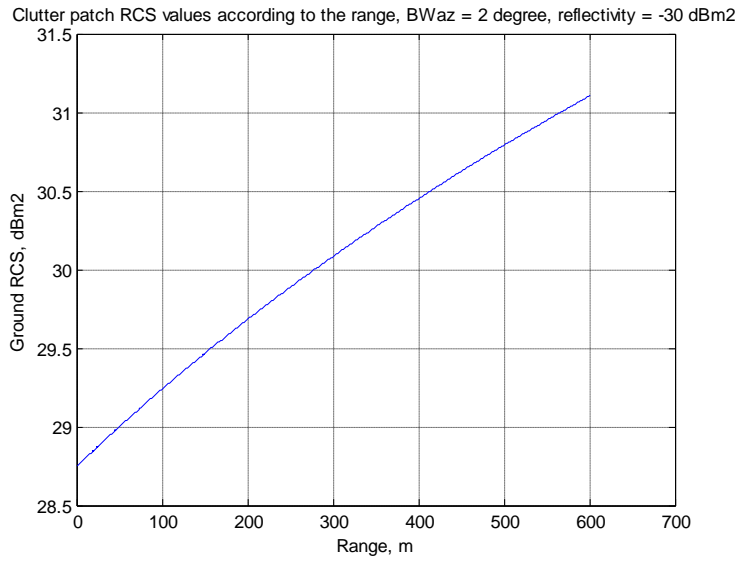


**Figure – 4.12:** Ground RCS Values According to the Range

In the generation of raw GMTI data, a received power vector is generated for each pulse by using the range-scatterer and the reflectivity matrices (Figure – 4.13).

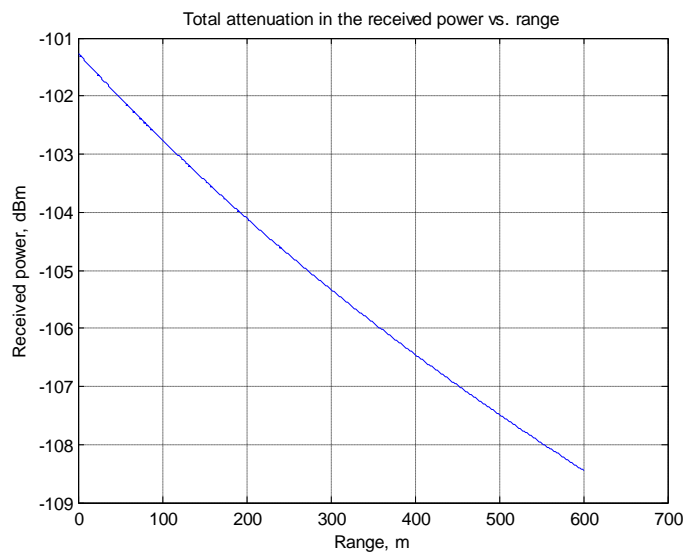


**Figure – 4.13:** Reflectivity Matrix

In the foregoing, only the generation of reflectivity coefficients of scatterers was explained.

In the generation of raw GMTI data, the formula given below is used:

$$s(t, u) = \sum_n \sigma_n p \left[ t - \frac{2\sqrt{x_n^2 + (y_n - u)^2}}{c} \right] \quad (4.15)$$

where

$$\frac{2\sqrt{x_n^2 + (y_n - u)^2}}{c} \quad (4.16)$$

is the round-trip delay from the radar to the  $n^{\text{th}}$  target. The  $s(t, u)$  matrix is a two dimensional matrix.  $t$  shows the fast-time axis and  $u$  shows the slow-time axis. Actually,  $u$  shows the flight positions of the aircraft at each pulse transmission.

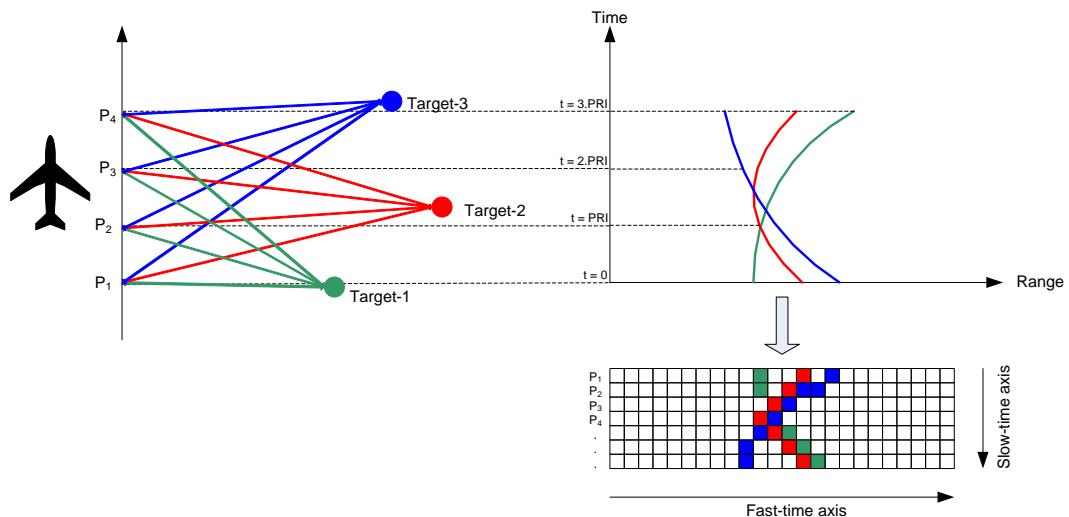


**Figure – 4.14:** Raw Clutter Data Generation Block Diagram

At each pulse transmission, the range between the radar and the  $n^{\text{th}}$  target changes (Figure – 4.14). For each pulse, the ranges between the radar and the targets are calculated and the transmitted signal is delayed and summed according to each round-trip delay time (Figure – 4.15).



**Figure – 4.15:** Targets Located in Different Range Bins in a Pulse

The radar cross section of each range bin in each pulse can be thought as the summation of point scatterers. If there are K point scatterers in the related range bin, the complex clutter sample can be defined as:

$$a_{xy} = \sum_{k=1}^K \alpha_{kxy} + j\beta_{kxy} \quad (4.17)$$

Before the summation, each delayed pulse is multiplied with the reflectivity matrix derived from the pulse-scatterer matrix  $\mathbf{X}$ . If correlation coefficient  $\rho$  is 1 (or very close to 1), the reflectivity of  $n^{\text{th}}$  scatterer doesn't change from pulse to pulse.

In the raw data generation, the effect of antenna pattern is also considered in the simulation. At each pulse, the angles of all scatterers are calculated and each scatterer is multiplied with the related pattern response at that position of the aircraft.

#### **4.4. Moving Target Generation**

In the moving target generation part, any desired number of moving targets can be added to the simulation. This section is independent from the other sections and the number and properties of targets can be changed without changing any of the radar or clutter parameters. This gives the advantage of observing the effects of different target parameters on the GMTI techniques.

The moving target generation section of the simulator is shown in Figure – 4.16. If the number of targets is selected and loaded, all target numbers can be seen in the target ID menu.

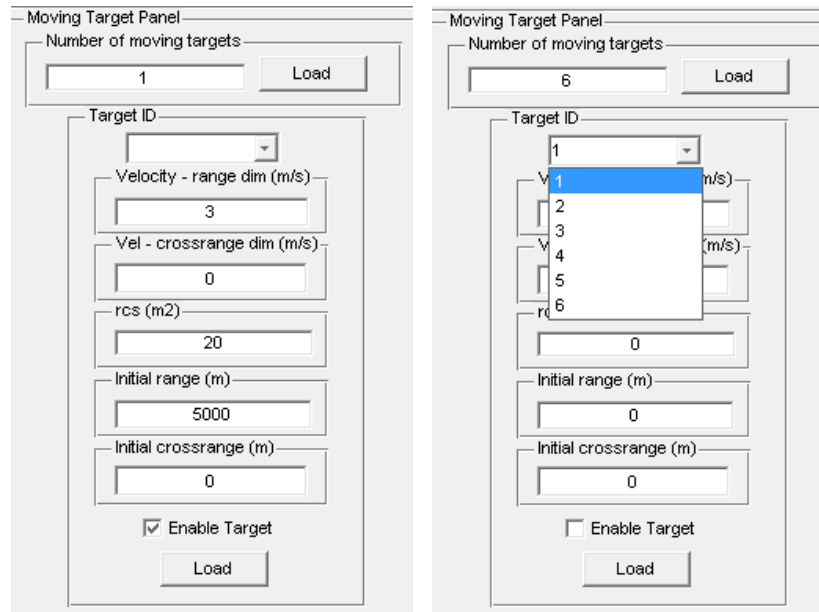


**Figure – 4.16:** Moving Target Parameters Selection Section

For each target, the velocity in range direction, the velocity in cross-range direction, the radar cross section and the initial X and Y coordinates of the target can be set. If the “Enable Target” checkbox of a target is not selected, the parameters of that target are kept saved but the echo of that target will not be added to the output.

Targets can be generated inside or outside of the clutter generation area. But if a target is generated outside of the clutter generation area, its effect cannot be seen at the simulation output, because the simulation output is calculated only over the clutter generation area (Figure – 4.17).

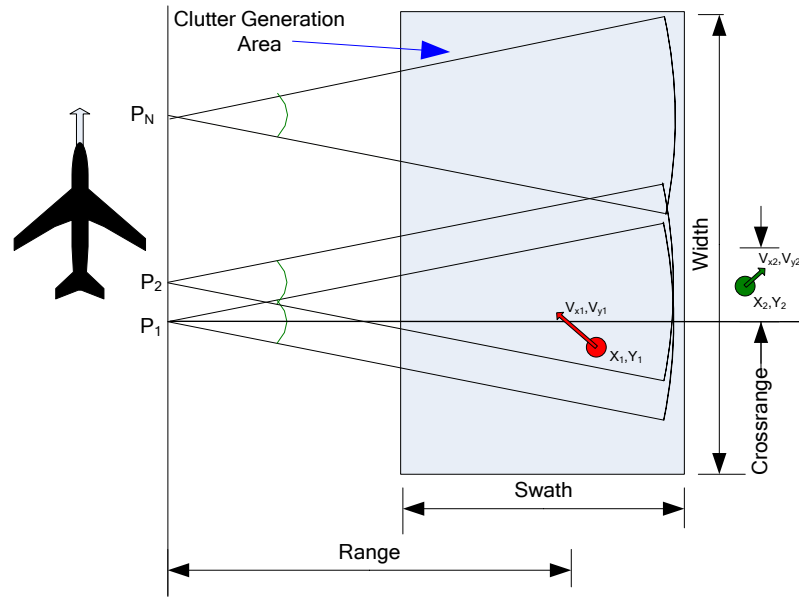


**Figure – 4.17:** Moving Target Generation Geometry

According to the initial coordinates and the velocities in range and cross-range dimensions of the target, the range and the position of the targets are changed over the pulses of the burst. The coordinate vectors  $\mathbf{x}$  and  $\mathbf{y}$  remain fixed from pulse to pulse for a stationary target. But these vectors must be matrices showing the coordinates of each target at each pulse and these are calculated automatically in the simulation according to the target velocity components.

$$\mathbf{x} = [x_1 \ x_2 \ x_3 \ \dots \ x_N] \quad (4.18)$$

$$\mathbf{y} = [y_1 \ y_2 \ y_3 \ \dots \ y_N] \quad (4.19)$$

where N shows the target ID.

The "S" matrix having the reflectivity coefficients of each target at each pulse has to be generated for the simulation.

$$S = \begin{bmatrix} P_{T1} \\ P_{T2} \\ \vdots \\ P_{TN_p} \end{bmatrix} = \begin{bmatrix} \sigma_{11} & \sigma_{12} & \dots & \sigma_{1N} \\ \sigma_{21} & \sigma_{22} & \dots & \sigma_{2N} \\ & & \vdots & \\ \sigma_{N_p 1} & \sigma_{N_p 2} & \dots & \sigma_{N_p N} \end{bmatrix}, \quad P_{TX} = [\sigma_{X1} \quad \sigma_{X2} \quad \dots \quad \sigma_{XN}] \quad (4.20)$$

In the simulation, all targets are assumed to have a Swerling-0 characteristic. So, the reflectivity coefficients of each target do not change from pulse to pulse. So, the "S" matrix will be as shown below.

$$S = \begin{bmatrix} P_{T1} \\ P_{T2} \\ \vdots \\ P_{TN_p} \end{bmatrix} = \begin{bmatrix} \sigma_1 & \sigma_2 & \dots & \sigma_N \\ \sigma_1 & \sigma_2 & \dots & \sigma_N \\ & & \vdots & \\ \sigma_1 & \sigma_2 & \dots & \sigma_N \end{bmatrix} \quad (4.21)$$

In the generation of raw GMTI data for targets, the same formula given in Section 4.3 is used. The only difference is the change in the coordinate vectors.

#### 4.5. Applying GMTI Techniques

To evaluate the performances of the GMTI techniques explained in previous chapters, firstly, the raw GMTI data has to be generated including clutter, target and noise signals for both antennas or for both channels.

According to the radar, clutter and target parameters, simulator generates three data matrices for both antennas.

One of them is the clutter data matrix  $s(t, u)$ . One axis of this matrix is the slow time axis showing the pulses and the other axis is the fast time axis showing the range bins in each pulse.

Another matrix that is generated is the target data matrix. This matrix is generated according to the targets in the clutter generation area and their parameters.

The last matrix generated is the matrix having noise. These three matrixes are summed and a GMTI data matrix for one antenna or channel is generated. Figure – 4.18 shows the data generation steps.

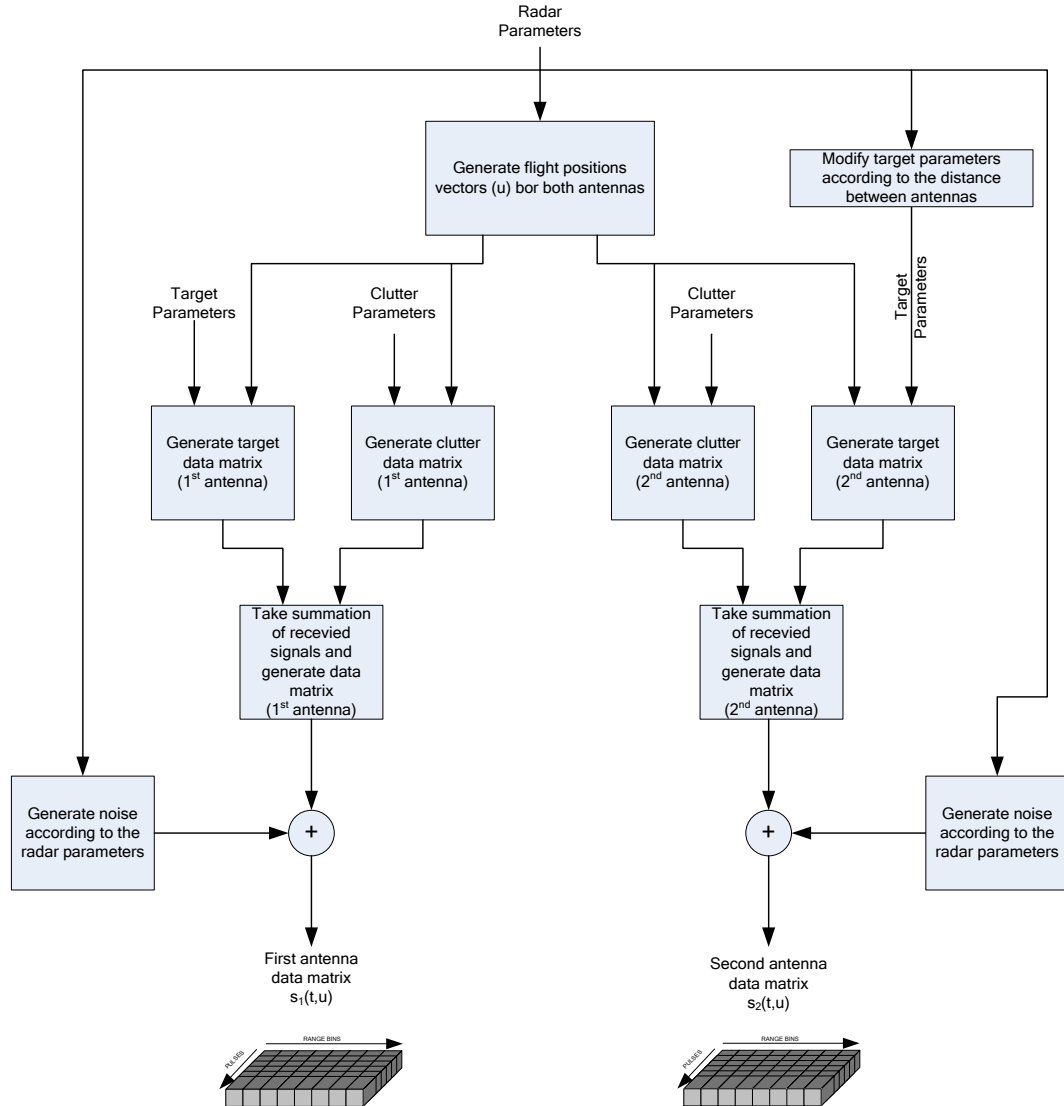


**Figure – 4.18:** Raw GMTI Data Generation Block Diagram

After the generation of  $s_1(t, u)$  and  $s_2(t, u)$  matrices, any one of the GMTI techniques explained in Chapter-3 can be applied to the raw data.

## **CHAPTER 5**

### **SIMULATION RESULTS**

#### **5.1. DPCA**

DPCA is a basic clutter suppression technique used in airborne radars. Because of this, firstly, the clutter suppression capability of DPCA is going to be investigated.

As mentioned in Section 2.2, DPCA is the oldest, simplest and mostly used GMTI technique. Its clutter cancellation performance mostly depends on the phase center alignment mismatches and the internal clutter motion (ICM). The parameters given in Table 5 – 1 defines a scenario where there isn't any phase center mismatch between fore and aft antennas, no internal clutter motion (ICM) and the phase matching between channels are successfully adjusted (Figure – 5.1).

**Table 5 – 1:** Simulation Parameters for Figure – 5.1

<b>Radar Parameters:</b>		<b>Target Parameters:</b>	
Frequency:	9.5 GHz	Vel. (range):	3 m/s
Waveform:	LFM	Vel. (c-range):	0 m/s
Peak Power:	5000 W	RCS:	0 m <sup>2</sup>
PRF:	1000 Hz	Init range:	30100 m
Pulses:	21	Init c-range:	0 m
Noise Figure:	3.5 dB	<b>Clutter Parameters:</b>	
Pulse width:	0.15 $\mu$ s	# of scatterers:	15000
Velocity:	77 m/s	Reflection coefficient:	-20 dB/ m <sup>2</sup>
1. Antenna pat:	Sinc	Correlation factor:	1
1. Antenna BW:	1.8 degree	Covariance Mat. Deg:	1
2. Antenna pat:	Sinc	Distribution:	Rayleigh
2. Antenna BW:	1.8 degree	Range:	30000 m
		Cross-range:	0 m
		Swath:	4000 m
		Width:	5000 m

If the simulation is started with the parameters given in Table 5 – 1, the number of time slip pulses explained in Section 3.1 and the phase center misalignment distance in the flight direction is asked by the simulator. For this simulation, the time slip pulses are 32 and the phase center misalignment distance is 0 lambdas.

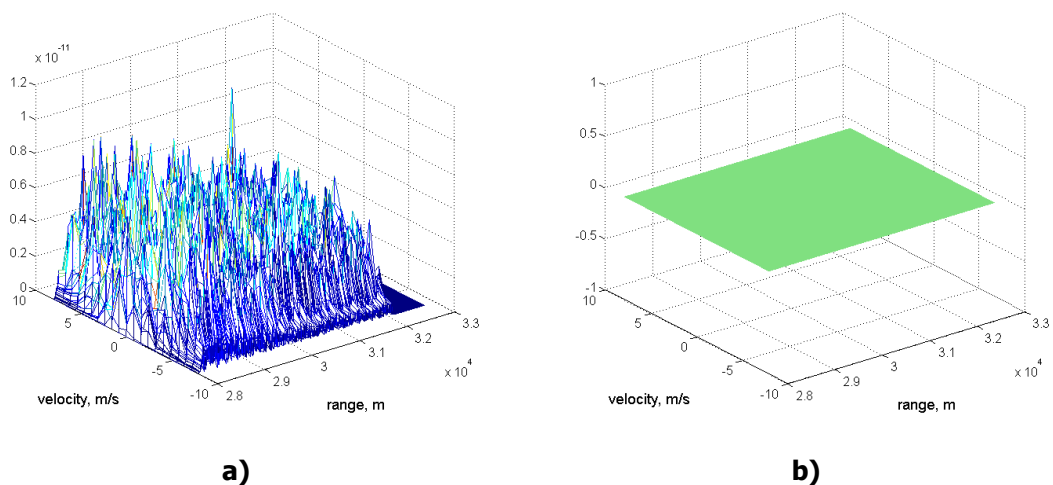


**Figure – 5.1:** a) Range-Doppler Output of First Channel b) Range-Doppler DPCA Output for Perfectly Aligned Antenna Case

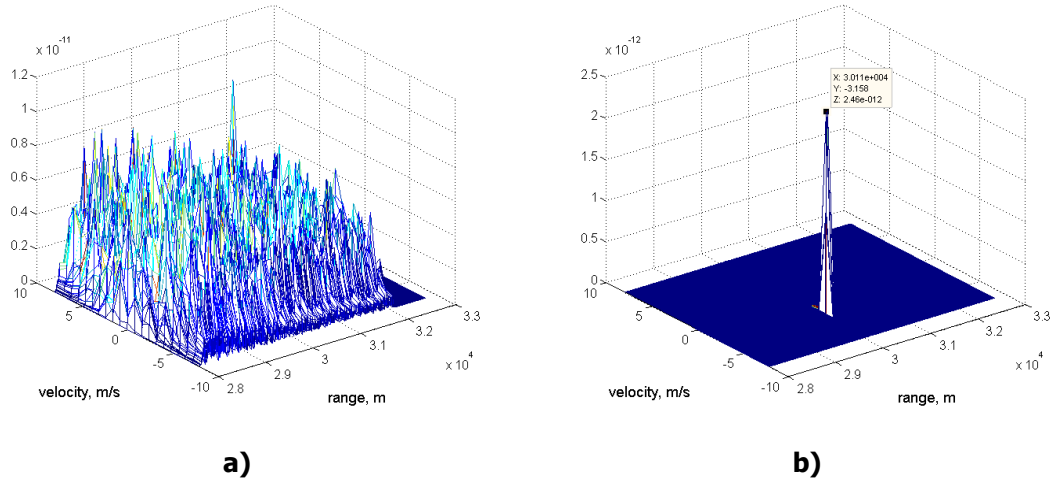
Figure – 5.1 – b shows the DPCA processor output for a scenario in which there is no target and noise signal at the fore and aft antenna channels and the phase center adjustment has been made successfully. The result is perfect clutter suppression by using DPCA.

Table 5 – 2 shows the simulation parameters of a DPCA processing being performed for a scenario in which there is a single moving target having 3 m<sup>2</sup> radar cross section (RCS) and no phase center misalignment between fore and aft antennas.

**Table 5 – 2:** Simulation Parameters for Figure – 5.2

<b><u>Radar Parameters:</u></b>		<b><u>Target Parameters:</u></b>	
Frequency:	9.5 GHz	Vel. (range):	3 m/s
Waveform:	LFM	Vel. (c-range):	0 m/s
Peak Power:	5000 W	RCS:	3 m <sup>2</sup>
PRF:	1000 Hz	Init range:	30100 m
Pulses:	21	Init c-range:	0 m
Noise Figure:	3.5 dB	<b><u>Clutter Parameters:</u></b>	
Pulse width:	0.15 μs	# of scatterers:	15000
Velocity:	77 m/s	Reflection coefficient:	-20 dB/ m <sup>2</sup>
3. Antenna pat:	Sinc	Correlation factor:	1
3. Antenna BW:	1.8 degree	Covariance Mat. Deg:	1
4. Antenna pat:	Sinc	Distribution:	Rayleigh
4. Antenna BW:	1.8 degree	Range:	30000 m
		Cross-range:	0 m
		Swath:	4000 m
		Width:	5000 m

For this simulation also, the time slip pulses are 32 and the phase center misalignment distance is 0 lambdas. This simulation is also performed for a scenario in which there is no ICM.



**Figure – 5.2:** a) Range-Doppler Output of First Channel b) Range-Doppler DPCA Output for Perfectly Aligned Antenna Case (target exists)

It can be seen that the clutter is eliminated and the target can be found perfectly at the output of the DPCA processor. The velocity of the target is found as 3.158 m/s. The small difference between the measured and actual target velocities are caused by the length of the FFT. As the length of the FFT increases, a more precise measurement can be achieved.

Figure – 5.3 shows the relationship between the clutter attenuation level and the normalized frequency. This figure is given for a scenario in which there is no phase center misalignment and no ICM. As compared with the performance of conventional two-pulse canceller MTI radar, this figure tells us that DPCA processing in the case of no ICM and no phase center misalignment gives a similar result. For targets or point scatterers having a Doppler shift of  $PRF/2$ , there is no signal attenuation due to the DPCA processing. But if the scatterer is located at squinted angles, the clutter attenuation performance degrades.

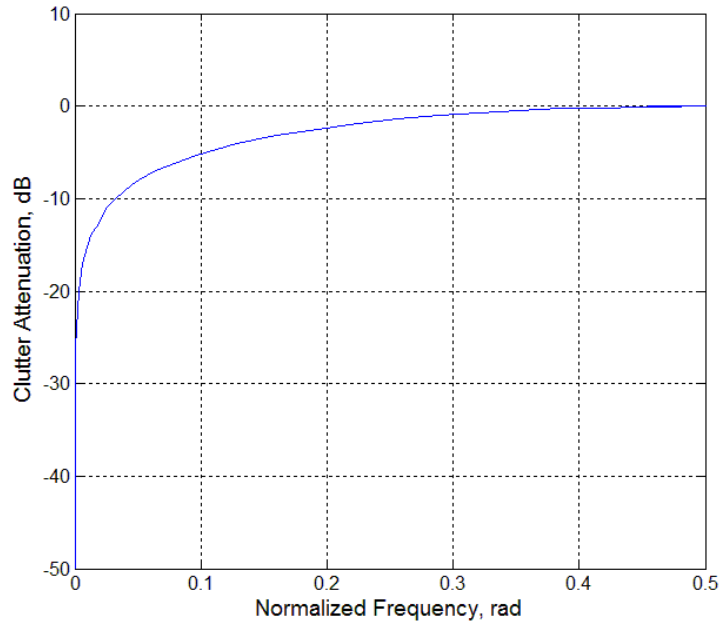


**Figure – 5.3:** Clutter Attenuation vs. Normalized Frequency for DPCA

If there is a misalignment at the phase centers between fore and aft antenna after the time slip pulses, the clutter cannot be suppressed successfully.

If the simulation is started with the parameters given in Table 5 – 2 where the number of time slip pulses is 32 and phase center misalignment in the flight direction is 0.1 lambdas, it can be seen that the clutter suppression performance of DPCA degrades (Figure – 5.4).

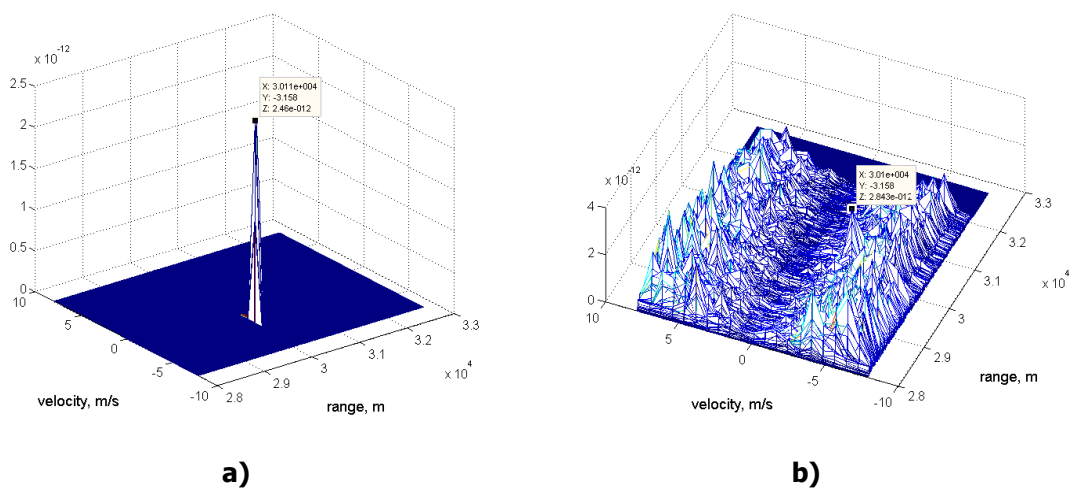


**Figure – 5.4:** Range-Doppler DPCA Output for a) Perfectly Aligned Antenna Case b) Phase Center Misaligned Case (target exist)

The clutter cancellation performance is better for low Doppler frequency region as seen in Figure – 5.3. This means that the clutter suppression performance is worse for the targets located at the squinted angles according to the radar beam than the ones located at the center of radar beam.

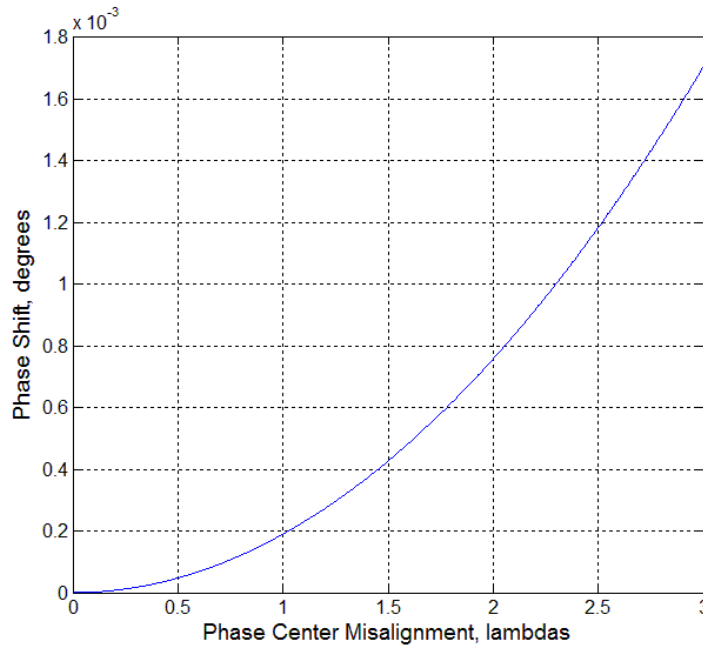


**Figure – 5.5:** Phase Shift in the Received Signal according to the Phase Center Misalignment for a Target Located at the Center of Radar Beam

As shown in Figure – 3.3, a phase center misalignment causes a phase shift in the received scatterer signal. This phase shift makes it difficult to suppress the unwanted clutter signals. Figure – 5.5 shows the phase shift values according to the phase center misalignment distances for a scatterer located at the center of the radar beam where the phase shift values are very low. So, the clutter cancellation performance is not affected so much for scatterers located at the regions close to the radar beam where these scatterers have small Doppler shifts according to the radar.

Figure – 5.6 shows the phase shift values according to the phase center misalignment distances for a scatterer located one degree squinted from the center of the radar beam. This scatterer has a higher Doppler shift than the

scatterer located at the center of the beam. For the scatterers located at squinted angles according to the radar beam, the phase shift due to the phase center misalignment is high. This makes it very difficult to suppress the unwanted clutter signal for scatterers located at squinted angles which have higher Doppler shifts according to the ones located at the center of the beam.

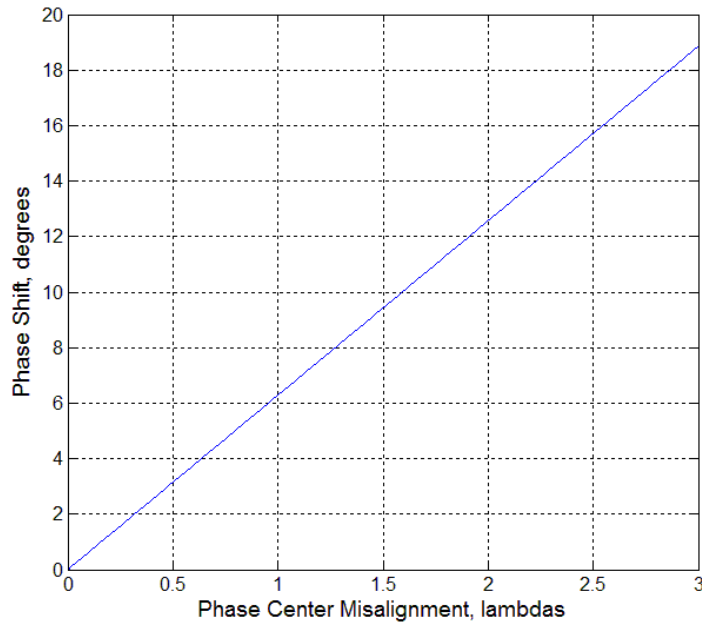


**Figure – 5.6:** Phase Shift in the Received Signal according to the Phase Center Misalignment for a Target Located 1 Degree Squinted from the Center of Radar Beam

At low Doppler frequencies, the clutter attenuation performance is better as explained in previous paragraphs. If there would be only one clutter sample at the center of the antenna beam, the phase changes caused by the antenna misalignments wouldn't affect the DPCA performance. But in the real life, this is not valid. There are infinite numbers of clutter samples around the antenna.

As it can be seen from Figure – 5.5, the real phase shift caused by the antenna misalignment for the scatterer located at the boresight is not high. So the DPCA processing can work successfully. But, as can be seen from Figure – 5.6, the actual phase shift caused by the antenna misalignment for

the scatterer located at 1 degree squinted from the boresight is high. The accumulated phase error of all squinted scatterers becomes so high to obstruct a successful DPCA cancellation.

Because of this, the higher is the antenna beamwidth; the higher is the accumulated phase error caused by the antenna misalignments.

In Figure – 5.7, the mean clutter attenuation in dB scale versus phase center misalignment in  $\lambda$  scale is shown. To find this plot, a Monte Carlo simulation is performed by using some parts of the simulator. The ratio between the mean power levels at the output of the first channel and at the output of DPCA processor is calculated according to the phase center misalignment distances in the flight direction.

As can be seen from Figure – 5.7, the clutter attenuation (CA) ratio is decreasing with the increasing value of the phase center misalignment. This phase center misalignment can be thought of as the summation of the phase adjustment errors in the channels and the phase error caused by the phase center misalignments.

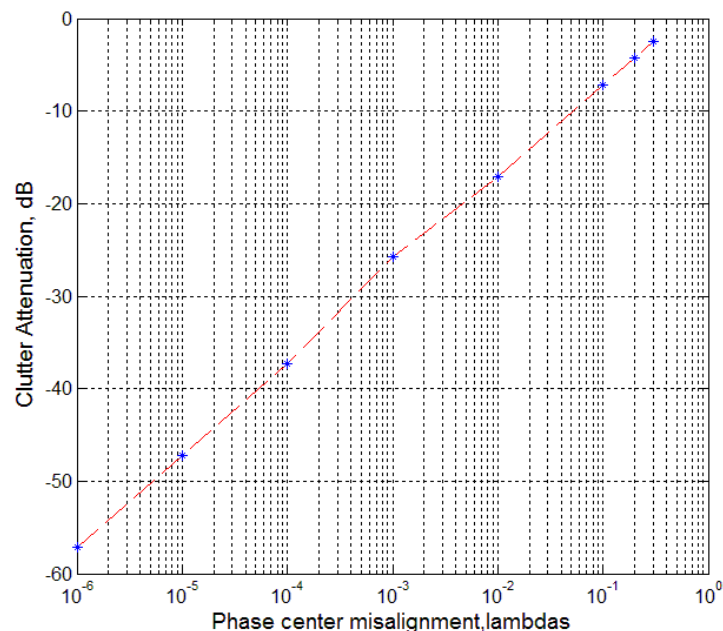


**Figure – 5.7:** Clutter Attenuation vs. Phase Center Misalignment

If the fore and aft antennas take measurements at the same position, i.e. there isn't any phase center misalignment, the clutter in the first antenna measurement can be exactly eliminated by using the second antenna measurements.

But the clutter attenuation is not only changing with phase center misalignments. It also depends on the frequency as shown in Figure – 5.3.

In Section 3.1, it is explained that the ICM is one of the most important factors affecting the clutter cancellation performance of DPCA. If the decorrelation of a point scatterer between two consecutive pulses is high, DPCA cannot eliminate the clutter exactly. The simulation parameters are given in Table 5 – 3 to see the DPCA performance for a scenario in which the ICM exists. The clutter correlation factor is used to generate the expected clutter covariance matrix for a scenario in which the ICM exists in 4.12.

**Table 5 – 3:** Simulation Parameters for Figure – 5.8

<b><u>Radar Parameters:</u></b>		<b><u>Target Parameters:</u></b>	
Frequency:	9.5 GHz	Vel. (range):	3 m/s
Waveform:	LFM	Vel. (c-range):	0 m/s
Peak Power:	5000 W	RCS:	6 m <sup>2</sup>
PRF:	1000 Hz	Init range:	30100 m
Pulses:	21	Init c-range:	0 m
Noise Figure:	3.5 dB	<b><u>Clutter Parameters:</u></b>	
Pulse width:	0.15 μs	# of scatterers:	15000
Velocity:	77 m/s	Reflection coefficient:	-30 dB/ m <sup>2</sup>
5. Antenna pat:	Sinc	Correlation factor:	0.9999
5. Antenna BW:	1.8 degree	Covariance Mat. Deg:	1
6. Antenna pat:	Sinc	Distribution:	Rayleigh
6. Antenna BW:	1.8 degree	Range:	30000 m
		Cross-range:	0 m
		Swath:	4000 m
		Width:	5000 m

As it can be seen from Figure – 5.8, in a scenario in which ICM exists, the clutter cancellation performance of DPCA degrades. Adaptive DPCA processing is a solution for this problem. In Figure – 5.17, the adaptive DPCA processor output for the same simulation parameters is shown.

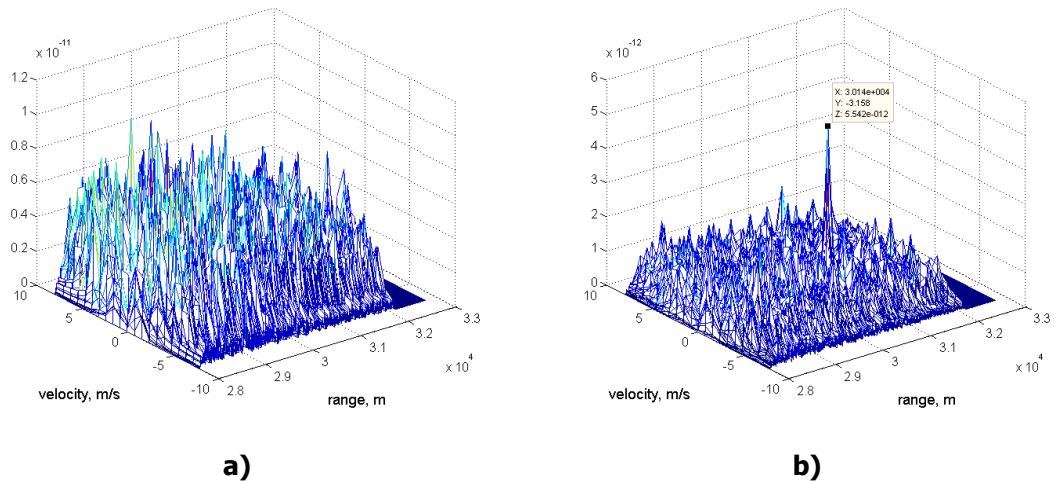


**Figure – 5.8:** a) Range-Doppler Output of First Channel b) Range-Doppler DPCA Output for Perfectly Aligned Antenna Case (ICM and target exist)

If the clutter correlation is high, i.e. the reflection coefficient of a point scatterer doesn't change so much between pulses, the clutter attenuation performance of DPCA will be successful. Figure – 5.9 shows the autocorrelation of clutter samples in each pulse. If the clutter correlation is high (e.g. correlation factor is 1), the autocorrelation output will have a flat like shape. But if the clutter correlation is low (e.g. correlation factor is 0.6), the autocorrelation output starts to have an impulse like shape, because the reflection coefficients of clutter samples change from pulse to pulse.

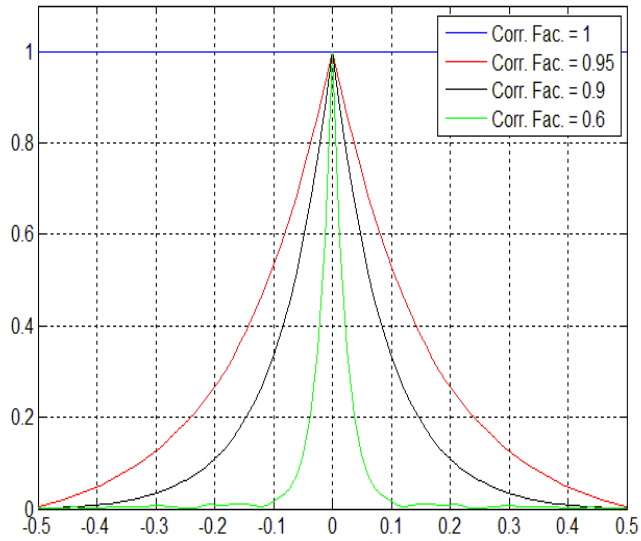


**Figure – 5.9:** Average Correlation of Clutter Samples according to the Correlation Factor  
 As the clutter correlation factor is decreased in the simulator, the clutter attenuation performance degrades. The reason of this situation is the changing reflection coefficient of the scatterers between pulses and between measurement taken by fore and aft antennas.

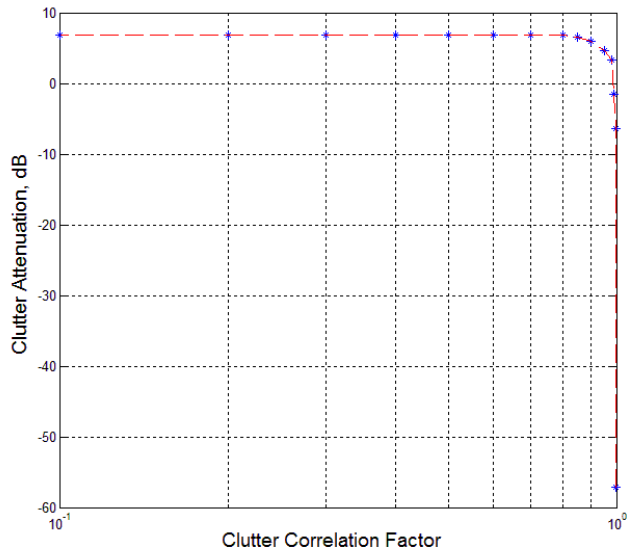


**Figure – 5.10:** Clutter Attenuation vs. Clutter Correlation Factor

Figure – 5.10 shows the clutter attenuation performance of DPCA as a function of the clutter correlation factor given in dB scale. For this simulation,

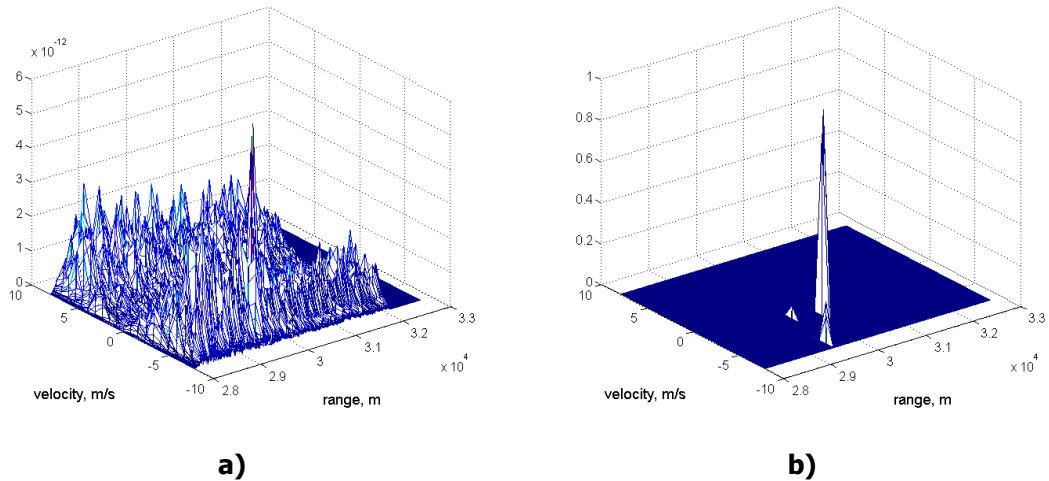
the time slip pulses are 32, the phase center misalignment distance is  $1e-6$  lambdas and there is no target added to the simulation.

A conventional Cell-Averaging CFAR algorithm is applied to the DPCA processor output to detect the targets. The simulation parameters are given in Table 5 – 4.

**Table 5 – 4:** Simulation Parameters for Figure – 5.8

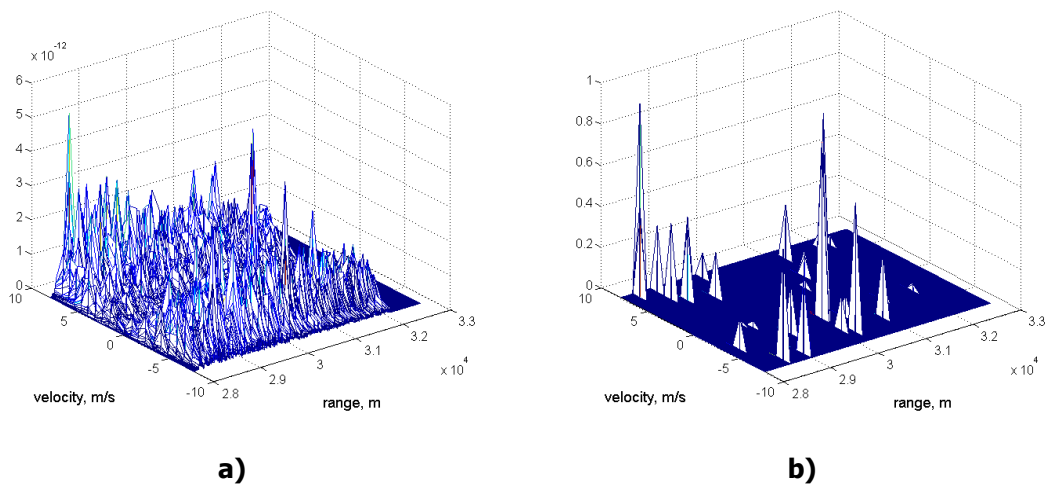
<b><u>Radar Parameters:</u></b>		<b><u>Target Parameters:</u></b>	
Frequency:	9.5 GHz	Vel. (range):	3 m/s
Waveform:	LFM	Vel. (c-range):	0 m/s
Peak Power:	5000 W	RCS:	6 m <sup>2</sup>
PRF:	1000 Hz	Init range:	30100 m
Pulses:	21	Init c-range:	0 m
Noise Figure:	3.5 dB	<b><u>Clutter Parameters:</u></b>	
Pulse width:	0.15 $\mu$ s	# of scatterers:	15000
Velocity:	77 m/s	Reflection coefficient:	-20 dB/ m <sup>2</sup>
7. Antenna pat:	Sinc	Correlation factor:	1
7. Antenna BW:	1.8 degree	Covariance Mat. Deg:	1
8. Antenna pat:	Sinc	Distribution:	Rayleigh
8. Antenna BW:	1.8 degree	Range:	30000 m
<b><u>CFAR Parameters:</u></b>		Cross-range:	0 m
Window length:	40	Swath:	4000 m
Gap length:	2	Width:	5000 m
Pfa:	1e-6		

Figure – 5.11 – b shows the CFAR detector output for the input signal given in Figure – 5.11 – a that is the DPCA processor output where the time slip pulses are 32 and the phase center misalignment distance in the flight direction is 0.1 lambdas. There are 21 Doppler bins and 1264 range bins at the output of the DPCA processor. The number of expected false alarms is around one for a burst having 21 pulses.



**Figure – 5.11:** a) Range-Doppler DPCA Output b) CFAR processor output (Rayleigh distribution)

It can be seen that there is only one false alarm with the target at the output of the CFAR detector. But the distribution of the clutter might be different according to the environment. K-distribution is used to simulate a clutter environment having spiky characteristic.



**Figure – 5.12:** a) Range-Doppler DPCA Output b) CFAR processor output (K-distribution)

If the same simulation is performed by only changing the distribution to K-distribution, from Figure – 5.12, it can be seen that the number of false alarms increases. For both simulations, Cell-Averaging CFAR detector for Rayleigh clutter is used.

## 5.2. Adaptive DPCA

To evaluate the performance of the adaptive DPCA technique, firstly, the clutter suppression capability has to be shown. In the adaptive DPCA technique, the clutter cancellation is performed individually in each Doppler subband. This brings the advantage of improving the cancellation coefficients for each Doppler subband.

Like DPCA processing, the clutter cancellation performance of Adaptive DPCA also depends on the phase center alignment mismatches and the internal clutter motion (ICM).

Figure – 5.13 shows the adaptive DPCA processor output for the simulation parameters given in Table 5 – 2. In this simulation the time slip pulses are 32 and there is no ICM or phase center misalignment.

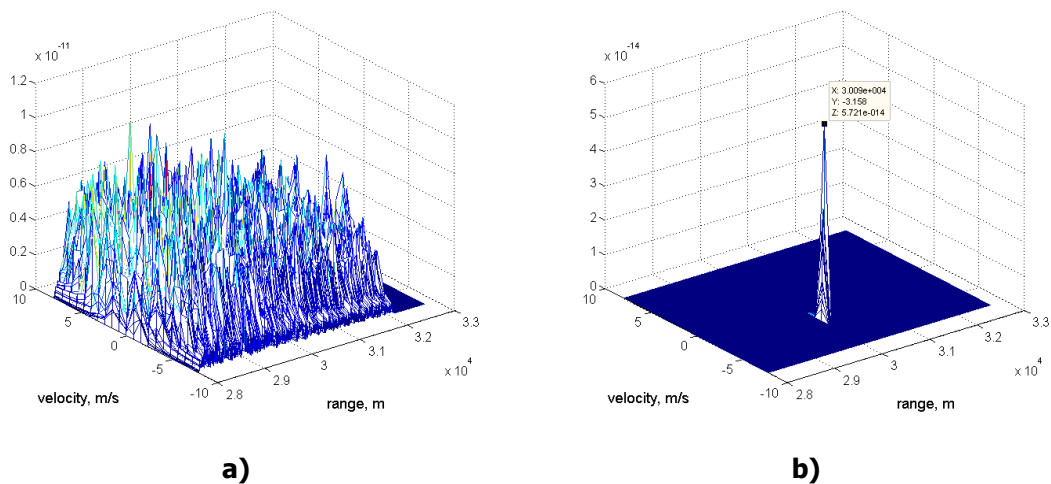


**Figure – 5.13:** a) Range-Doppler Output of First Channel b) Range-Doppler Adaptive DPCA Output for Perfectly Aligned Antenna Case (target exists)

Figure – 5.14 shows the relationship between the clutter attenuation level and the normalized frequency for adaptive DPCA. This figure is given for a scenario in which there is no phase center misalignment or ICM.

Just like DPCA, the clutter cancellation performance degrades at higher Doppler frequencies. If compared with DPCA, adaptive DPCA has a higher clutter attenuation level for each Doppler bin.

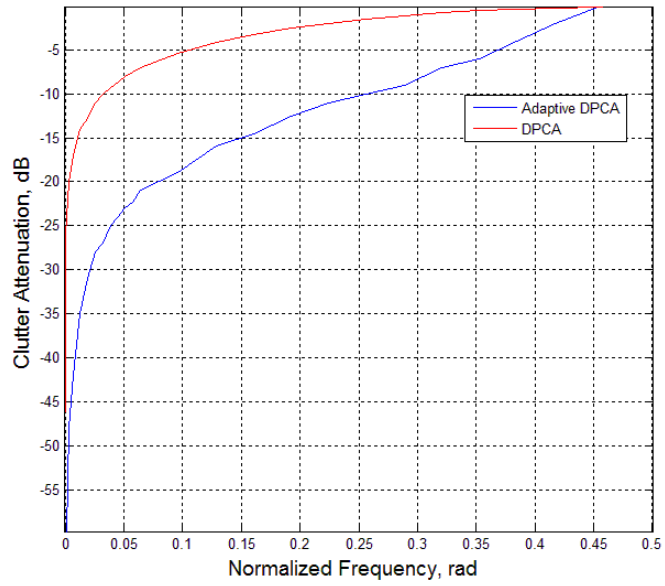


**Figure – 5.14:** Clutter Attenuation vs. Normalized Frequency for Adaptive DPCA

The phase center misalignment degrades the clutter suppression performance of the adaptive DPCA. Figure – 5.15 shows the adaptive DPCA output for the simulation parameters given in Table 5 – 2 where the number of time slip pulses is 32 and phase center misalignment in the flight direction is 0.1 lambdas. If the results given in Figure – 5.4 and Figure – 5.15 are compared, it can be said that adaptive DPCA has a better clutter suppression capability even in the phase center misalignment case. This gives robustness to the adaptive DPCA against the clutter.

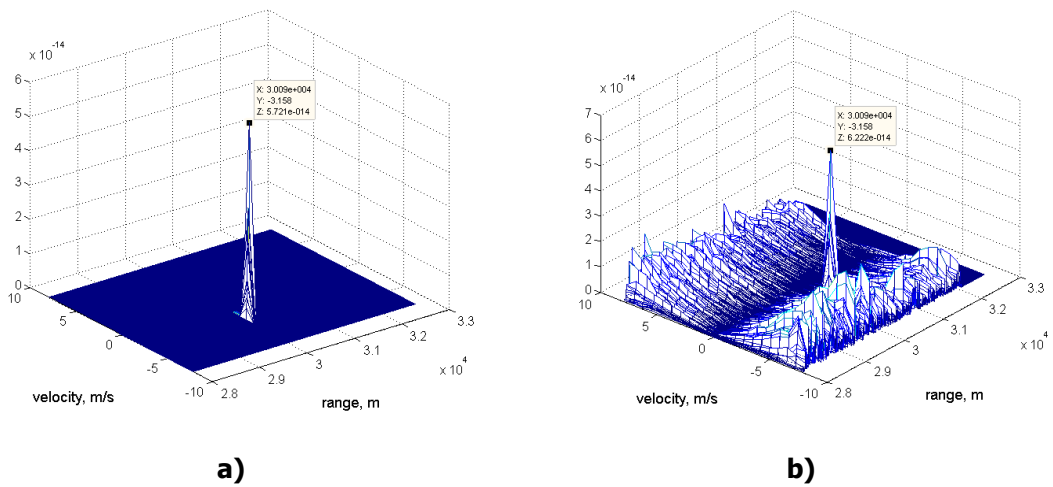


**Figure – 5.15:** Range-Doppler Adaptive DPCA Output for a) Perfectly Aligned Antenna Case  
b) Phase Center Misaligned Case (target exist)

As can be seen from Figure – 5.16, the clutter attenuation (CA) ratio is decreasing with the increasing value of the phase center misalignment. The clutter cancellation performance of adaptive DPCA degrades with increasing phase center misalignment like DPCA.

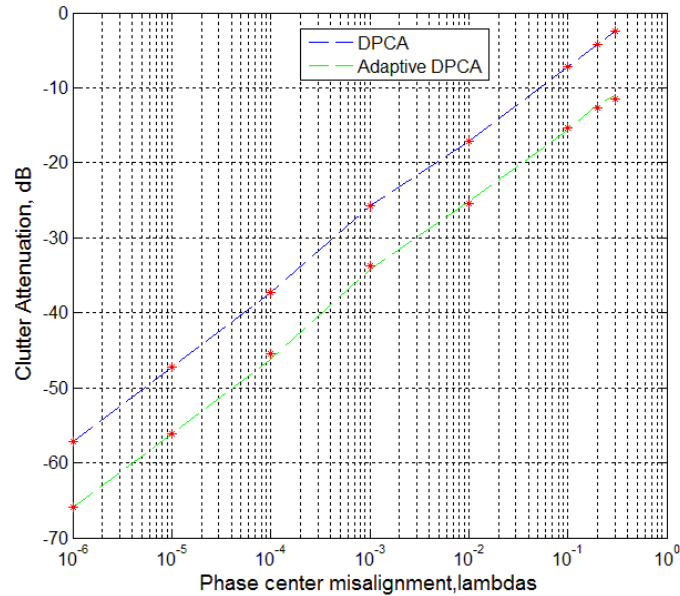


**Figure – 5.16:** Clutter Attenuation vs. Phase Center Misalignment

The ICM is one of the most important factors affecting the clutter cancellation performance of adaptive DPCA as is the case in DPCA. The simulation parameters are given in Table 5 – 3 to see the adaptive DPCA performance for a scenario in which ICM exists.

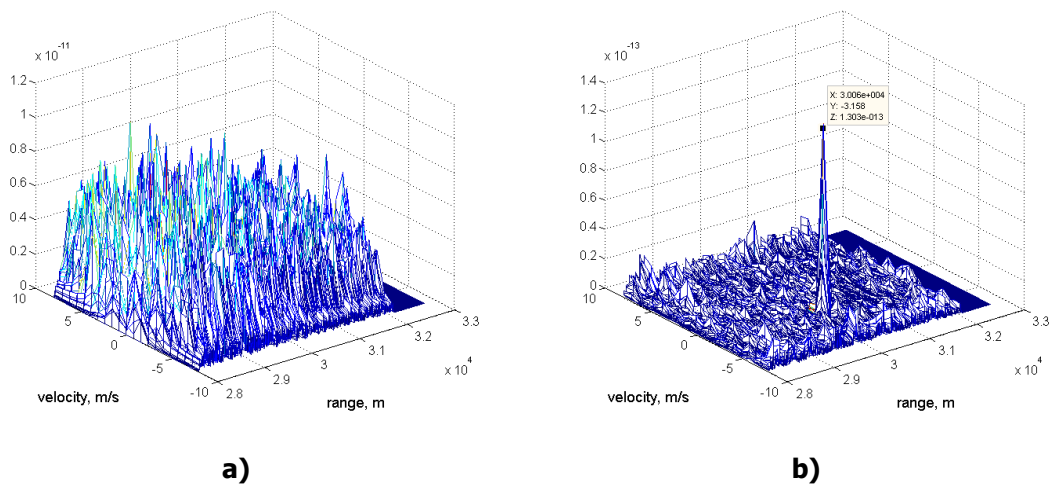


**Figure – 5.17:** a) Range-Doppler Output of First Channel b) Range-Doppler Adaptive DPCA Output for Perfectly Aligned Antenna Case (ICM and target exist)

As is can be seen from Figure – 5.17 – b, the existence of the ICM degrades the performance of adaptive DPCA. But it has a better performance under ICM if compared with DPCA (Figure – 5.17 & Figure – 5.8). This is because of the adaptive weight calculation in each Doppler bin for adaptive DPCA. It uses the neighboring range cells to estimate the clutter covariance matrix. Even its performance superiority against DPCA, under highly decorrelated clutter environments, the clutter suppression performance of the adaptive DPCA degrades. Figure – 5.18 shows the relationship between the clutter correlation factor and the clutter attenuation level for the adaptive DPCA.

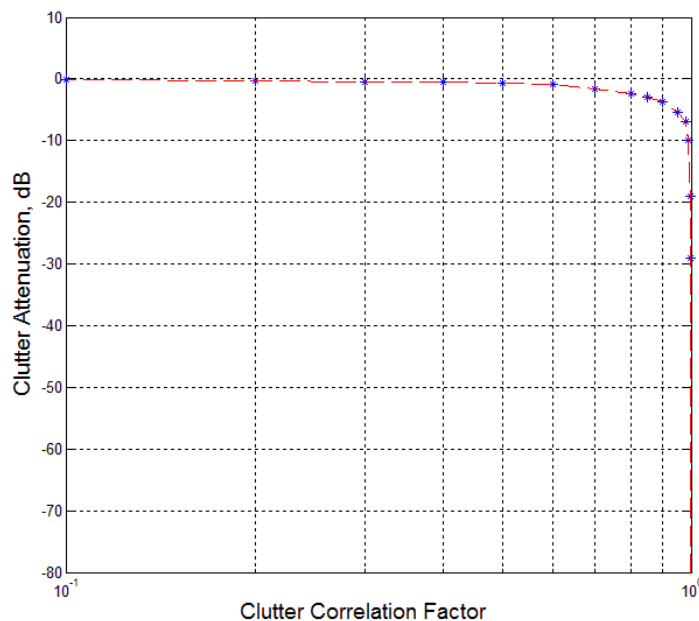
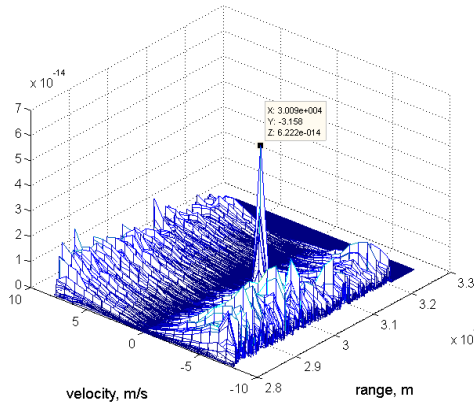


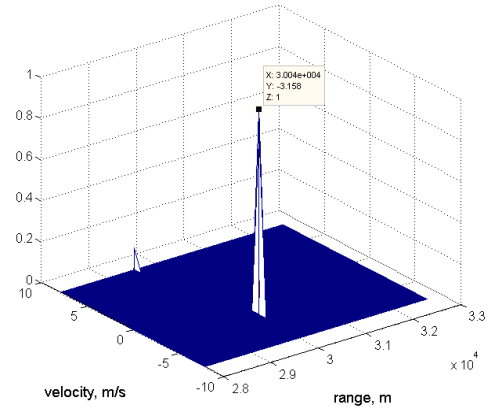
**Figure – 5.18:** Clutter Attenuation vs. Clutter Correlation Factor

Like DPCA, a conventional Cell-Averaging CFAR algorithm is applied to the adaptive DPCA processor output to detect the targets. The simulation parameters are given in Table 5 – 4.

Unsurprisingly, the adaptive DPCA has fewer false alarms than the DPCA (Figure – 5.19).



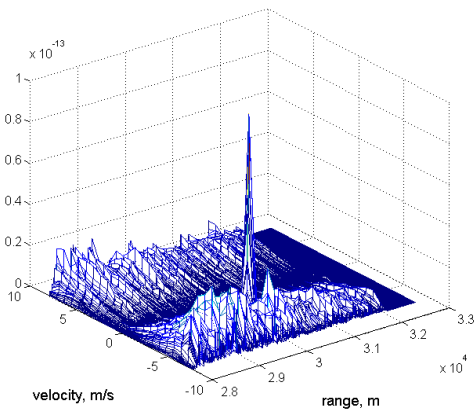
a)



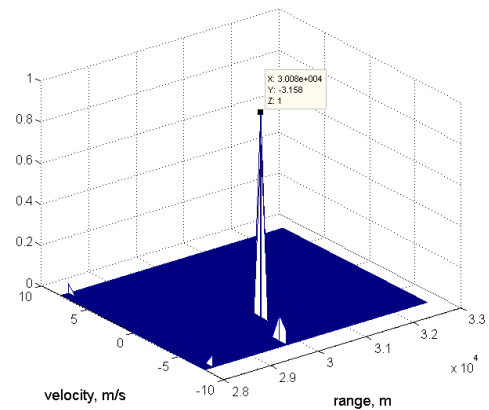
b)

**Figure – 5.19:** a) Range-Doppler DPCA Output b) CFAR processor output (Rayleigh distribution)

But the false alarm performance is more important under spiky clutter environments. If the K-distribution is selected from the simulator interface without changing any parameter, it can be seen that adaptive DPCA has a better performance (Figure – 5.20) under spiky clutter environment than DPCA (Figure – 5.12). For both simulations, Cell-Averaging CFAR detector for Rayleigh clutter is used.



a)



b)

**Figure – 5.20:** a) Range-Doppler DPCA Output b) CFAR processor output (K-distribution)

### 5.3. ATI

As explained in Chapter-3, ATI is not a clutter suppression technique. It uses the advantage of correlation of the moving targets.

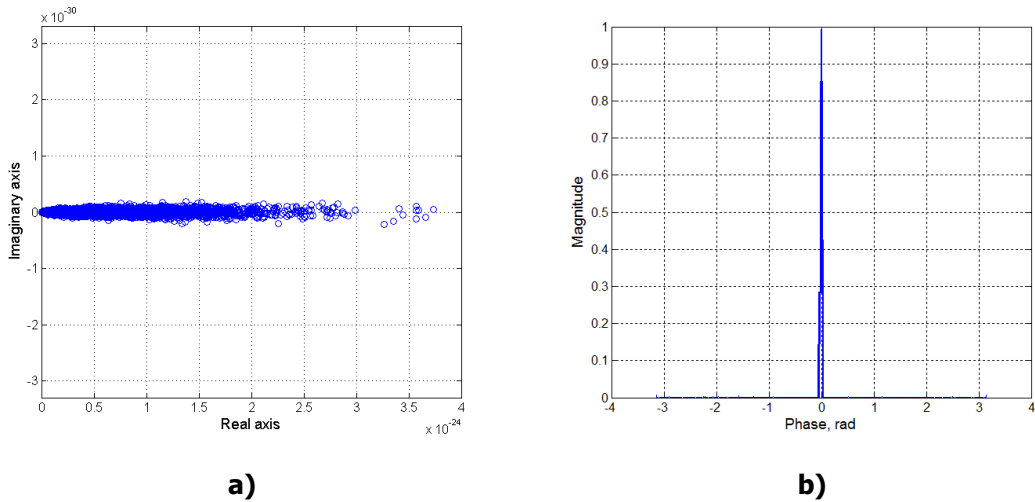
It may be better to explain the ATI output for a case in which only clutter exists. If the phase center alignment is exact, the clutter samples are located around the real axis after the ATI correlation process. When the phase center misalignment is increased, the correlation of the clutter samples between fore and aft antennas will decrease and the clutter samples start to spread with larger imaginary parts as explained in Section 3.3. This is due to the phase difference between clutter samples at the fore and aft antennas.

**Table 5 – 5:** Simulation Parameters for Figure – 5.21

<b><u>Radar Parameters:</u></b>		<b><u>Target Parameters:</u></b>	
Frequency:	9.5 GHz	Vel. (range):	3 m/s
Waveform:	LFM	Vel. (c-range):	0 m/s
Peak Power:	5000 W	RCS:	0 m <sup>2</sup>
PRF:	1000 Hz	Init range:	30100 m
Pulses:	21	Init c-range:	0 m
Noise Figure:	3.5 dB	<b><u>Clutter Parameters:</u></b>	
Pulse width:	0.15 μs	# of scatterers:	15000
Velocity:	77 m/s	Reflection coefficient:	-30 dB/ m <sup>2</sup>
9. Antenna pat:	Sinc	Correlation factor:	1
9. Antenna BW:	1.8 degree	Covariance Mat. Deg:	1
10. Antenna pat:	Sinc	Distribution:	Rayleigh
10. Antenna BW:	1.8 degree	Range:	30000 m
		Cross-range:	0 m
		Swath:	4000 m
		Width:	5000 m

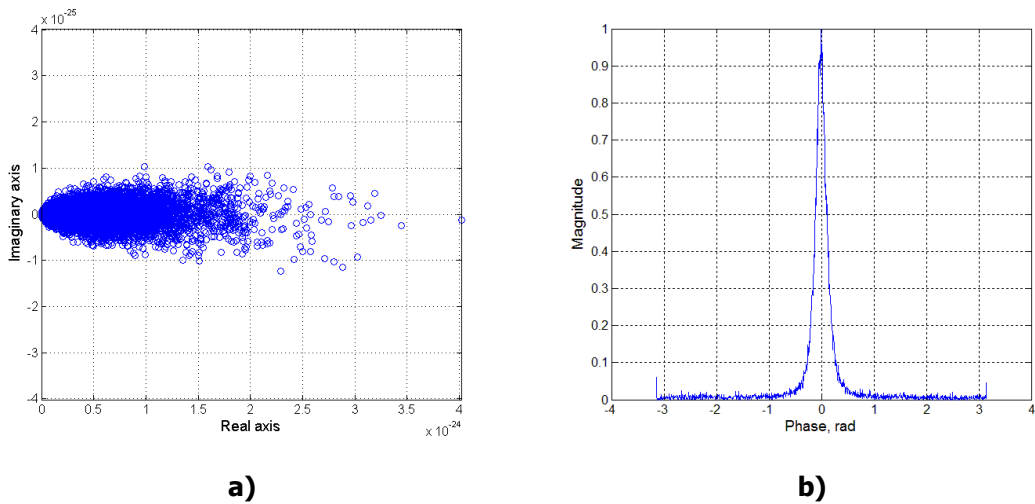
Figure – 5.21 shows the ATI processor output for the simulation parameters given in Table 5 – 5. For this simulation, there is no target and no phase center misalignment. It can be seen that the clutter samples are collected at

the zero phase angle in the phase-magnitude plane as explained in Section 3.3.



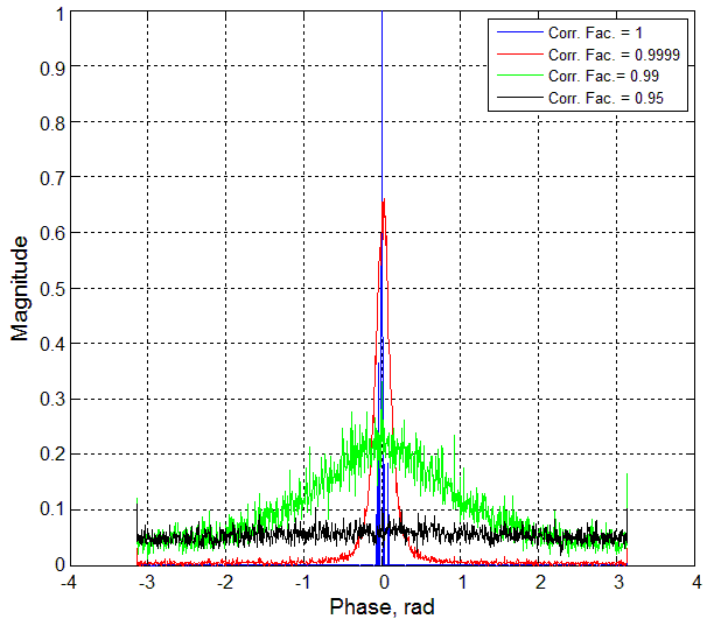
**Figure – 5.21:** a) ATI Output at Complex Plane b) ATI Output at Phase-Magnitude Plane (only highly correlated clutter)

If the clutter correlation decreases, the clutter samples start to spread into the phase axis. Figure – 5.22 shows the simulation results for the same parameters with the previous example but the clutter correlation factor is 0.9999 in this case.



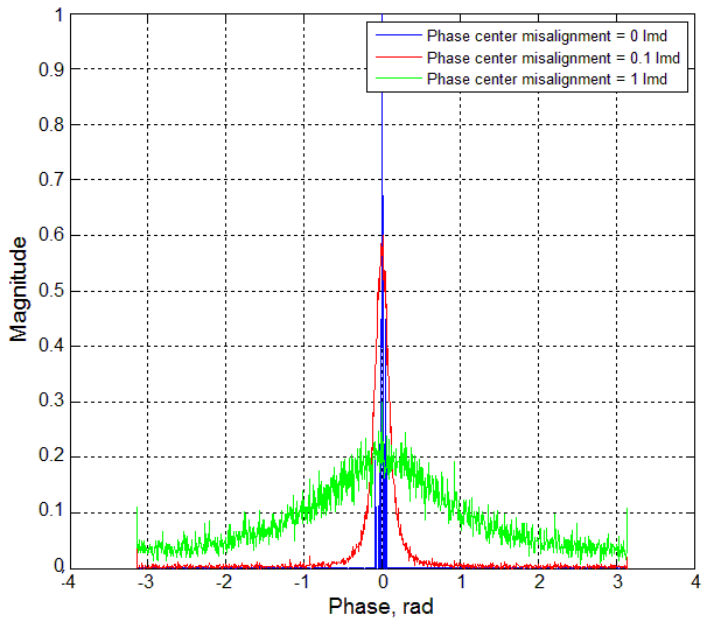
**Figure – 5.22:** a) ATI Output at Complex Plane b) ATI Output at Phase-Magnitude Plane (only clutter, correlation factor = 0.9999)

Figure – 5.23 shows the ATI processor output at Phase-Magnitude Plane for different clutter correlation factors.



**Figure – 5.23:** ATI Output at Phase-Magnitude Plane for Different Correlation Factors

Any phase center misalignment in the flight direction also changes the correlation of the clutter samples between fore and aft channels. Figure – 5.24 shows the ATI processor output at Phase-Magnitude Plane for different phase center misalignment distances.

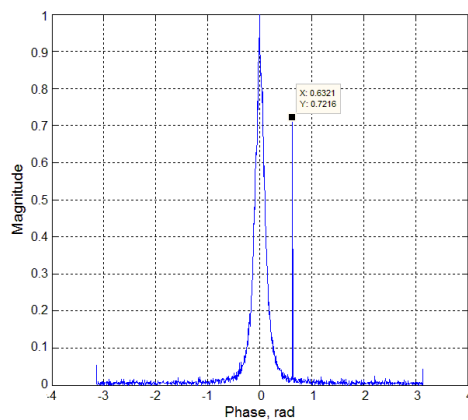


**Figure – 5.24:** ATI Output at Phase-Magnitude Plane for Different Phase Center Misalignments

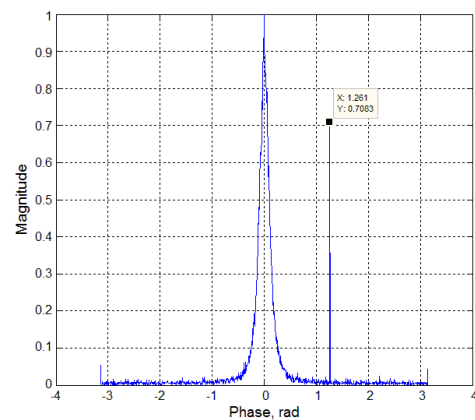
Figure – 5.25 shows the ATI output at phase-magnitude plane for targets having 3 m/s velocity (a) and 6 m/s velocity (b). The simulation parameters are given in Table 5 – 6.

**Table 5 – 6:** Simulation Parameters for Figure – 5.25

<b><u>Radar Parameters:</u></b>		<b><u>Target Parameters:</u></b>	
Frequency:	9.5 GHz	Vel. (range):	3 m/s & 6 m/s
Waveform:	LFM	Vel. (c-range):	0 m/s
Peak Power:	5000 W	RCS:	6 m <sup>2</sup>
PRF:	1000 Hz	Init range:	30100 m
Pulses:	21	Init c-range:	0 m
Noise Figure:	3.5 dB	<b><u>Clutter Parameters:</u></b>	
Pulse width:	0.15 $\mu$ s	# of scatterers:	15000
Velocity:	77 m/s	Reflection coefficient:	-20 dB/ m <sup>2</sup>
11. Antenna pat:	Sinc	Correlation factor:	0.9999
11. Antenna BW:	1.8 degree	Covariance Mat. Deg:	1
12. Antenna pat:	Sinc	Distribution:	Rayleigh
12. Antenna BW:	1.8 degree	Range:	30000 m
		Cross-range:	0 m
		Swath:	4000 m
		Width:	5000 m



**a)**



**b)**

**Figure – 5.25:** ATI Output at Phase-Magnitude Plane a) with a Target having 3m/s velocity b) with a Target having 6m/s velocity (correlation factor = 0.9999)

As can be seen from Figure – 5.25, there is a limit for the minimum detectable velocity performance. The clutter samples may spread onto the phase axis after ATI process due to the ICM and the phase center misalignment. This makes it difficult to detect target signal through the clutter samples. There are some detection techniques used with ATI processing, but, in this thesis, these techniques are not investigated.

Another important factor affecting the ATI performance is the noise. The existence of noise may spread the clutter samples into the phase axis. This makes it difficult to detect slow moving targets and the minimum detectable velocity will increase.

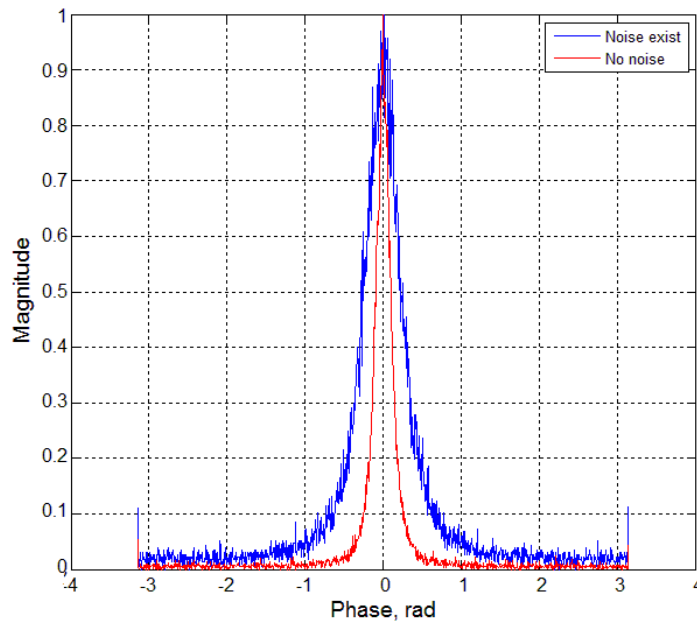


**Figure – 5.26:** ATI Output at Phase-Magnitude Plane for the cases a) Noise exist b) No noise

#### 5.4. $\Sigma - \Delta$ STAP

There are two methods of  $\Sigma - \Delta$  STAP explained in Section 3.4 which are Pre-Doppler and Post-Doppler. Pre-Doppler performs the weight calculations before any Doppler processing and the cancellation is done in time domain.

The scenario parameters are given in Table 5 – 7 to see the performance of Pre-Doppler  $\Sigma - \Delta$  STAP.

**Table 5 – 7:** Simulation Parameters for Figure – 5.27

<b><u>Radar Parameters:</u></b>		<b><u>Target Parameters:</u></b>	
Frequency:	9.5 GHz	Vel. (range):	3 m/s
Waveform:	LFM	Vel. (c-range):	0 m/s
Peak Power:	5000 W	RCS:	3 m <sup>2</sup>
PRF:	1000 Hz	Init range:	30100 m
Pulses:	21	Init c-range:	0 m
Noise Figure:	3.5 dB	<b><u>Clutter Parameters:</u></b>	
Pulse width:	0.15 $\mu$ s	# of scatterers:	15000
Velocity:	77 m/s	Reflection coefficient:	-20 dB/ m <sup>2</sup>
13. Antenna pat:	Taylor	Correlation factor:	1
13. Antenna BW:	9 degree	Covariance Mat. Deg:	1
14. Antenna pat:	Bayliss	Distribution:	Rayleigh
14. Antenna BW:	9 degree	Range:	30000 m
		Cross-range:	0 m
		Swath:	4000 m
		Width:	5000 m

In Figure – 5.27, Range-Doppler outputs of sigma and delta channels are shown. As can be seen from the figures, at low frequencies of Range-Doppler output of delta channel, the signal strength is low. This is because of the monopulse characteristic of the antenna used for the delta channel.

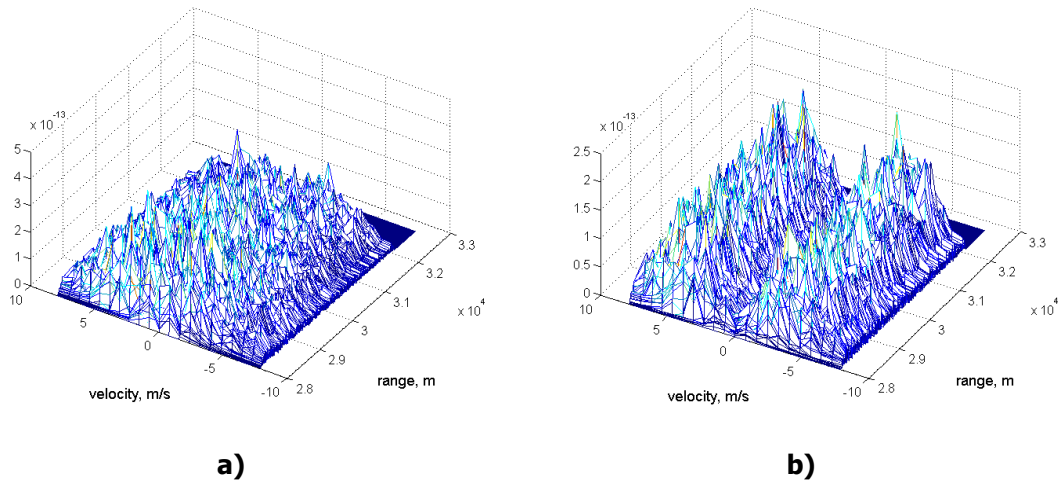


**Figure – 5.27:** a) Range-Doppler Output of Sigma Channel, b) Range-Doppler Output of Delta Channel (no ICM)

In the  $\Sigma - \Delta$  STAP simulations performed in this thesis, usually, Taylor and Bayliss patterns are used. The typical shapes of these patterns are shown in Figure – 5.28.

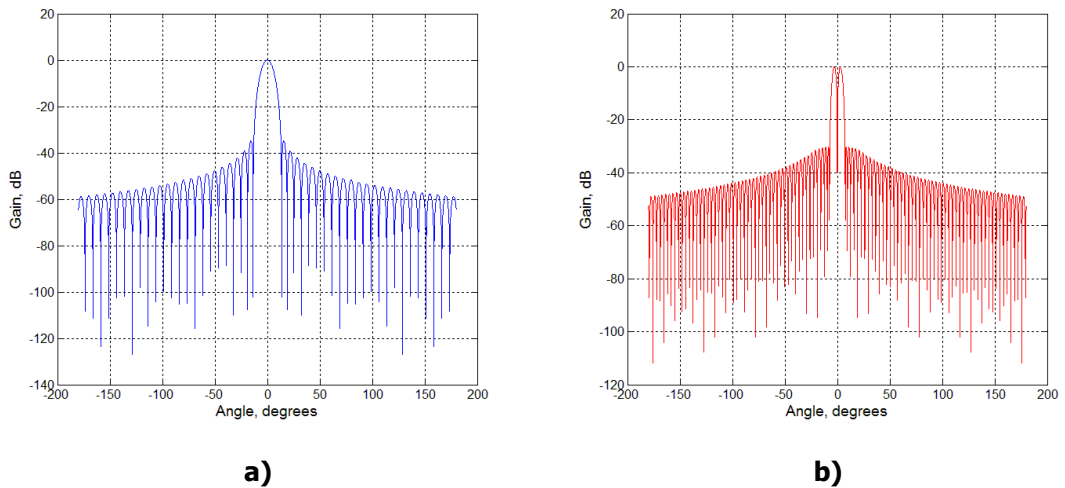


**Figure – 5.28:** a) Taylor Pattern (SSL = -35 dB) b) Bayliss Pattern

Figure – 5.29 shows the Range-Doppler output of Pre-Doppler  $\Sigma - \Delta$  STAP. The target cannot be found with a high SINR value. In  $\Sigma - \Delta$  STAP, the clutter at the sum channels is suppressed by using the clutter information at

the difference channel where there is no target signal because of the notch at the boresight of the antenna pattern.

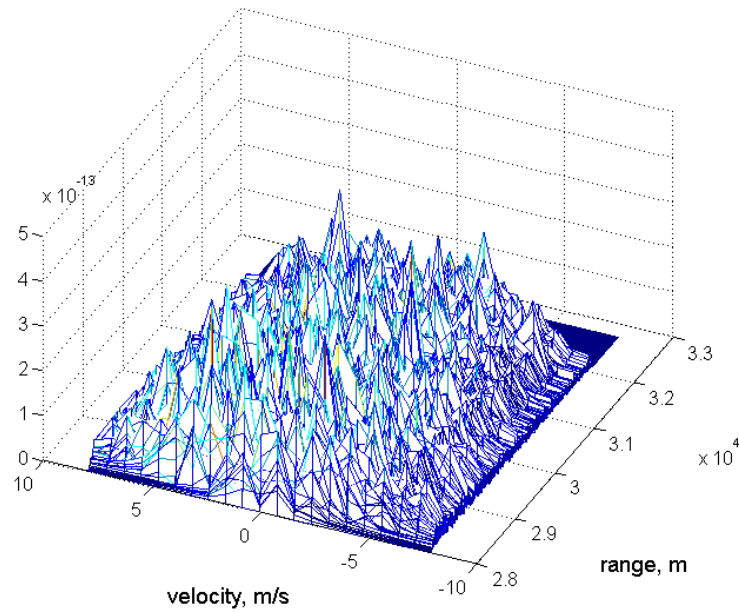


**Figure – 5.29:** Output of Pre-Doppler  $\Sigma - \Delta$  STAP

Post-Doppler  $\Sigma - \Delta$  STAP is another method for clutter suppression in the case of sum and delta channels usage. It performs the adaptive cancellation weight estimation after Doppler processing.

The scenario parameters are given in Table 5 – 8 to see the performance of Post-Doppler  $\Sigma - \Delta$  STAP.

**Table 5 – 8:** Simulation Parameters for Figure – 5.30

<b><u>Radar Parameters:</u></b>		<b><u>Target Parameters:</u></b>	
Frequency:	9.5 GHz	Vel. (range):	5 m/s
Waveform:	LFM	Vel. (c-range):	0 m/s
Peak Power:	5000 W	RCS:	20 m <sup>2</sup>
PRF:	1000 Hz	Init range:	30100 m
Pulses:	21	Init c-range:	0 m
Noise Figure:	3.5 dB	<b><u>Clutter Parameters:</u></b>	
Pulse width:	0.15 μs	# of scatterers:	15000
Velocity:	77 m/s	Reflection coefficient:	-20 dB/ m <sup>2</sup>
15. Antenna pat:	Taylor	Correlation factor:	1
15. Antenna BW:	9 degree	Covariance Mat. Deg:	1
16. Antenna pat:	Bayliss	Distribution:	Rayleigh
16. Antenna BW:	9 degree	Range:	30000 m
		Cross-range:	0 m
		Swath:	4000 m
		Width:	5000 m

In Figure – 5.30, the Range-Doppler outputs of sigma and delta channels are shown. These Range-Doppler outputs are the same with the ones shown in Figure – 5.27. But the Post-Doppler method will be applied to the signals measured from sum and delta channels.

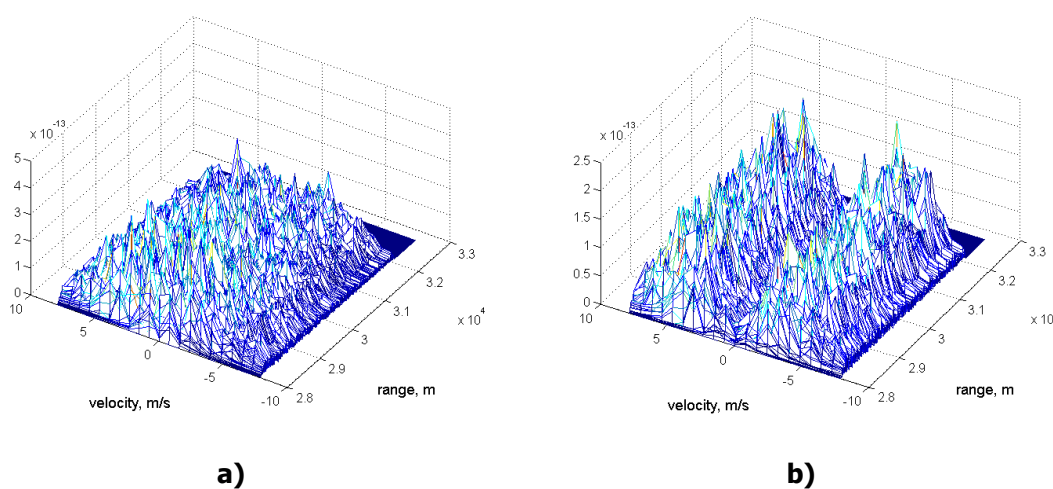


**Figure – 5.30:** a) Range-Doppler Output of Sigma Channel, b) Range-Doppler Output of Delta Channel (no ICM)

Figure – 5.31 shows the Range-Doppler output of Post-Doppler  $\Sigma - \Delta$  STAP method applied to the signals shown in Figure – 5.30. It can be seen that the target signal has a high SINR level at the output of the Post-Doppler method.

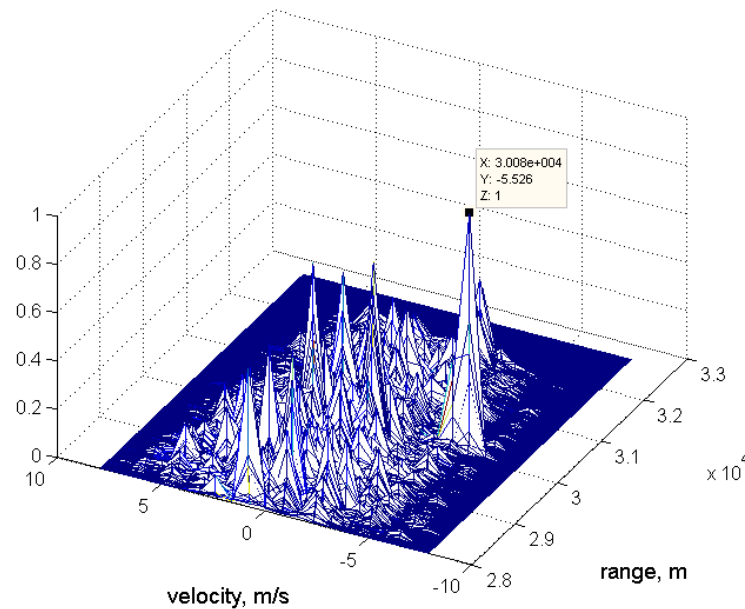


**Figure – 5.31:** Output of Post-Doppler  $\Sigma - \Delta$  STAP

But there are some clutter signals which cannot be eliminated and located at low Doppler frequencies. This is because of the deficiency in the estimation of the clutter covariance matrix due to the number of neighboring range cells used in the simulation and the width of the notch at the difference pattern. Increasing the length of the observation time may be a method to estimate the clutter covariance matrix successfully at these low Doppler frequencies.

For the  $\Sigma - \Delta$  STAP, there is no phase center misalignment problem. Because the phase center of the sum and difference patterns are same. This gives a great advantage to the  $\Sigma - \Delta$  STAP.

The main purpose of the  $\Sigma - \Delta$  STAP methods is to suppress the clutter signal by using the clutter information at the delta channel where the target signal is not present because of the notch at the boresight of the difference

pattern. As the width of this notch is small, the miss-observed clutter signal level will be low.

Post-Doppler  $\Sigma - \Delta$  STAP method works successfully for the targets having high RCS values if the antenna has a narrow beamwidth. The simulation parameters are given in Table 5 – 9.

**Table 5 – 9:** Simulation Parameters for Figure – 5.33

<b><u>Radar Parameters:</u></b>		<b><u>Target Parameters:</u></b>	
Frequency:	9.5 GHz	Vel. (range):	5 m/s
Waveform:	LFM	Vel. (c-range):	0 m/s
Peak Power:	5000 W	RCS:	20 m <sup>2</sup>
PRF:	1000 Hz	Init range:	30100 m
Pulses:	21	Init c-range:	0 m
Noise Figure:	3.5 dB	<b><u>Clutter Parameters:</u></b>	
Pulse width:	0.15 $\mu$ s	# of scatterers:	15000
Velocity:	77 m/s	Reflection coefficient:	-20 dB/ m <sup>2</sup>
17. Antenna pat:	Taylor	Correlation factor:	1
17. Antenna BW:	4.5 degree	Covariance Mat. Deg:	1
18. Antenna pat:	Bayliss	Distribution:	Rayleigh
18. Antenna BW:	4.5 degree	Range:	30000 m
		Cross-range:	0 m
		Swath:	4000 m
		Width:	5000 m

As can be seen from Figure – 5.32, by using an antenna having narrow beamwidth, Post-Doppler  $\Sigma - \Delta$  STAP has a great performance.

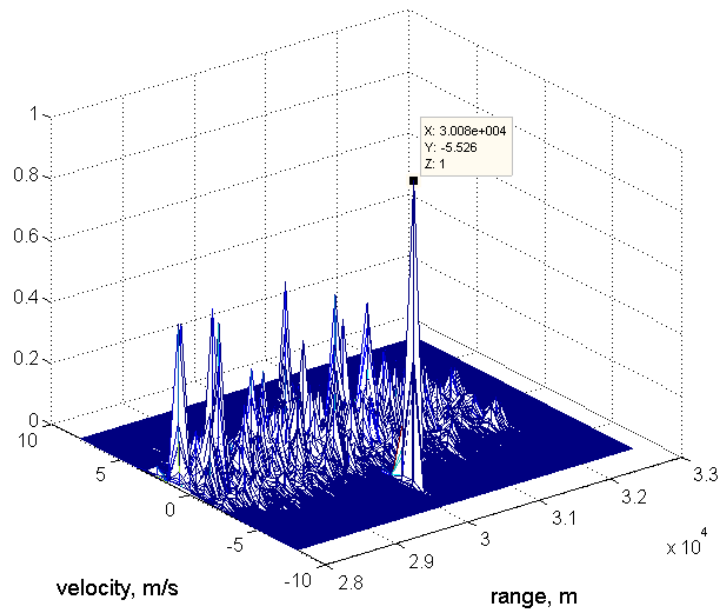


**Figure – 5.32:** Output of Post-Doppler  $\Sigma - \Delta$  STAP (narrow beam antenna)

The most distinctive disadvantage of  $\Sigma - \Delta$  STAP observed in the simulations is its dependence on the RCS. For targets having low RCS values, its performance starts to degrade rapidly. In Figure – 5.33, the Range-Doppler output of the  $\Sigma - \Delta$  STAP processor for a target having 3 dB less RCS than the one used in Figure – 5.32 is shown.

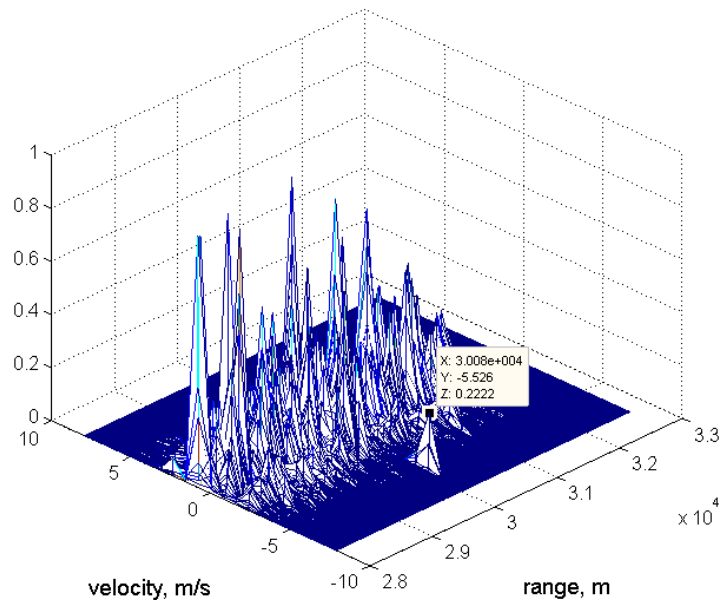


**Figure – 5.33:** Output of Post-Doppler  $\Sigma - \Delta$  STAP (small RCS target)

As can be seen from Figure – 5.33, the decrease in the output SINR is higher than the depletion in the RCS. This is an unexpected result and seems as a performance weakness in  $\Sigma - \Delta$  STAP.

The most important advantage of Post-Doppler  $\Sigma - \Delta$  STAP is its performance superiority against the other GMTI methods in operation performed in a highly decorrelated clutter environment. With the advantage of having constant phase center for sum and difference patterns, the adaptive weight calculation performed in each Doppler bin successfully without being affected from the ICM.  $\Sigma - \Delta$  STAP uses the advantage of space and time divergence in weight estimation and this gives it performance superiority against the other methods.

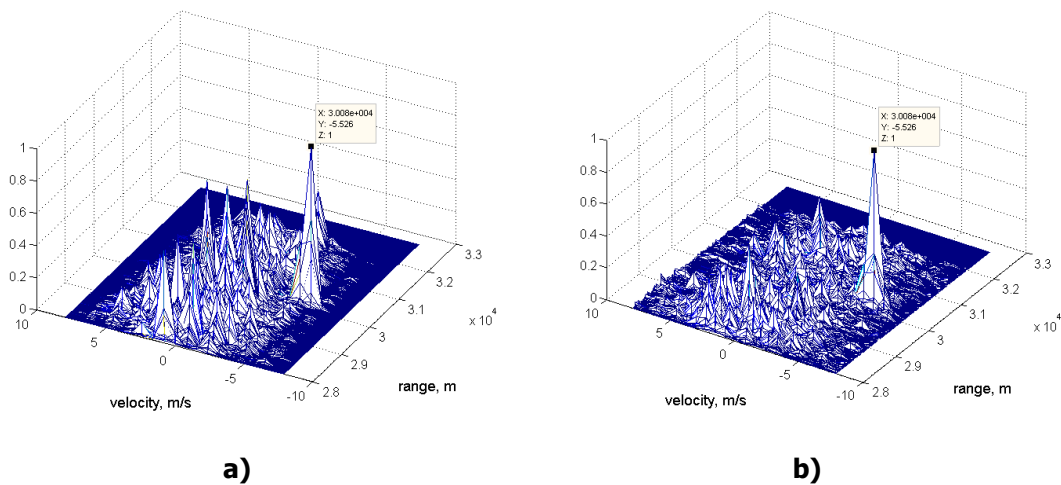


**Figure – 5.34:** Range-Doppler Output of Post-Doppler  $\Sigma - \Delta$  STAP a) Correlation Factor = 1, b) Correlation Factor = 0.6

For highly decorrelated clutter environments, where the ICM is high, clutter spreads onto the Doppler axis. From Figure – 5.34, it can be seen that Post-Doppler  $\Sigma - \Delta$  STAP is not affected so much from the ICM. This brings a great advantage to  $\Sigma - \Delta$  STAP as compared with other GMTI techniques.

## 5.5. Comparison of GMTI Techniques

In this section, a performance comparison of the techniques under different environmental conditions is given.

A short comparison of the basic GMTI techniques is given in Table 5 – 12 and each item is explained below.

The most prominent and distinctive property of the techniques is the phase center alignment problem. For the techniques used with two antennas having different phase centers like DPCA, Adaptive DPCA and ATI, phase center alignment problem is one of the most critical issue. Any phase center misalignment causes rapid performance degradation. Adaptive DPCA has a better performance in comparison to DPCA and ATI. Because it uses the advantage of adaptive cancelation in each Doppler subband. ATI and DPCA are very sensitive to the misalignments. There is no phase center alignment problem for  $\Sigma - \Delta$  STAP, because it has two channels having same phase center but different beam shapes. Briefly,  $\Delta$  channel gives the information about the interferences and the unwanted signals are eliminated from the  $\Sigma$  channel by using this information.

In Table 5 – 10, SCR degradation levels for the phase center misalignment (PCM) distances are given. These values are calculated by using a Monte Carlo simulation derived from the simulator and run 25 times. Because of the sample-based characteristic of the simulator, the number of the runs to get these results are low.

**Table 5 – 10:** SCR Degradation Levels vs. PCM Distances for DPCA & Adaptive DPCA

	<b>DPCA</b>	<b>Adaptive DPCA</b>
<b>SCR degradation for PCM = 0.001 lambdas</b>	18 dB	3 dB
<b>SCR degradation for PCM = 0.1 lambdas</b>	33 dB	13 dB

The second distinctive parameter is the SINR (Signal to Interference Plus Noise Ratio) improvement. SINR improvement is investigated as the clutter attenuation. SINR improvement is almost same for adaptive DPCA and  $\Sigma - \Delta$  STAP. Because of their adaptive structures, these techniques have a better performance compared to DPCA. Any performance comparison can not be given for ATI about this property, because ATI is not a clutter suppression technique. SCR degradation levels vs. target velocities are given in Table 5 – 11. These values are given for similar simulation parameters. But the main purpose of this table is to show the degradation in the SCR with changes in the target velocity.

**Table 5 – 11:** SCR Levels vs. Target Velocities

	<b>DPCA</b>	<b>Adaptive DPCA</b>	<b><math>\Sigma - \Delta</math> STAP</b>
<b>SCR (Target Velocity = 6 m/s)</b>	17 dB	39 dB	41 dB
<b>SCR (Target Velocity = 3 m/s)</b>	15 dB	35 dB	29 dB
<b>SCR (Target Velocity = 1 m/s)</b>	5 dB	30 dB	17 dB

- For DPCA and Adaptive DPCA, PCM distance are 0.1 lambdas

According to the MDV (Minimum Detectable Velocity) performances, Adaptive DPCA has good simulation results. ATI has also good results for the targets having high RCS values. As can be seen from Table 5 – 11, the least SCR degradation occurs in Adaptive DPCA.  $\Sigma - \Delta$  STAP has a deficiency in the estimation of the clutter covariance matrix due to the number of neighboring range cells used in the simulation and the width of the notch at the difference pattern. If the adaptive weights are not calculated successfully, the SCR degradation for low Doppler frequencies will be high. But this problem can be solved by using longer observation times.

For the detection of targets having low RCS values, adaptive DPCA has the best performance. Because of its fairly robust structure to the phase center

misalignments and adaptive cancellation characteristic, it gives quite well results.  $\Sigma - \Delta$  STAP also has an adaptive structure but it also has good performance results for the scenarios where long observation times are used.

In the case of working in a heterogeneous clutter environment, adaptive DPCA and  $\Sigma - \Delta$  STAP have better performance results in comparison with DPCA and ATI. As can be seen from Figure – 5.8, Figure – 5.10, Figure – 5.17, Figure – 5.18, Figure – 5.23 and Figure – 5.34,  $\Sigma - \Delta$  STAP has the best performance in highly decorrelated clutter environment where the ICM is high.

DPCA has the minimum processing load. ATI is also a simple algorithm but the thresholding algorithms suggested for this method like [19] are more complex than the other techniques. Adaptive DPCA and  $\Sigma - \Delta$  STAP have quite similar processing steps. The processing loads for these techniques are higher than the other techniques because of their adaptive structures.

If the hardware simplicities to implement these techniques are compared, Adaptive DPCA and  $\Sigma - \Delta$  STAP have more complex structures because of their processing loads.

**Table 5 – 12:** Comparison of GMTI Techniques

	<b>DPCA</b>	<b>Adaptive DPCA</b>	<b>ATI</b>	<b>SD-STAP</b>
<b>Robustness to the Phase Mismatches</b>	<i>poor</i>	<i>good</i>	<i>poor</i>	<i>excellent</i>
<b>Clutter Attenuation</b>	<i>poor</i>	<i>good</i>	-	<i>good</i>
<b>Minimum Detectable Velocity</b>	<i>poor</i>	<i>good</i>	<i>good</i>	<i>good</i>
<b>Low RCS Target Detection</b>	<i>good</i>	<i>good</i>	<i>poor</i>	<i>poor</i>
<b>Performance in Heterogeneous Clutter</b>	<i>poor</i>	<i>good</i>	<i>poor</i>	<i>excellent</i>
<b>Processing Load</b>	<i>low</i>	<i>high</i>	<i>medium</i>	<i>high</i>

If Table 5 – 12 is investigated, the Adaptive DPCA and  $\Sigma - \Delta$  STAP can be defined as the techniques having some superiority against other GMTI techniques. DPCA and ATI are the simplest techniques frequently used in real systems even today. In spite of their high processing loads, Adaptive DPCA and  $\Sigma - \Delta$  STAP have better simulation results in challenging environmental conditions. Because of their adaptive structures, the target detection and clutter suppression performances are better.

## **CHAPTER 6**

### **CONCLUSIONS**

#### **6.1. Thesis Summary**

The main objective of this thesis was developing a GMTI simulator to compare some GMTI techniques under various environmental conditions.

A basic theoretical review of GMTI geometry, Doppler and clutter structures for airborne radars was required at the beginning to understand the GMTI concept. Then, the characteristics, the processing steps, advantages and disadvantages of the GMTI techniques which are investigated throughout this thesis were studied.

In order to compare the techniques, an in-depth study on the GMTI simulator development was required. The raw GMTI data generation including the target and clutter signals and the techniques used to accelerate the simulator data generation speed are important parts of this thesis.

After developing the GMTI simulator, the techniques were implemented and run on the raw data generated by the simulator. The techniques are compared according to their performances under scenarios where phase center misalignment and internal clutter motion exist.

According to the simulation results, it is seen that the phase center alignment problem is one of the most critical issue for the techniques used with two antennas having different phase centers like DPCA, Adaptive DPCA and ATI. There is no phase center alignment problem for  $\Sigma - \Delta$  STAP, because it has two channels having same phase center but different beam shapes.

For highly decorrelated clutter environment ,i.e. where ICM exists,  $\Sigma - \Delta$  STAP has the best performance results because it takes measurements from different channels having same phase center. The simulation results show that the target detection performance degrades for the techniques taking measurements at nearly same position but at different time instants.

The output SINR performances of the techniques are compared by using a Monte Carlo simulation. Because of the sample based characteristic of the simulator, the number of runs is not high. But the simulation results show that SINR improvement is almost same for adaptive DPCA and  $\Sigma - \Delta$  STAP. Because of their adaptive structures, these techniques have a better performance compared to DPCA.

According to the MDV (Minimum Detectable Velocity) performances, Adaptive DPCA has good simulation results. ATI has also good results for the targets having high RCS values.  $\Sigma - \Delta$  STAP has a deficiency in the estimation of the clutter covariance matrix due to the number of neighboring range cells used in the simulation and the width of the notch at the difference pattern. If the adaptive weights are not calculated successfully, the SCR degradation for low Doppler frequencies will be high. But this problem can be solved by using longer observation times.

DPCA has the minimum processing load. ATI is also a simple algorithm but the thresholding algorithms suggested for this method are more complex than the other techniques. Adaptive DPCA and  $\Sigma - \Delta$  STAP have quite similar

processing steps. The processing loads for these techniques are higher than the other techniques because of their adaptive structures.

As a result, the Adaptive DPCA and  $\Sigma - \Delta$  STAP can be defined as the techniques having some superiority against other GMTI techniques because of their adaptive structures. But they have high processing loads. DPCA and ATI are the simplest techniques frequently used in real systems even today.

## **6.2. Future Work**

There are some research activities that could not be investigated during this process. Some of the topics that would require further investigation are:

- a. All simulations in this thesis were performed for a scenario where the antenna squint angle is zero. The comparison of the techniques investigated throughout this thesis for the scenarios where the squint angle is not zero is a future work.
- b. The detection of the target having variable velocity components
- c. A study on the techniques used to estimate the direction of the moving target
- d. A research on the effects of moving targets on SAR images

## REFERENCES

- [1] Richards, Mark A., Ph.D., "Fundamentals of Radar Signal Processing", *McGraw-Hill 2005*
- [2] Rangaswamy, M., Weiner, D. and Öztürk, A., "Computer Generation of Correlated Non-Gaussian Radar Clutter", *IEEE Transactions On Aerospace and Electronic Systems Vol. 31, No:1 January 1995*
- [3] Jao, J. K., "Theory of Synthetic Aperture Radar Imaging of a Moving Target", *IEEE Transactions on Geoscience and Remote Sensing Vol. 39, No: 9 September 2001*
- [4] Fienup, J.R., "Detecting Moving Targets in SAR Imagery by Focusing", *IEEE Transactions On Aerospace and Electronic Systems Vol. 37, No:3 July 2001*
- [5] Rüegg, M., Meier, E. and Nüesch, D., "Capabilities of Dual-Frequency Millimeter Wave SAR with Monopulse Processing for Ground Moving Target Indication", *IEEE Transactions on Geoscience and Remote Sensing Vol. 45 No:3 March 2007*
- [6] Dunn, R. J., Bingham, P. T., Fowler, C. A., "Ground Moving Target Indicator Radar", *Northrop Grumman Analysis Center Papers, February 2004*
- [7] Chapin, E. and Chen, C. W., "GMTI Along-Track Interferometry Experiment", *IEEE A&E Systems Magazine, March 2006*
- [8] Bergin, J. S. and Techau, P. M., "Multiresolution Signal Processing for Ground Moving Target Detection Using Airborne Radar", *EURASIP Journal on Applied Signal Processing Volume 2006, Article ID 47534, Pages 1-16*
- [9] Guerci, J.R. and Steinhardt, A. O., "Multiresolution GMTI Radar", *IEEE 2003*
- [10] Beaulne, P. D., Gierull, C. H., Livinstone, C. E., Sikenata, I. C. and Chiu, S., "Preliminary Design of a SAR-GMTI Processing System for RADARSAT-2 MODEX Data", *IEEE 2003*
- [11] Gierull, C.H., "Moving Target Detection with Along-Track SAR Interferometry – a Theoretical Analysis", *Tech. Rep. TR 2002-084, Defence R&D Canada-Ottawa, Canada, Aug. 2002*

- [12] Gierull, C.H. and Sikenata, I. C., "Raw Data Based Two-Aperture SAR Ground Moving Target Indication", *IEEE 2003*
- [13] Brown, R.D., Schneible, R.A., Wicks, M.C., Wang, H. and Zhang, Y., "STAP for Clutter Suppression with Sum and Difference Beams", *IEEE Transactions On Aerospace and Electronic Systems Vol.36, No:2 April 2000*
- [14] Bürger, W., "Space-Time Adaptive Processing: Algorithms", *Educational Notes RTO-EN-SET-086, Paper 7. Neuilly-sur-Seine, France: RTO.*
- [15] Linnehan, R., Perlovsky, R., Mutz, C. and Shindler, J., "Detection of Slow Moving Targets in SAR Images", *Proc. Of SPIE Vol. 5410*
- [16] Minardi, M.J. and Zelnio, E.G., "Comparison of SAR Based GMTI and Standart GMTI in a Dense Target Environment", *Proc. Of SPIE Vol. 6237*
- [17] Chiu, S. and Livinstone, C., "A Comparison of Displaced Phase Center Antenna and Along-Track Interferometry Techniques for RADARSAT-2 Ground Moving Target Indication", *Canadian Journal of Remote Sensing Vol.31, No:1, pp.37-51, 2005*
- [18] Livinstone, C. and Sikenata, I. C., "Focusing Moving Targets", *DRDC Ottawa TM 2004-160*
- [19] Chiu, S., "A Constant False Alarm Rate (CFAR) Detector for RADARSAT-2 Along-Track Interferometry", *Canadian Journal of Remote Sensing Vol.31, No:1, pp.73-84, 2005*
- [20] Wicks, M.C., "Knowledge-Based Control For Space Time Adaptive Processing", *RTO-EN-SET-063*
- [21] Blum, R.S., Melvin, W.L. and Wicks, M.C., "An Analysis of Adaptive DPCA", *IEEE Transactions On Aerospace and Electronic System, 1996*
- [22] Jung, B.W., Chun, J. and Adve, R.S. , "Discrete Suppression with  $\Sigma\Delta$ -STAP", *Waveform Diversity and Design, 2007*
- [23] Zhang, Y., Hajjari, A., Kim, K. and Himed, B., "A Dual-Threshold ATI-SAR Approach for Detecting Slow Moving Targets", *IEEE 2005*
- [24] Tanik, Y., "Post-Doppler Başarımı", *ASELSAN SAR Projesi Kasım 2008 raporu*
- [25] Chiu, S., "A constant false alarm rate (CFAR) detector for RADARSAT-2 along-track interferometry", *Can. J. Remote Sensing, Vol. 31, No. 1, pp. 73-84, 2005*

- [26] Goldstein, G.B., "False alarm regulation in log-normal and weibul clutter", *IEEE Transections On Aerospace and Electronic System Vol. AES-9 No:1*
- [27] [http://www.ieeeboston.org/edu/images/airborn\\_radar/ground\\_clutter.jpg](http://www.ieeeboston.org/edu/images/airborn_radar/ground_clutter.jpg)